Influence of Carbon Additives on the Electrochemical Performance of Modern Lead-Acid Batteries

Dissertation zur Erlangung des naturwissenschaftlichen Doktorgrades der Julius-Maximilians-Universität Würzburg

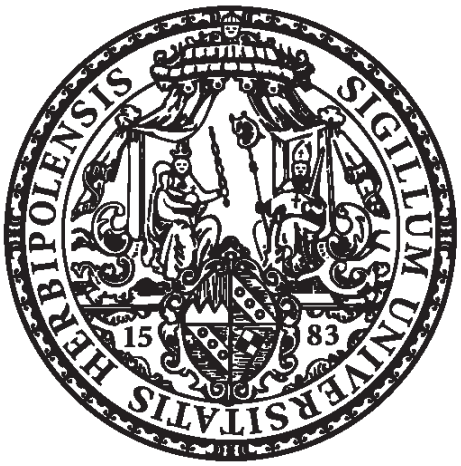

vorgelegt von

Begüm Bozkaya

aus Eskişehir

Fraunhofer-Institut für Silicatforschung ISC

Würzburg, 2022

Fraunhofer ISC

Eingereicht bei der Fakultät für Chemie und Pharmazie am

19.12.2022

Gutachter der schriftlichen Arbeit

1. Gutachter: Prof. Dr. Gerhard Sextl

2. Gutachter: Prof. Dr. Grażyna Gryglewicz

Prüfer des öffentlichen Promotionskolloquiums

1. Prüfer: Prof. Dr. Gerhard Sextl

2. Prüfer: Prof. Dr. Grażyna Gryglewicz

3. Prüfer: Prof. Dr. Lutz Nuhn

Datum des öffentlichen Promotionskolloquiums

10.05.2023

Doktorurkunde ausgehändigt am

This dissertation was conducted from October 2015 to September 2021 at Fraunhofer Institute for Silicate Research ISC in Würzburg under the supervision of Prof. Dr. Gerhard Sextl, Chair of Chemical Technology of Material Synthesis at Julius-Maximilians University of Würzburg. The direct supervision was provided by Dr. Jochen Settelein, Expert Group Manager Analytics at Fraunhofer ISC.

As a part of this dissertation, the master´s thesis of Lukas Gerstner (2020) was supervised. The master´s thesis was also written at Julius-Maximilians University of Würzburg under the supervision of Prof. Dr. Gerhard Sextl. Part of the results obtained from this master´s thesis was included in Chapter 4. The data analysis and scientific interpretation of the results were performed in a regular discussion with the master´s student. Further use of the results in this dissertation is approved by the student.

Scientific Publications

Publications in peer-reviewed scientific journals

B. Bozkaya, S. Bauknecht, J. Settelein, J. Kowal, E. Karden, G. A. Giffin, Comparison of Dynamic Charge Acceptance Tests on Lead-Acid Cells for Carbon Additive Screening, *Energy Technology*, 2022, 10, 2101051, DOI: 10.1002/ente.202101051.

B. Bozkaya, J. Settelein, M. Komma, G. Gryglewicz, G. Sextl, G. A. Giffin, Influence of Basic Carbon Additives on the Electrochemical Performance of Lead-Carbon Batteries, *Journal of Energy Storage*, 2021, 44, 103400, DOI: 10.1016/j.est.2021.103400.

Oral contributions to international conferences

B. Bozkaya, J. Settelein, G. Gryglewicz, G. Sextl, Chemically-Modified Carbon Additives for Increased Dynamic Charge Acceptance in Lead-Acid Batteries, 17th European Lead Battery Conference and Exhibition (ELBC), September 2020, virtual.

B. Bozkaya, J. Settelein, G. Sextl, Approach to Lower Water Consumption: Chemically Modified Carbon Materials for Lead-Acid Batteries, Advanced Automotive Battery Conference Europe (AABC), January 2018, Mainz, Germany.

B. Bozkaya, J. Settelein, H. Lorrmann, G. Sextl, Effects of Surface Chemistry of Carbon on Hydrogen Evolution Reaction in Lead-Carbon Electrodes, 10th International Conference on Lead-Acid Batteries (LABAT), June 2017, Golden Sands, Bulgaria.

B. Bozkaya, J. Settelein, M. Rumpel, H. Lorrmann, G. Sextl, Analysis of the Hydrogen Evolution Reaction on Pure Carbon Additives and Lead-Carbon Electrodes in Sulfuric Acid Solution, 15th European Lead Battery Conference and Exhibition (ELBC), September 2016, Valletta, Malta.

Poster contributions to international conferences

B. Bozkaya, J. Settelein, H. Lorrmann, G. Sextl, The Role of Carbon Surface Chemistry on the Electrochemical Performance of Negative Electrodes in Advanced Lead-Acid Batteries, 7th International Conference on Carbon for Energy Storage and Environment Protection (CESEP), October 2017, Lyon, France.

B. Bozkaya, J. Settelein, M. Rumpel, H. Lorrmann, G. Sextl, Investigation of Hydrogen Evolution Reaction on Pure Carbon Additives and Lead-Carbon Electrodes, NanoCarbon Annual Conference, February 2017, Würzburg, Germany.

Table of Contents

1 Introduction

1.1 Background and motivation

As the energy demand rises due to advanced technologies and changes in the climate, the electrification of vehicles has attracted further attention. This progressive electrification is being driven by increased safety and comfort as well as by the legislation which targets lowering CO_2 emission. Due to the increased demand for electromobility as well as competitive technologies, lead-acid batteries are facing substantial challenges. At this point, it is inevitable to question whether cheap and recyclable lead-acid batteries will still play a role in the 12 V electrical system, which can be found in hybrid and electric cars. Another question can be extended to whether they stand a chance to be used as a cost-efficient 48 V battery for the next higher level of electrified powertrains [1].

The hybrid electric vehicle (HEV) was introduced in order to decrease petrol consumption by the combination of an electrical engine with an internal combustion engine. Based on the degree of electrification, a classification of HEVs such as micro, mild, full and plug-in can be made [2]. A battery for HEVs requires a high power performance, high energy storage capability, high specific energy, long calendar life and affordable cost. A single battery type cannot fulfill all these requirements since each type has its specific advantages. Therefore, a mixture of different battery types is expected to be on the market. Lead-acid batteries (LAB) are often used in micro-hybrids. For mild-, full- and plug-in HEVs, advanced battery technologies like nickel-metal hydride and lithium-ion batteries are exclusively employed. However, a starting-lighting and ignition (SLI) battery is present in all vehicles, which is considered for cranking the combustion engine or providing safety functions within the 12 V power supply. The SLI battery is typically provided by a lead-acid starter battery [1,3].

One of the most important advantages of LABs is the low material cost compared to other battery technologies. LABs consist of around 85 % recycled material. In Europe, almost 99 % of LABs are collected and recycled in case they reach their end of life. This high recycling efficiency is an important factor for car manufacturers considering a product design. Moreover, LABs contain an aqueous electrolyte which makes them intrinsically safe and thus decreases significantly the possibility of fires and explosions. Of course, a LAB is composed of mostly lead and sulfuric acid which are classified as heavy metal and hazardous liquid, respectively. However, these materials do not possess a serious threat to the users and the environment, while being in a battery container. Besides these advantages, LABs have one major disadvantage. In comparison to various batteries, a LAB has a low specific energy, which is between 30 and 40 Wh kg^{-1} due to the high atomic weight of Pb [1,2]. Bringing all this together, LABs

need to undergo further development in order to still be considered as a candidate for future developments such as micro-hybrid vehicles.

Batteries in micro-hybrid vehicles require superior performance in comparison to conventional vehicles. The features like stop/start and regenerative braking are included in micro-hybrids [4]. In such applications, the battery is mainly operated at partial state-of-charge (PSoC). Besides a long service life, a fast recharge is essential to provide a highly efficient recuperation function in order to reduce fuel consumption [1]. The recharge-ability of a micro-hybrid battery during recuperation events is called dynamic charge acceptance (DCA). The DCA is defined as the average charge current over the initial charging period, which is often between 3 and 20 s [5]. The charge acceptance is mainly limited by the negative electrode due to a slow charge reaction resulting from its low specific surface area and porosity in comparison to the positive electrode. Another reason for the charge acceptance limitation is attributed to the progressive accumulation of lead sulfates at the negative electrode during PSoC operations [6,7].

In order to increase the performance of modern SLI batteries, for many years now, battery manufacturers introduced improved negative electrode formulations that include up to 2 wt. % carbon additives. Various studies have revealed the enhanced charge acceptance of LABs via the addition of small amounts and certain forms of carbon in the negative electrodes [8–11]. A variety of possible mechanisms how carbon can improve the performance has been proposed [8,12,13]. The impact of carbon on the electrochemical performance of LABs seems to be affected by several parameters including specific surface area, external surface area, particle size distribution, porosity, electronic conductivity and surface functional groups of carbon [10,14,15]. The selection of an ideal carbon additive and further optimization strongly depends on the determination of the most important carbon parameters. So far, LABs containing carbon additives do not possess the charge acceptance required by OEMs, while keeping the water loss still at minimum levels [1,16]. This is due to the increased hydrogen evolution reaction (HER) by the addition of carbon additives in the negative electrodes, leading to a water loss of LABs [17]. Therefore, in order to find or produce carbon additives that improve the DCA without accelerating the HER activity, the role of carbon additives needs to be further investigated.

So far, mainly structural properties of carbon materials have been investigated regarding their effects on increasing charge acceptance as well as cycle life of LABs [8,9,11,18]. Other properties of carbon materials such as their surface chemistry have attracted only minor attention. However, it is well known from other electrochemical applications like supercapacitors that carbon surface chemistry can influence the electrochemical activity significantly [19–21]. For instance, specific surface functional groups can be attributed to the improved performance of supercapacitors such as the double-layer capacitance [22].

In case of LABs, only few studies have been conducted to examine the effect of carbon surface functional groups. The results obtained from these studies reported conflicting findings. It was concluded that carbon blacks having lower pH might decrease the water loss during the overcharge of LABs [23]. However, another study revealed the enhanced charge acceptance as well as the inhibition of the hydrogen evolution reaction by using nitrogen-doped carbons [24], which is known to increase the pH of carbon [25]. Hence, a comprehensive study covering a wide range of carbon pH is not existing but essential to understand the influence of carbon surface chemistry and to relate its properties to the electrochemical activity as well as the battery performance.

Another challenging aspect in LABs is the lack of predictability and discrepancy for the DCA under long-term vehicle usage. At PSoC conditions, a significant reduction in DCA values is observed [26,27]. DCA cannot be sustained after several months of vehicle operation which hinders the fuel savings as well as low emission features [1]. Further, there is often an inconsistency between the long-term DCA of a battery in an operational life and the prediction obtained from the short-term DCA tests [28]. Batteries and active material compositions, showing superior DCA performance according to the short-term tests, generate a rather poor charge acceptance in long-term field tests. Due to these discrepancies between the real-world and laboratory tests, the general recommendation by battery experts is to not only investigate the standardized short-term DCA test but also test the DCA during a long-term real-world drive cycle. In order to accelerate the active material development, both short- and long-term tests need to be adapted in the laboratory cell-level.

According to the current research topics of LABs for micro-hybrid vehicles, standardized and reliable DCA tests on a laboratory scale as well as an understanding of the structure-property relationship for carbon additives are required in order to accelerate the active material development for LABs. Based on that, this thesis is concentrated on the two main aspects that are described in the following section.

1.2 Aim of the thesis

In order to produce LABs that help to lower CO_2 emissions, the material development for such batteries needs to be improved. To provide a faster and cost-efficient screening of materials, execution of electrical tests on a laboratory scale is necessary. As the current standardized DCA tests do not represent the results obtained from the real-world drive cycles, there is definitely a need for understanding the discrepancy between the DCA results in order to apply these tests for the selection of carbon additives. Therefore, this thesis aims on two specific topics.

Firstly, a validation of both short-term and long-term DCA tests on 2 V laboratory cells is focussed. This study also aims to improve the laboratory cell level measurement technology for dynamic charge acceptance regarding the investigation of carbon additives. To address this issue, it is crucial to apply carbon additives generating a remarkable difference in charge acceptance. For this purpose, five different carbon additives providing a variation in the specific external surface, ranging from 7 $m^2 g^{-1}$ to 159 $m^2 g^{-1}$, were included as additives in the negative plates of 2 V lead-acid cells. Both short-term (charge acceptance test 2 from SBA and DCA from EN) and long-term (Run-in DCA from Ford) DCA tests were executed on the lead-acid cells. Further understanding of the mechanism was studied by applying electrochemical methods like cyclic voltammetry and electrochemical impedance spectroscopy.

Secondly, this thesis aims to understand the impact of carbon surface functional groups on the electrochemical activity of the negative electrodes as well as the DCA of 2 V lead-acid cells. In order to address this topic, commercially available activated carbon was modified by different chemical treatments to incorporate specific surface functional groups in the carbon structure. A series of activated carbons having a broad range of pH between 2.5 to 11.1 was prepared, which were used as additives in the negative electrodes. The corresponding lead-acid cells were subjected to cyclic voltammetry and DCA test according to EN. Further, the physical and chemical properties of the functionalized carbon additives were intensively analyzed to establish a structure-property relationship with a focus on DCA.

The present thesis is structured in the following manner. Chapter 2 gives an overview of the basics of electrochemistry and electroanalytical methods as well as the working principles of lead-acid batteries with a focus on carbon materials for the negative active material. Chapter 3 presents the first main part of this thesis which is about the dynamic charge acceptance tests on laboratory cell-level. In this chapter, experimental methods like the preparation of negative electrodes with tailored DCA are first described and the results of characterization techniques as well as electrochemical and electrical tests are presented and discussed. The second main part of the thesis is presented in Chapter 4, which focuses on the influence of carbon surface chemistry on the negative electrodes. The preparation and various characterization methods of carbons as well as manufacture and electrical testing of laboratory cells are explained. Further, the characterization results of carbons as well as the electrochemical and electrical test results are illustrated and discussed. Chapter 5 gives a summary of the main findings and also provides an outlook for possible future work on this topic.

2 Theoretical background and state of the art

2.1 Basics of electrochemistry

This chapter provides a summary of the electrical double-layer and hydrogen evolution reaction in which the concept as well as models are described.

2.1.1 Electrical double-layer

When an electrode is brought into contact to a solution of electrolyte, the formed interfacial region is called the electrical double-layer (DL). The electrochemical measurements are greatly influenced by the electrical properties of the DL. When an electronic charge is established inside the electrode, inversely charged ions to that on the electrode will be attracted to the solution phase boundary. That means the DL contains two parallel layers of charge and the charge on the electrode surface will be balanced with that inside the solution [29–31].

The first model for the existence of the DL at the metal surface being in contact with an electrolyte solution was developed by Helmholtz. In this model, the existence of a compact layer of ions in contact with the charged metal surface is assumed [30]. The Helmholtz model is considered as incomplete since the thermal motion of the ions, e.g. a loss of ions from the compact layer, is not taken into account [29]. The next model described by Gouy and Chapman involves the influence of the thermal motion on the ions near an electrode surface. Their model contemplates a diffuse DL, including positive and negative ions, in an extended region near the electrode surface. The probability of an inner Helmholtz layer was not considered in this model. The most realistic model defined by Stern consists of the electrified solid-liquid interface including both Helmholtz layer and diffuse layer models [29,30].

The simplified final representation of the DL formed at the negatively-charged electrode surface is presented in Figure 1. Through van-der-Waals or coulombic interactions or even chemisorption, neutral molecules, ions as well as solvent dipoles may be adsorbed onto the surface of a metal electrode. Two planes named as inner and outer Helmholtz planes are assigned with the DL. The inner Helmholtz plane is placed at the center of the specifically adsorbed ions or behind the layer of adsorbed water. The outer Helmholtz plane is located at the center of the positively-charged cations [29,30].

The total DL capacitance, C_D, can be calculated by the sum of the compact, $C_{compact}$, and diffuse layer capacitances, $C_{diffuse}$

$$\frac{1}{C_D} = \frac{1}{C_{compact}} + \frac{1}{C_{diffuse}} \quad (1)$$

In case of the concentrated electrolyte solutions, the diffuse double-layer capacitance can be neglected and the DL capacitance can be predicted by the compact Helmholtz layer [29,31].

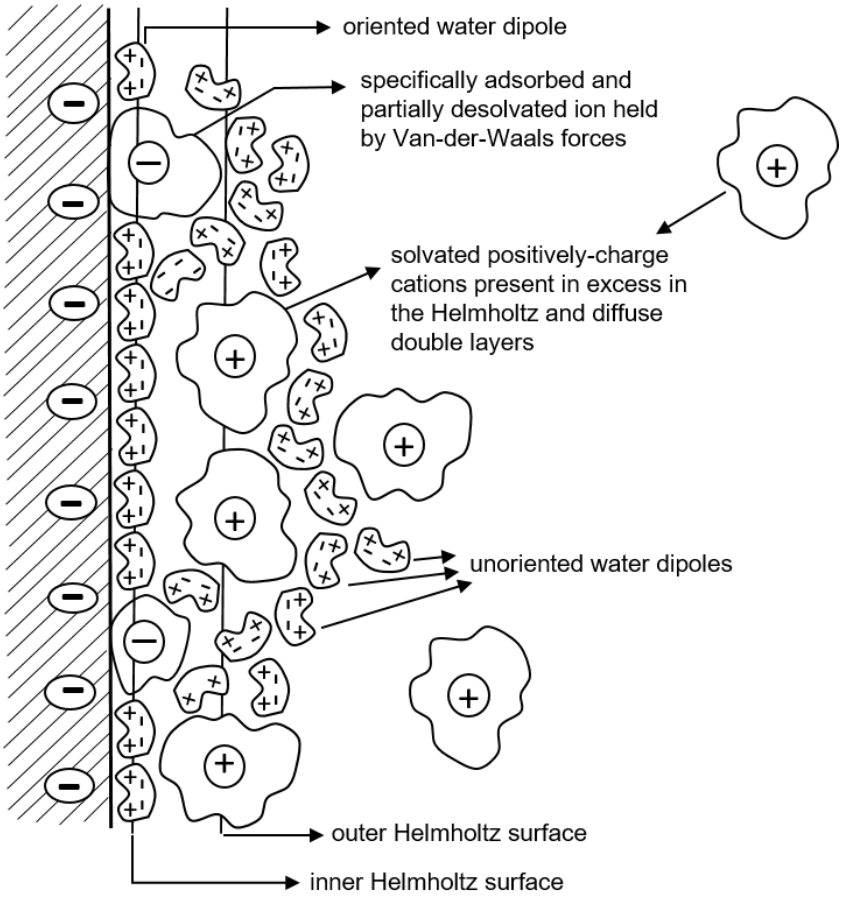

Figure 1: Schematic illustration of the double-layer formed at the negatively-charged electrode surface (the figure was redrawn based on reference [29]).

The electrolytic DL can be seen as a parallel plate capacitor. For such a capacitor, the charge on the plates, Q, can be calculated by multiplying the potential difference between the plates, $\Delta\varphi$, and the capacitance, C_D

$$Q = C_D \cdot \Delta\varphi \tag{2}$$

Regarding DL, Q represents the charge on the solution interface side and $\Delta\varphi$ stands for the potential difference between metal and solution interiors. It should be mentioned that in case of a zero Q, due to the solvent dipole layer at the electrode surface a potential difference between metal and solution will be still observed [29].

In electrochemistry, the differential capacitance, C_{DL}, is usually applied for a voltage alteration at a certain electrode potential instead of the integral capacitance, C_D. This is

due to the fact that in comparison to the parallel plate capacitor, the capacitance of the electrolytic layer is not necessarily constant over the whole potential range. The variation in the potential might result in the rearrangement of the solvent dipole layers or the adsorption or desorption of ions.

The capacitance charging current, i_C, can be expressed as the following equation, where its relationship to the differential capacitance, C_{DL}, and a linear potential increase, $d\varphi \cdot dt^{-1}$, is established [29].

$$i_C = \frac{dQ\,(\varphi)}{dt} = \frac{dQ}{d\varphi} \cdot \frac{d\varphi}{dt} = C_{DL} \cdot \frac{d\varphi}{dt} \tag{3}$$

2.1.2 Hydrogen evolution reaction

The hydrogen evolution reaction (HER) is the cathodic reaction in the electrochemical water splitting. This reaction occurs at the electrode surface forming gaseous hydrogen and can take place in acidic and alkaline solutions. The HER consists of a multi-step electrochemical process which is known as Volmer, Heyrovsky and Tafel steps. The accepted reaction mechanisms in acidic and alkaline solutions are given below [32–34]:

- Volmer reaction: electrochemical hydrogen adsorption

$$H^+ + M + e^- \rightleftharpoons M\text{-}H^* \text{ (acidic solution)} \tag{4}$$

$$H_2O + M + e^- \rightleftharpoons M\text{-}H^* + OH^- \text{ (alkaline solution)} \tag{5}$$

followed by

- Heyrovsky reaction: electrochemical desorption

$$M\text{-}H^* + H^+ + e^- \rightleftharpoons M + H_2 \text{ (acidic solution)} \tag{6}$$

$$M\text{-}H^* + H_2O + e^- \rightleftharpoons M + OH^- + H_2 \text{ (alkaline solution)} \tag{7}$$

or followed by

- Tafel reaction: chemical desorption or recombination reaction

$$2M\text{-}H^* \rightleftharpoons 2M + H_2 \text{ (acidic and alkaline solutions)} \tag{8}$$

in which H* represents a hydrogen atom chemically adsorbed on an electrode surface [32]. The represented reaction pathways are strongly influenced by the electrochemical, chemical and physical properties of the electrode surface. The kinetics of the overall

reactions are evaluated by the rate-determining step and can be determined by the Tafel slopes [17,32,34,35]. Depending on the rate-determining step, Bockris and Potter have summarized the Tafel slopes values of the HER obtained from Butler-Volmer kinetics [36]. If the adsorption of hydrogen (Volmer reaction) is the rate-determining step, the Tafel slope is 118 mV dec^{-1}. In case the electrochemical desorption (Heyrovsky) or recombination reaction (Tafel) is the rate-determining, the Tafel slope is 39 mV dec^{-1} or 29 mV dec^{-1}, respectively [36].

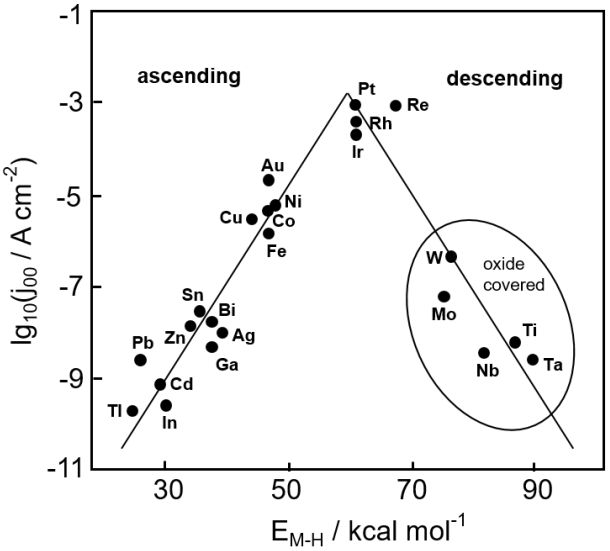

Figure 2: Volcano plot for the hydrogen evolution reaction in acidic solutions, in which j_{00} and $E_{M\text{-}H}$ denote the exchange current density and the energy of hydride formation, respectively (the figure was redrawn based on reference [37,38]).

Hydrogen adsorption and desorption on the electrode surface are two main steps of the HER, although both terms are competitive with each other. A metal surface having too weak bond strength with hydrogen leads to desorption before initiation of the HER. On the other hand, strongly bonded hydrogen on the metal surface would not be easily recombined into the product. Therefore, a metal surface could provide a high reaction rate for the HER, if it provides “not too strong, nor too weak” binding of intermediates [32]. This phenomenon is in line with the Sabatier principle which suggests that ideal catalytic activity can be obtained via having intermediate bonding energies with intermediates [39]. Trasatti established the first volcano curve for the HER (Figure 2), which represents the relationship between the exchange current density (j_{00}) and the equilibrium potential ($E_{M\text{-}H}$) [37]. As seen in Figure 2, Platinum groups metals (Pt, Rh, Ir) are the best electrocatalysts that exhibit the highest exchange current density for the HER. This model from Trasatti is the simplified one, which is often used to describe the HER activity.

2.2 Electroanalytical techniques

In this chapter, the fundamentals of the two mainly electroanalytical methods used in this work, cyclic voltammetry and electrochemical impedance spectroscopy are described.

2.2.1 Cyclic voltammetry

Cyclic voltammetry (CV) is a dynamic electrochemical method to investigate the reduction and oxidation processes of molecular species. It characterizes electrochemically active masses and provides information regarding a potential range of activity, mass transport, kinetics and reversibility of the reaction. Further, it can help to identify the different redox couples and phases taking place during the charge and discharge processes of an electroactive material [40–42].

A general reduction process at the surface of the electrode can be represented as

$$A + e^- \rightleftharpoons B \tag{9}$$

In a cyclic voltammetry study, the potential is scanned linearly with time from a defined starting potential, E_i, to a more negative potential, E_v. At the starting potential, species A is stable and at the vertex potential, E_v, species B is formed. When the potential is swept back to the initial potential, electron transfer occurs in the opposite direction and species A is reformed. This waveform of the potential during a CV experiment is shown in Figure 3 [43].

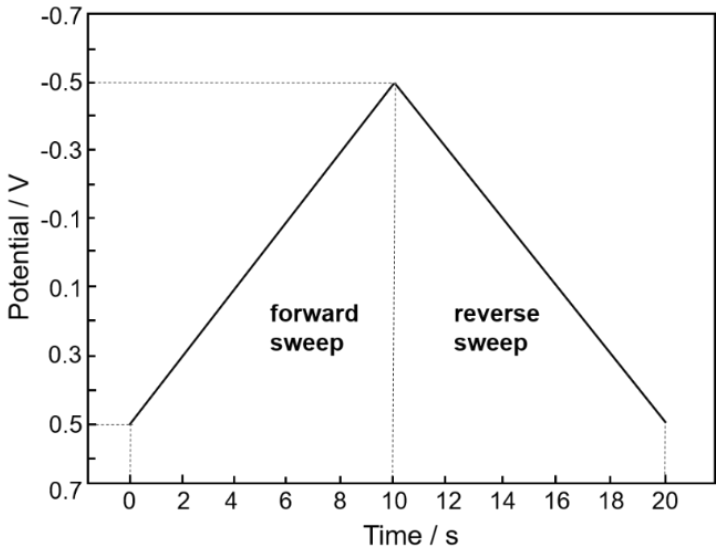

Figure 3: The potential waveform during a cyclic voltammetry study, where the initial potential, E_i is 0.5 V, the vertex potential, E_v, is -0.5 V and the scan rate, ν, is 0.1 V s^{-1} (the figure was redrawn based on reference [43]).

Throughout this process, the current response, *I*, is obtained from the applied potential at a fixed scan rate. A plot of the obtained current with respect to the potential gives a characteristic cyclic voltammogram for a diffusion-limited reaction, which is presented in Figure 4 [43].

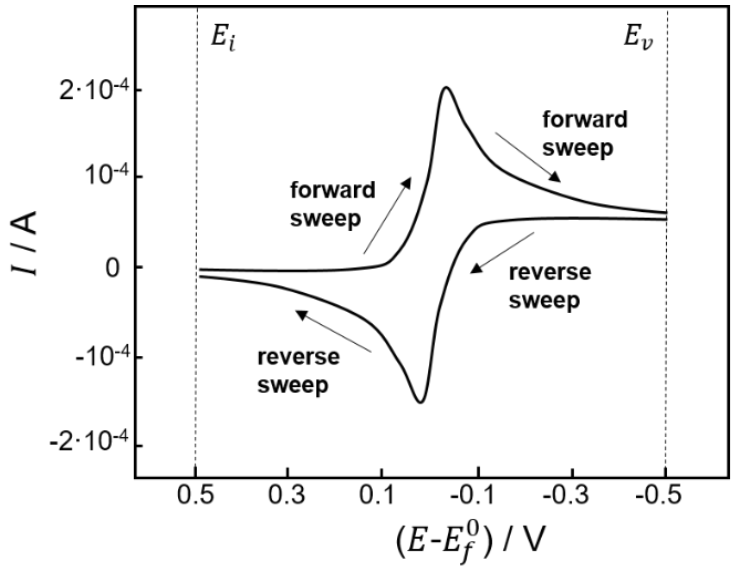

Figure 4: A typical cyclic voltammogram showing the current-potential relationship (the figure was redrawn based on reference [43]).

The CV is a powerful method since the obtained peak shape enables a direct fingerprint of the properties of the reduction and oxidation processes. The peak position and its shape provide essential information regarding the nature of the chemical species as well as the electrochemical processes occurring on the electrode surface. With the help of a voltammogram shape, the reversibility of an electrochemical reaction can be determined [43].

The electrochemical reversibility depends on the rates of electrode kinetics compared to the rate of mass transfer. If the kinetics of the electron transfer, k^0, are fast in comparison to the rate of mass transport, m_t, ($k^0 >> m_t$), Nernst equation defines the dependence of the equilibrium potential on the surface concentration of species, C^s_{ox} and C^s_{red}, at the electrode

$$E = E^0 + \frac{RT}{nF} \ln \frac{(C^s_{ox})}{(C^s_{red})} \qquad (10)$$

where E^0 is the formal potential of the reaction, F is Faraday´s constant, R is the universal gas constant, n is the number of exchanged electrons and T is the temperature [29,43,44].

In case, the electrode kinetics is slow (k^0 << m_t), the following equation relates the dependence of surface concentrations on the potential

$$i = i_0 \left\{ \frac{C_{ox}^s}{C_{ox}} \exp\left[-\frac{\alpha F}{RT}\eta \right] - \frac{C_{red}^s}{C_{red}} \exp\left[\frac{(1-\alpha)F}{RT}\eta \right] \right\} \quad (11)$$

where i_0, α and η, exchange current, transfer coefficient and overpotential. C stands for bulk concentrations, whereas C^s is surface concentrations of the species.

If the surface concentrations are similar to the bulk ones, the equation 11 is simplified to the Butler-Volmer equation [29,43,44].

$$i = i_0 \left\{ \exp\left[-\frac{\alpha F}{RT}\eta \right] - \exp\left[\frac{(1-\alpha)F}{RT}\eta \right] \right\} \quad (12)$$

Matsuba and Ayabe introduced the parameter, called Matsa number (Λ), in order to distinquish the validity of the equations 10 and 12 regarding fast and slow electron transfer.

$$\Lambda = \frac{k^0}{m_t} = \frac{k^0}{\left(\frac{nF}{RT} D\right)^{1/2} \cdot \nu^{1/2}} \quad (13)$$

where, k^0 m_t, D and ν are the electron-transfer rate constant, rate of mass transport, the diffusion coefficient and scan rate, correspondingly [29].

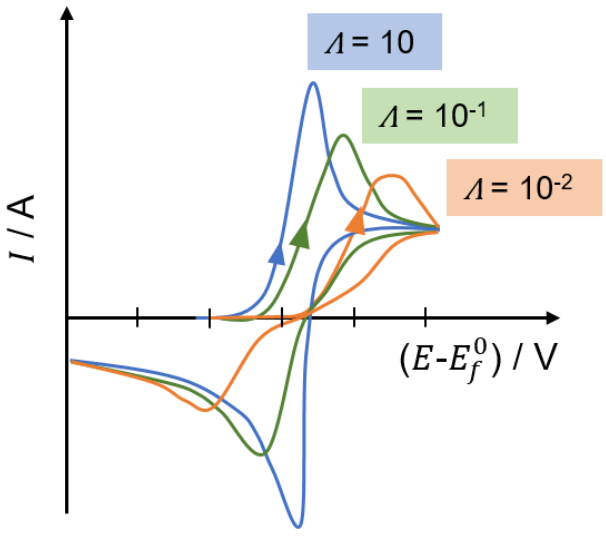

Figure 5: Cyclic voltammograms for three different Matsa numbers (the figure was redrawn based on reference [43]).

The principles of diffusion and electrode kinetics explain the shape of the voltammogram, which identifies whether the electrochemical reaction is reversible, quasi-reversible or irreversible. The process is reversible when the Matsa number is much larger than 15 or the rate constant is much larger than $0.3\ \nu^{1/2}$. For the Matsa number values between 15 and 10^{-3} or the rate constant values between 0.3 and $2 \cdot 10^{-5}\ \nu^{1/2}$, the voltammogram is quasi-reversible. In case of the irreversible processes, the Matsa number is much lower than 10^{-3} or the rate constant is much lower than $2 \cdot 10^{-5}\ \nu^{1/2}$ [29,43,44]. The influence of the reversibility on the shape of CVs is presented in Figure 5.

2.2.2 Electrochemical impedance spectroscopy

Electrochemical impedance spectroscopy (EIS) is a technique to determine the impedance spectrum of an electrochemical system. It is widely used for the investigation of complex electrochemical systems, which can determine the electrochemical processes and dynamic behavior of batteries [30,45].

The most commonly used method in EIS measurements includes the execution of a sinusoidal signal with a low amplitude and a controlled frequency. Afterwards, a transient response is obtained at which the amplitude ideally has a linear variation with respect to the input signal. In order to obtain this linearity, the amplitude of the input signal should be sufficiently low. Considering such conditions, the sinusoidal response is obtained, which provides the same frequency as the input signal. As a result, the impedance is expressed as a function of the frequency [46]. Two types of EIS can be used to determine the complex impedance. In the galvanostatic EIS, the alternating current (ac) of a defined frequency is applied and the ac voltage response is obtained. In terms of the potentiostatic EIS, the ac voltage is used as an input. Considering the EIS of batteries, the galvonastatic technique is widely used in order to control the state of charge [47]. The complex impedance as a function of frequency, $Z(f)$, can be calculated according to equation 14. The current, *i,* and voltage, *u*, can be written as the amplitudes *I* and *U* as well as the phases ϕ_i and ϕ_u, respectively [47].

$$Z(f) = \frac{u}{i} = \frac{U \cdot e^{j2\pi ft + \phi_u}}{I \cdot e^{j2\pi ft + \phi_i}} = Z \cdot e^{j2\pi ft + \phi} = \mathrm{Re}(Z) + j \cdot \mathrm{Im}(Z) \qquad (14)$$

The impedance spectrum can be visualized on either a Bode plot which presents the relationship between the complex impedance amplitude (Z) or the impedance phase (ϕ) and the frequency (f). Another way to present the impedance spectrum is the Nyquist plot, where the imaginary part of the impedance, -Im (Z), is plotted with respect to the real part of the impedance, Re (Z) [46]. The Nyquist plot is often used to identify an equivalent circuit model (ECM) for the investigation of the impedance behavior of electrochemical systems for batteries [46,47]. The following paragraphs describe the elements which can be found in ECM.

Ohmic resistance and inductance

A battery has an ohmic resistance, which is called internal resistance (R_i). The internal resistance is always present due to the limited conductivity of the battery terminals, electrodes and electrolyte. Several factors such as state of charge, age and history influence the ohmic resistance, which is resulted from morphological as well as chemical changes in the active material, electrolyte and grid. In case of a frequency range covering all electrochemical reactions shunted by the double-layer capacitors, the real part of the impedance provides the internal resistance. The phase angle in this frequency range is zero. Therefore, the internal resistance can be measured since the modulus of the impedance is almost the same as its real part [48]. For instance, around 10 Ah valve-regulated lead-acid batteries possess the real-axis intersection, where Im (Z) = ϕ = 0, at 1 kHz [49].

Considering sufficiently high-frequency ranges, the imaginary part of the impedance provides positive values. This generally shows a linear proportionality to the frequency, in case of a constant real part [49,50]. A model to this observation is introduced by a constant inductance, L, with the internal resistance as well as all capacitive elements. When the ECM consists of a series connection L–R_i–C_{DL}, the impedance can be calculated according to the equation below

$$Z(f) = R_i + j \cdot \left(\omega L - \frac{1}{\omega C_{DL}}\right) \tag{15}$$

where ω and C_{DL} are angular frequency and double-layer capacitance. It is assumed in equation 15 that all faradaic processes are shunted by DL capacitors and the series connection of capacitances are described as C_{DL} [48].

Charge transfer resistance

The discharge reaction of lead-acid batteries includes the oxidation of the metallic lead at the negative electrode and the reduction of lead dioxide at the positive electrode (shown in chapter 2.3.1). In these reactions, the transfer of two electrons takes place. The mechanism in these reactions depends on the electrode potential and the electrolyte concentration [48]. Different reaction mechanisms and models are widely discussed for both positive and negative electrodes [51–55]. In terms of the rate-determining step, transfer of lead ions (or protons), crystal growth or adsorption might be the one rather than the electrochemical charge transfer process [48].

Furthermore, side reactions such as hydrogen and oxygen evolution occur in lead-acid batteries since water is not thermodynamically stable at the equilibrium potential (further explained in chapter 2.3.1). The mechanism of the oxygen evolution reaction is discussed in the following reference [56]. Considering the hydrogen evolution reaction

on lead, the rate-determining step might be the charge transfer, which is often valid for metal electrodes in acid solutions [54].

Double-layer capacitance

The description and model for the electrical double-layer can be found in chapter 2.1.1. For metal electrodes, the charge on the double-layer capacitor can be positioned directly at the interface because of high electron mobility [48]. Regarding this phenomenon, lead dioxide can be considered as a metal electrode due to its relatively high conductivity [57].

Putting together the charge-transfer resistance, R_{CT}, and the DL capacitance, R_{DL}, a parallel combination of R_{CT} and C_{DL} can be considered for the representation of an electrode. The current is distributed between a capacitive current, I_C, and a faradaic current which crosses R_{CT}.

A capacitive semicircle is present for the impedance of a parallel combination of resistor-capacitor. The impedance at high frequencies is close to the real axis, which provides the ohmic resistance. Considering low frequencies, the impedance curve reaches to the real axis as well. The semicircle diameter is equal to the paralleled resistor. Based on this, the impedance amplitude of resistor-capacitor, Z_{RC}, can be calculated according to the equation below [48].

$$\frac{1}{Z_{RC}} = \frac{1}{R} + j \cdot (\omega C) \tag{16}$$

Warburg impedance

The sulfuric acid is consumed during the discharge process of lead-acid batteries, which is followed by a diffusion process [48]. The Warburg impedance obtained from a solution of Fick´s second law represents the diffusion limitation in the impedance term [30,58]. Figure 6 presents the three different types of Warburg impedances, Z_W, considering the one-dimensional diffusion. If the diffusion length reaches the thickness of the diffusion region at lower frequencies, the straight-line behavior (45 °) of the complex impedance changes into a semicircle (Figure 6b), which represents a parallel combination of capacity (C) and diffusion resistance (R_d). When the complete blocking of diffusion occurs at the end, where no direct current (dc) flows in the system, a vertical line at low frequencies can be observed, which is only related to the capacity (Figure 6c). At this region, resistance and capacity are in series connected [30].

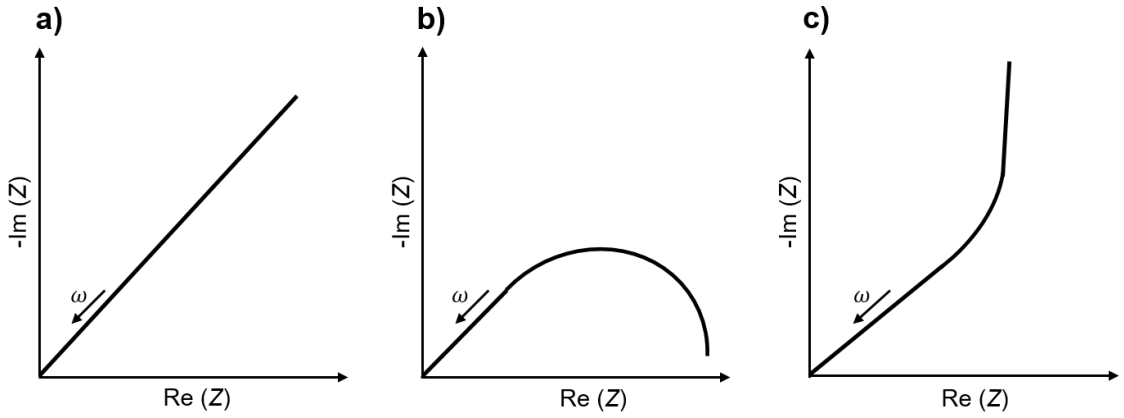

Figure 6: Nyquist plots of Warburg impedance for a) semi-infinite diffusion; b) limited diffusion layer with a transmissive boundary condition; c) limited diffusion layer with a reflective boundary condition (the figure was redrawn based on references [48,59]).

Randles equivalent circuit

In case the electrode is controlled by the elements described above, the Randles equivalent circuit can be used to define the electrical behavior of the electrode [48,60]. The Nyquist plot and the equivalent circuit model are presented in Figure 7. The presented model contains only charge transfer and diffusion limitation. At higher frequencies, the semicircle ($R_{CT}C_{DL}$) is present. In case of lower frequencies, the Warburg tail is observed. Considering a battery, its electrodes shall be connected in series. If both electrodes in the battery correspond to the ECM presented in Figure 7b, it is possible to add the inductance (L) and internal resistance (R_i). However, complex capacitive curves are obtained considering the charge transfer resistance (R_{CT}), double-layer capacitance (C_{DL}) and Warburg impedance (Z_W) of both electrodes. As a result, the electrode kinetics cannot be easily derived from the impedance spectrum [48].

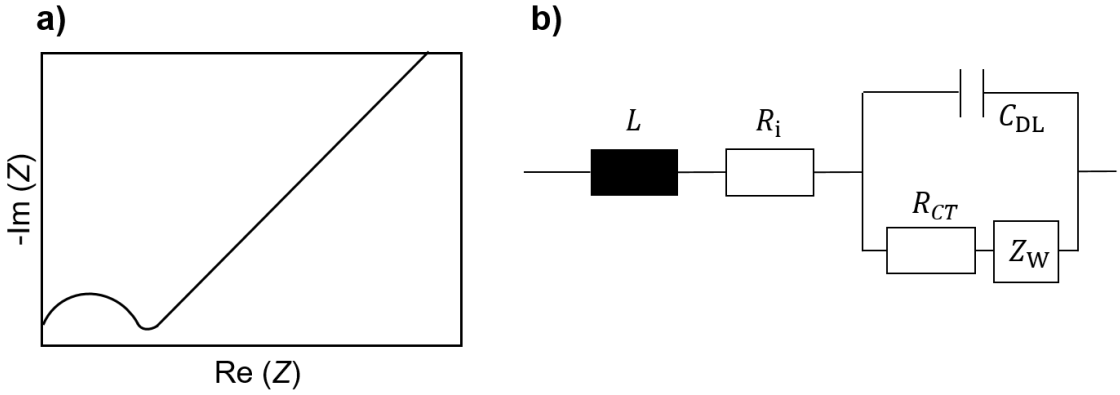

Figure 7: a) Nyquist plot and the corresponding b) Randles circuit of an electrochemical half-cell (the figure was redrawn based on reference [48]).

2.3 Lead-acid batteries

In 1859, Gaston Planté reported that during charging the two lead plates immersed in aqueous sulfuric acid solution, a discharge current could be obtained. Afterwards, in 1860, he presented the first rechargeable lead-acid battery consisting of parallel-connected series of nine cells, which was considered as the invention of the lead-acid battery [1,2,61,62].

Depending on the application field, different types of lead-acid batteries are used in automobile, transport and telecommunication industries. For example, SLI batteries in automobiles, stationary batteries in backup power supplies and traction batteries in power in-house transport vehicles are widely used. Despite its low specific energy, hundreds of millions of such batteries are produced worldwide and they can be found in a wide application range as mentioned above. This is due to the fact that lead-acid batteries provide advantages in comparison to the other battery technologies. The most important factors are the economic and safety issues. The manufacture of such batteries is easy and practical. The battery materials are almost 95% recyclable [2]. On the other hand, since lead is toxic, its emission has certain hazards both to the environment and human health [63].

In the following subchapters, the thermodynamics and working principle of the lead-acid batteries are explained. Further, the concept of dynamic charge acceptance as well as carbon additives used for the negative electrode optimization are overviewed.

2.3.1 Thermodynamics and working principle

The relationship between the equilibrium potential of a redox reaction and pH is provided by so-called Pourbaix diagrams [64]. Figure 8 shows such a diagram for the $Pb/H_2SO_4/H_2O$ system. The stability regions of the solid phases are restricted by the continuous lines. Each line shows the equilibrium potential of the electrochemical reaction occurring between the two adjacent phases. The dashed lines define the stability regions of Pb^{2+}, $HPbO_2^-$ and PbO_3^{2-} ions. The dependence of the equilibrium potentials of the hydrogen and oxygen electrodes on the pH of a solution is delimited by the dashed-and-dotted lines.

It can be seen that at low pH values the equilibrium potential of the $Pb/PbSO_4$ electrode is much more negative than that of the H^+/H_2 electrode. According to that, it is expected that the HER to occur significantly during battery charge. However, this does not happen due to the high overpotential of the hydrogen evolution on the Pb surface. Only at very negative potentials, the HER provides a non-negligible current. In case of the H_2O/O_2 and $PbO_2/PbSO_4$, a similar case is also present. Mainly, the oxidation of $PbSO_4$ to PbO_2

proceeds because of the high overpotential of the oxygen evolution reaction on PbO_2. Only at more positive potentials, significant oxygen evolution reaction (OER) occurs [2].

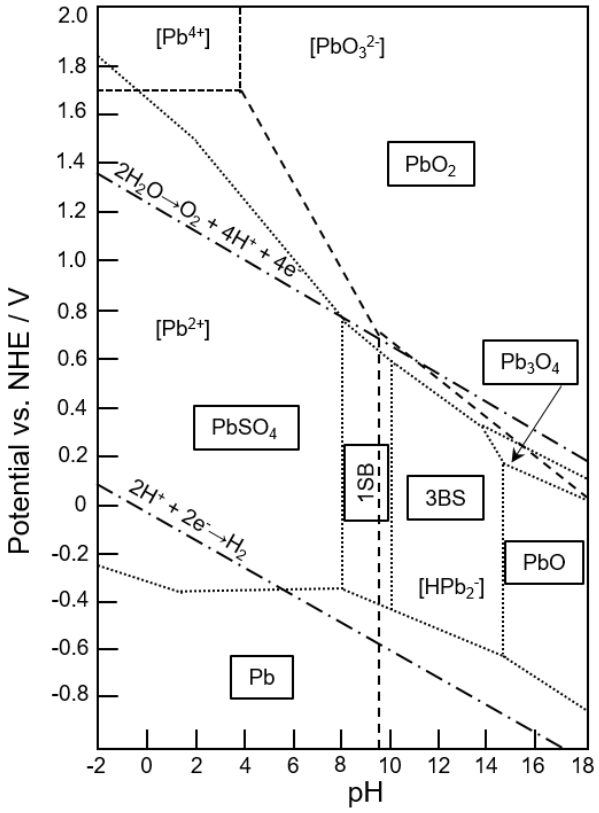

Figure 8: Equilibrium potential/pH diagram for the $Pb/H_2SO_4/H_2O$ system at 25 °C (the figure was redrawn based on reference [2]).

In contrast to other battery systems, the electrolyte in lead-acid batteries is also an active material, which takes a part in the generation and accumulation of the electric energy. Depending on the application, the relative density of sulphuric acid typically is around 1.3 g ml^{-1} at the fully charged state and reduced to around 1.1 g ml^{-1} at discharged state [2,65]. Therefore, the state of charge (SoC) of the battery influences the pH of the system as well as the electrode potentials. A significant influence of the pH of the system on the phases can be seen in Figure 8.

Negative electrode

At a fully charged state, the negative electrode consists of spongy lead skeleton immersed in diluted sulfuric acid. During discharge, the oxidation of Pb to $PbSO_4$ occurs and during charge the reduction of $PbSO_4$ to Pb proceeds [2,65]. The main redox reaction taking place on a lead electrode and the corresponding Nernst equation is shown below

$$Pb + HSO_4^- \rightleftharpoons PbSO_4 + H^+ + 2e^- \quad (17)$$

$$E = -0.302 - 0.029\,pH - 0.029 \lg a_{HSO_4^-} \quad (18)$$

which indicates that the equilibrium potential depends on the pH of the solution [2]. The reversibility of the $Pb/PbSO_4$ redox pair depends on the electrochemical history of the electrode as well as the density of the electrolyte. It is known that the size and number of the $PbSO_4$ crystals strongly influence the charging reaction of the Pb electrode. Additionally, the concentration of sulfuric acid affects the solubility of $PbSO_4$ which has an impact on the saturation concentration of Pb^{2+} ions [27]. After strong charge pulses, it is possible to obtain locally high sulfate concentrations which decrease the conversion of $PbSO_4$ to Pb. The dissolution of the lead ions is the rate-determining step here [66].

The mechanism of the $PbSO_4$ formation on the negative electrode is proposed by Pavlov et al. [8,67]. The processes taking place on the negative electrode is represented in Figure 9. During the discharge process, small $PbSO_4$ crystals are formed on the surface of Pb. These small crystals have high solubility and Pb^{2+} ions are formed, which is involved in the following charge process (process A). However, some parts of the Pb^{2+} ions participate in the growth of the big $PbSO_4$ crystals (process B). These big crystals have low solubility and therefore have only a minor contribution in the charge process (process A*). Hence, the big $PbSO_4$ crystals continue to grow further which results in rapid sulfation of the negative electrodes. The precipitation of the unreduced $PbSO_4$ crystals onto the Pb surface leads to a reduction in the charge acceptance of negative electrodes [67].

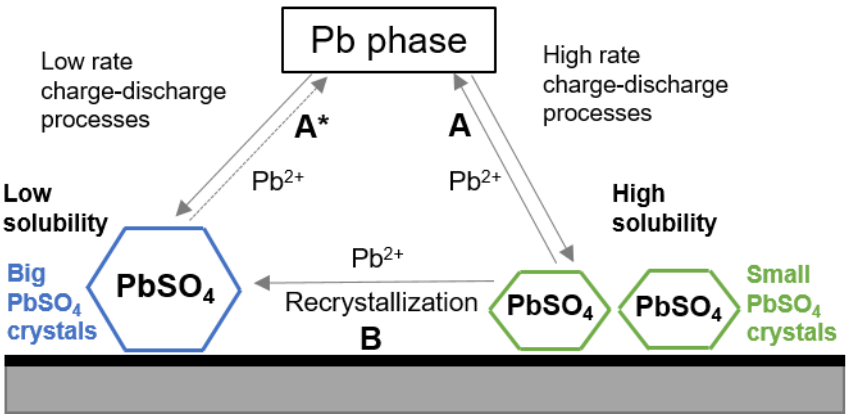

Figure 9: Schematic representation of the processes taking place at the negative electrode during charge and discharge (the figure was redrawn based on reference [8,67]).

In addition to the presented main reaction above, side reactions occur on the lead surface as well which are hydrogen evolution reaction and oxygen recombination reaction (ORR). The HER and the respective Nernst equation are presented below

$$2H^+ + 2e^- \rightleftharpoons H_2 \quad (19)$$

$$E = -0.059\ pH\ -\ 0.029\ \lg P_{H_2} \quad (20)$$

where P_{H_2} is the hydrogen pressure [2]. The HER during overcharge can decrease the electrolyte amount which might lead to a loss of active material contact with the liquid phase. This phenomenon could increase the internal resistance of the battery [1].

The second side reaction at the negative plate, the ORR, results in the generation of water. The ORR occurs during overcharge when the evolved oxygen at the positive electrode diffuses to the negative electrode and the diffused oxygen reacts with the spongy lead. The oxygen is converted to water via two steps as shown below [2].

$$O_2 + 2H^+ + 2e^- \rightleftharpoons H_2O_2 \quad (21)$$

$$H_2O_2 + 2H^+ + 2e^- \rightleftharpoons H_2O \quad (22)$$

Figure 10 presents the current-potential curves of the main and side reactions occurring on the negative electrode. The electrochemical oxidation and reduction, taking place on the $Pb/PbSO_4$ redox pair, proceed with slight polarization meaning that it is nearly reversible. The hydrogen evolution potential possesses more negative values than the potential of $PbSO_4$ reduction to Pb [2]. Thus, the electrolyte decomposition occurs only at very high polarization of the electrode such as during battery overcharge. The current contribution of the ORR is considered to be diffusion-limited. Therefore, the potential of the ORR does not depend on the working potential range of the negative electrode [68–70]. Figure 10 presents the current-potential curves of the main and side reactions taking place on the negative electrode.

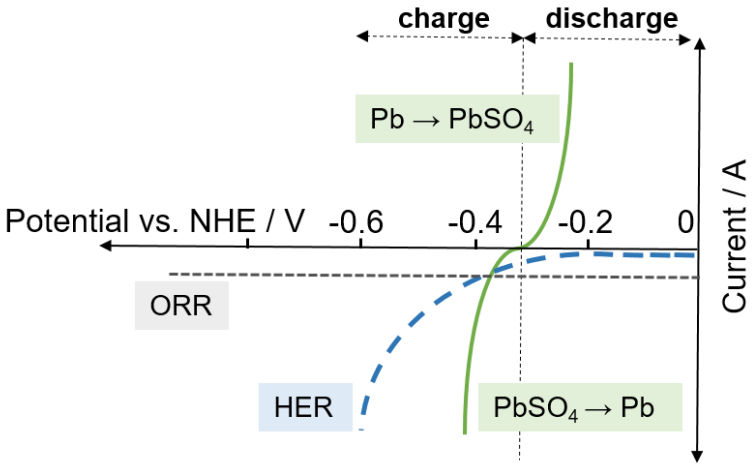

Figure 10: Current-potential relationship for the negative electrode in lead-acid batteries (the figure was redrawn based on reference [65,71]).

Positive electrode

The positive electrode of lead-acid cells at a fully charged state consists of porous PbO_2. During discharge $PbSO_4$ crystals are formed. During the charge process, the oxidation of $PbSO_4$ occurs. The main redox reaction as well as the corresponding equilibrium potential obtained from the Nernst equation are shown below.

$$PbO_2 + HSO_4^- + 3H^+ + 2e^- \rightleftharpoons PbSO_4 + 2H_2O \quad (23)$$

$$E = 1.628 - 0.088\,pH + 0.029 \lg a_{HSO_4^-} \quad (24)$$

Besides the main reaction, the OER takes place on the positive electrode. The electrochemical reaction as well as the respective equilibrium potential are presented below

$$H_2O \rightleftharpoons O_2 + 4H^+ + 4e^- \quad (25)$$

$$E = 1.228 - 0.059\,pH + 0.029 \lg a_{H_2O} + 0.015 \lg P_{O_2} \quad (26)$$

where P_{O_2} is the partial pressure of oxygen. It can be seen that the equilibrium potential of the OER is lower than the main redox reaction. Due to the kinetic hindrance of the OER similar to the HER, this side reaction starts to take place at higher potentials. Therefore, the high overpotential of the OER enables the positive electrode to be recharged before a considerable amount of oxygen is evolved [1,2].

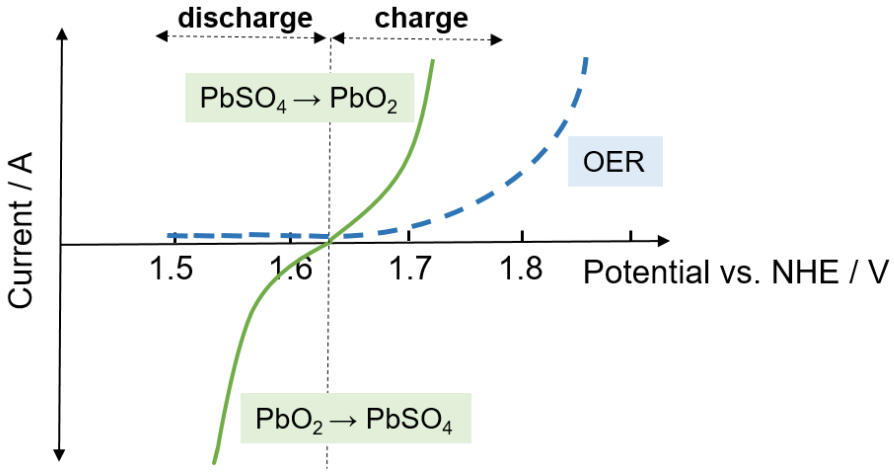

Figure 11: Current-potential relationship for the positive electrode in lead-acid cells (the figure was redrawn based on reference [2,72]).

Figure 11 represents the current-potential curves of the main and side reactions proceeding on the positive electrode. It can be seen that electrochemical oxidation and reduction of the $PbO_2/PbSO_4$ redox pair occur at a low electrode polarization. On the

contrary, the oxygen evolution potential possesses much more positive values. Therefore, during anodic polarization, $PbSO_4$ to PbO_2 reaction takes place first and the OER proceeds only for high overpotentials [2].

Lead-acid cell

Based on the reactions taking place on negative and positive electrodes, the overall reaction and the open circuit potential (E_0) are expressed below.

$$Pb + PbO_2 + 2H_2SO_4 \rightleftharpoons 2PbSO_4 + 2H_2O \quad (27)$$

$$E_0 = 2.041 - 0.059 \lg (a_{H_2SO_4} / a_{H_2O}) \quad (28)$$

The nominal voltage of a cell at pH=0 is 2.041 V which depends on the concentration of the sulfuric acid solution.

Figure 12 presents the construction of a 12 V commercial lead-acid battery. The represented battery comprises six individual cells connected in series with lead connectors. The positive and negative plates in a cell are isolated by microporous separators which allow the ion transfer. The plates of a cell consist of an active mass that is filled during the pasting process into a current collector, known as grid. The cells are filled with a 35-40 % H_2SO_4 solution as electrolyte which has high electrical conductivity and low freezing point [1,2].

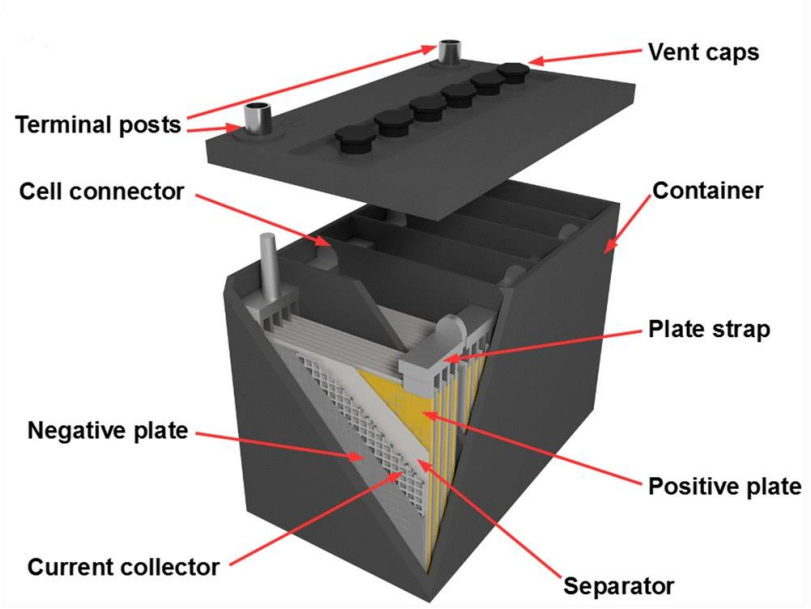

Figure 12: A schematic representation of a lead-acid battery (the figure was reproduced based on reference [73], http://creativecommons.org/licenses/by/4.0/).

2.3.2 Dynamic charge acceptance

Lead-acid batteries in micro-hybrid vehicles are operated mainly at PSoC operations due to the stop/start events and brake energy recuperation function [74]. For the evaluation of the rechargeability of a battery after different histories at PSoC operations, Karden et al. introduced the definition of “dynamic charge acceptance” [75]. The DCA is defined as the average charging current during regenerative braking in a specified time range. The obtained DCA value is divided to the nominal capacity of the battery in order to compare the DCA of different sizes of batteries [74]. The battery possessing high DCA would provide several benefits. For example, the fuel consumption and CO_2 emissions could be reduced by decreasing alternator torque during fuelled engine operation. Further, such high DCA batteries enhance stop/start availability because of faster recharge-ability especially in urban traffic and at winter temperatures. Moreover, in micro-hybrid and PSoC operations, high DCA performance could enable weight reduction and battery downsizing [1].

The DCA of lead-acid batteries is generally between 0.5 and 1.5 A Ah^{-1} [76]. The DCA value is required to be in the range of 2 A Ah^{-1} over the whole battery life in order to improve fuel economy as well as reduction of emissions [1]. However, it has been shown that the DCA reduces quickly to around 0.1 A Ah^{-1} during real-world application which is especially obtained after longer parking periods [27,77].

There are several parameters affecting the DCA of the batteries. During discharge, $PbSO_4$ crystals are formed on both negative and positive electrodes. In PSoC operations, the formed $PbSO_4$ crystals are often larger and they are much more difficult to dissolve in comparison to a fully-charged state. The reason for the decrease of DCA is not completely understood yet. Still, as mentioned above, the charge process is dependent on the dissolution of $PbSO_4$ crystals. As the dissolution process depends on several parameters, the DCA is probably influenced by the same factors such as time, temperature, the concentration of ions in the electrolyte as well as crystal surface area [1,26,78,79]. The main impact factors on DCA are described in the following paragraphs.

Partial state-of-charge operations

The main failure reason at PSoC operations is the irreversible sulfation on the surface of the negative electrode since $PbSO_4$ crystals are not completely or rarely recharged back to lead [80]. The progressive growth of the $PbSO_4$ crystals is taking place via the “Ostwald Ripening” process [81]. Therefore, a capacity loss is observed due to a decrease of the active surface area during the charge process which inhibits obtaining high DCA values [74].

State-of-charge

It is known that low SoC leads to an increase of DCA values due to the presence of higher active surface area of $PbSO_4$ crystals at low SoCs to be transformed back to lead. Budde-Meiwes [74] has tested the DCA of batteries after charge and discharge history at various SoCs (40, 50, 60, 70, 80, 90 and 100% SoC). It has been shown that with an increase of SoC, the recuperation currents obtained after charge and discharge history become lower [74].

Short-term history (charge, discharge, rest period)

The DCA is much lower after a precious charge event than after a discharge event. Sauer and co-workers [82] studied DCA testing with short-term history at 90% SoC. It was found that the DCA obtained after discharge history possesses more than twice as high or in few cases even 5 times higher values compared to charge history. Furthermore, it was observed that the longer test periods decrease the recharging currents [79,82]. The recrystallization and growth of $PbSO_4$ crystals take place during longer rest periods as well, which deaccelerates the dissolution of such crystals [74].

Temperature

It has been shown that the DCA is remarkably pronounced at elevated temperatures [82]. This observation fits to the description of Bode which refers to an easier dissolution of $PbSO_4$ crystals at higher temperatures during charging [54]. It is possible that the saturation concentration is not reached at low temperatures since the dissolution rate is insufficient [74].

Acid stratification

There are two different findings about the impact of acid stratification on DCA. According to Sauer et al. [82] the DCA limitation is not mainly resulted from the acid stratification since the batteries, consisting of stirring electrolyte, also face poor charge and sulphation. In case of acid stratification, the charge process can occur at another area than where the material is freshly discharged [74]. As a result, lower DCA is obtained since the freshly discharge location is not used for the charge process. In another work, Kowal and coworkers [27] investigated the DCA of flooded SLI batteries during micro-cycling by simulation of a two-dimensional macrohomogeneous model. In that study, different current profiles were examined with respect to the current distribution during charging and discharging. It has been determined that at large current rates initial acid stratification enhances inhomogeneity in acid density as well as charge distribution. Further, micro-cycles are determined to homogenize acid density distribution, however,

the gradients in charge distribution increase as well. When charging is not homogeneous over the electrode, the DCA is significantly limited over thousands of micro-cycles.

2.3.3 Optimization of negative electrodes via carbon additives

As the charge acceptance of lead-acid batteries is mainly limited by the negative plate [8,14,83,84], attributed to rate-limiting steps including the progressive sulfation of $PbSO_4$ crystals in the negative plates [8], certain types of additives have been incorporated into the negative active mass. Various studies have revealed that the inclusion of small amounts of carbon additives can invest the negative electrode with enhanced charge acceptance since the carbon addition can overcome the tendency of sulfate accumulation [8,12,14,85–87]. The incorporation of additional carbon in the negative electrodes was first demonstrated by the study of Nakamura and Shiomi [88,89]. They showed that the carbon black addition retards mainly the sulphation of the negative electrodes during the simulated high-rate partial state of charge (HRPSoC) test for HEV applications.

In recent years, the reasons why carbon enhances battery performance is widely discussed. Still, more research and systematic studies are needed in this field. There are many types of carbon materials such as carbon black, activated carbon and graphite which have been used as additives in negative plates [9,11,90,91]. Within each type of carbon, there is a broad range of physical and chemical properties including: a) specific surface area; b) porosity; c) surface functional groups; d) particle size distribution and e) electrical conductivity, which influence the electrochemical activity of the corresponding negative electrode [14]. The influence of the parameters of carbon mentioned above on the performance of lead-acid batteries has been widely studied. As an example, the main findings of such studies are summarized in the following paragraph.

The specific surface area of the negative electrode has been determined as an important parameter, as it keeps the negative plate potential below the hydrogen evolution potential [92]. By using a high surface area carbon black additive, a reduction in the discharge capacity of lead batteries upon cycling was observed [93]. Pavlov and coworkers have demonstrated that the size of carbon particles influences the structure of the negative active material (NAM). It has been illustrated that nanosized carbon particles are incorporated in the bulk of the skeleton branches of the NAM. On the other hand, microsized carbon particles having high affinity to lead are integrated into the skeleton structure of the NAM [9]. Another study presented the influence of carbon surface functional groups on the hydrogen evolution activity of negative electrodes and the charge acceptance of the battery [24]. The DCA of lead-acid cells was improved via an increased external surface area of carbon additives. The improved performance was attributed to the enhanced DL capacitance of the negative plates [10].

The mechanism as well as the possible functions how carbon improves the electrochemical performance of lead-acid batteries have been briefly described [13,94] as follows: a) improvement of the overall conductivity of negative active mass; b) formation of small $PbSO_4$ crystals and restriction of $PbSO_4$ crystal growth; c) carbon acting as a capacitor to absorb charge current at high rates and d) reduction of the hydrogen overpotential and facilitating hydrogen emission.

As mentioned above, the usage of carbon as an additive in the negative electrode can improve the electrochemical performance of lead-acid batteries but its addition has also some limitations. The following paragraphs summarize the beneficial effects of carbon including studies supporting the possible mechanism of carbon listed above and the limitations of using carbon additives.

Beneficial effects of carbon

One of the beneficial contributions of carbon has been suggested as the improved conductivity of the negative active mass, which can enhance the recharge-ability. Since the $PbSO_4$ formed on the negative electrode is an insulator, the presence of carbon particles might provide a conducting path through $PbSO_4$ crystals. The conductivity of carbon depends on the graphitization degree as well as the surface functional groups [12,95–97].

Another possible function of carbon is known as the restriction of $PbSO_4$ crystal growth and the formation of $PbSO_4$ crystals. Studies have shown [87,98] that carbon can act as a steric hindrance to the $PbSO_4$ crystallization which helps to keep a high surface area to proceed electrochemical reactions. By restricting the crystal growth, taking place via “Ostwald Ripening”, the recharge reaction of $PbSO_4$ to Pb can be accelerated via carbon. This suggested mechanism was supported by another study [99] in which besides graphite, titanium dioxide particles as an additive can also improve the HRPSoC cycle life. Titanium dioxide is known to be a poor electronic conductor. Therefore, the enhanced performance via graphite cannot be attributed to its conductivity alone [12,13].

During high-rate charge processes, protons or solvated protons can be stored in an electrical double-layer by the capacitive component. When the negative active mass contains considerable amounts of carbons, carbon materials might act as the capacitive element. During the charge process at high rates, the electrical double-layer on the carbon surface is charged first. This non-faradaic charging occurs at potentials between the steady-state potential of the negative plate and the potential required for the hydrogen evolution. The electrical double-layer is discharged slowly in which the reduction of $PbSO_4$ to Pb takes place. Therefore, the capacitive contribution of carbon can support the charge/discharge events proceeding at high rates [12].

Limitations of carbon

One of the main limitations of carbon incorporation into the negative electrodes is the accelerated hydrogen evolution reaction during charging. This phenomenon might lead to electrolyte dry-out which would be the reason for the failure mode of a cell. The pronounced HER might be due to: a) an increase in the active surface area of the negative plate; b) the presence of highly active surface functional groups and the presence of certain metal impurities [17,100].

There have been several studies investigating the impact of carbon properties on the HER affinity. Settelein et al. showed [10] that the increase of the external surface area of carbon enhances the HER rate occurring at the negative electrodes. In case of studies focusing on the surface functional groups, inconsistent results were reported about the HER inhibition or acceleration [24,101,102] and this observation might be attributed to the presence of different types of nitrogen groups in the carbon lattice [17]. This topic is further described in chapter 2.4.2. Regarding the presence of metal impurities on carbon, a study has presented that the significant concentration of iron pronounces the HER remarkably as expected [103].

Another limitation of carbon addition results from the manufacture of the negative paste. The pasted negative plates require defined chemical and physical properties. Therefore, an addition of carbon additives into the negative paste shall be implemented without any significant change in the paste properties. The paste mixture including even small amounts of carbon additive requires additional water in comparison to the paste without extra carbon additive. The structural properties of carbon play an important role in this manner [12]. Carbons having a low specific surface area require smaller amounts of additional water than the ones possessing a high specific surface area [104]. The carbon addition, in the range between 1 and 2 wt. % carbon, can also increase the specific surface area of the negative electrode by an order of magnitude or more [12].

2.4 Carbon materials

As the incorporation of carbon materials in the negative plates influences the electrochemical behavior of lead-acid batteries, it is essential to understand their physical and chemical properties to improve electrochemical performance.

Carbon materials exist in different crystallographic forms, mainly as diamond, graphite and amorphous carbon. These materials have been widely used in various applications such as charcoal as heat source, graphite electrodes for steel production, carbon black for reinforcing the tires and activated carbon for water purification [105]. Recently developed carbons such as carbon nanotubes and fullerenes accelerate the

development of nanotechnology and can be found in different fields of science and engineering [42,65]. The characteristics of the carbon materials according to their structural properties and surface chemistry concerning the applications in energy storage are explained in the following subchapters.

2.4.1 Structural properties

The carbon atom is composed of four valence electrons, which are found in its outermost 2s and 2p orbitals, represented as $2s^2 2p^2$. In case of the formation of a chemical bond with other atoms, the carbon atom can possess three different hybridizations, namely sp, sp^2 and sp^3. Different combination of these hybrid orbitals provides various forms of hydrocarbons including aliphatic and aromatic carbons [42].

The carbon possessing sp^2 hybridization is offered by graphite, in which the carbon atoms are arranged in hexagonal rings that are stacked in parallel. These layers are held together via weak van der Waals bonds. Mostly, the hexagonal crystallographic system which has the ABAB stacking sequence of the carbon layers is present in graphite. Further, the rhombohedral system, having the stacking sequence of ABCABC, exists in the graphite structure but it is less frequently observed compared to the hexagonal one [42,65]. The former graphite provides more thermally stable hexagonal symmetry in comparison to the rhombohedral one. The crystal structure of graphite exhibiting the ABAB stacking sequence and that of amorphous carbon are presented in Figure 13 [42].

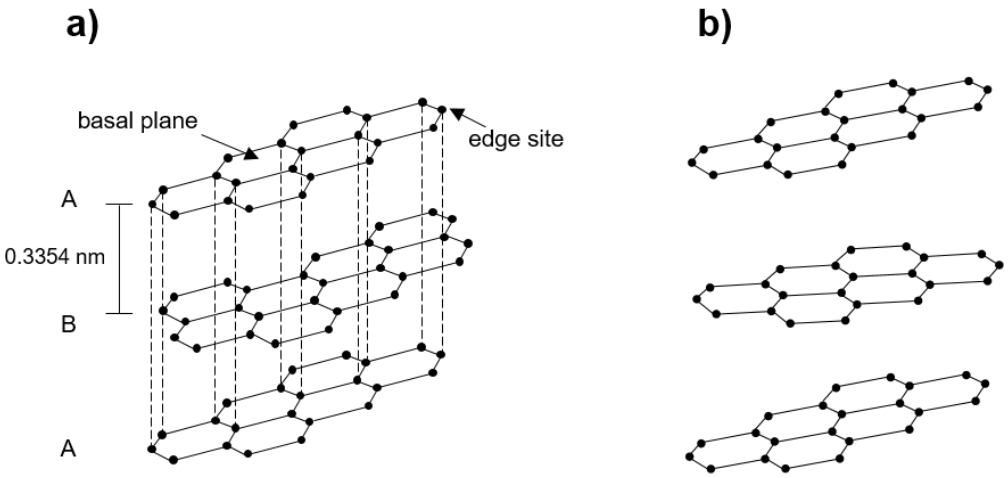

Figure 13: a) The crystal structure of graphite having the ABAB… stacking sequence (hexagonal graphite); b) amorphous carbon (the figure was redrawn based on reference [42]).

Amorphous carbons consist of carbon atoms that are arranged in planar hexagonal networks with a very little crystallographic order in the c-direction. For instance, the layer stacking is generally larger than 0.350 nm for carbon blacks [65]. As seen in Figure 13b,

these carbons have the structure of areas that are embedding and more crosslinking [106]. Generally, nongraphitic carbons are produced by pyrolysis of organic polymer or precursors at temperatures below 1500 °C under an inert atmosphere. These carbons can be either graphitizable (soft) or nongraphitizable (hard) carbons, which are illustrated in Figure 14. The graphite structure can be achieved upon heat treatment of soft carbons above 2000 °C. In case of hard carbons, due to the presence of strong sp^3 crosslinking bonds graphite structure cannot be obtained even at high temperatures (2500 °C - 3000 °C) [107,108].

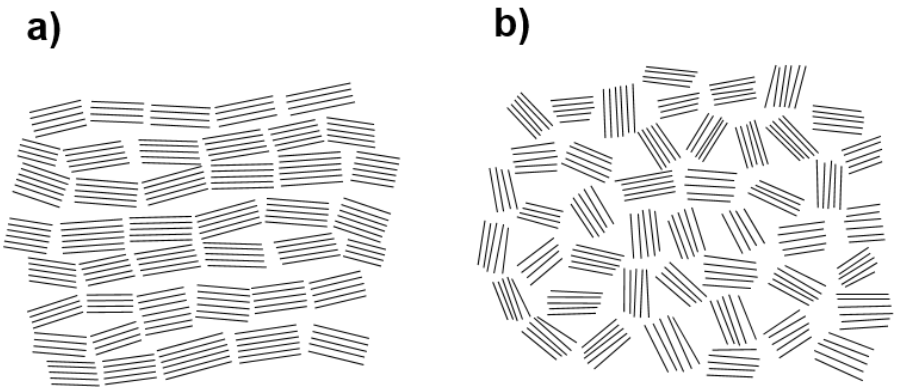

Figure 14: a) The structure model of graphitizable (soft) carbon; b) non-graphitizable (hard) carbon (the figure was redrawn based on reference [109]).

One of the widely used carbon materials in various applications is activated carbon (AC), which consists of a large number of open pores [105]. AC is produced by the thermal decomposition of carbonaceous material followed by chemical or physical activation, which removes the residual material. As a carbon precursor, organic materials containing high carbon content such as coconut shell, wood as well as natural and synthetic polymers can be used [110]. The porosity of AC is obtained during the carbonization process of an organic precursor. The removal of small molecules during carbonization results in distortions within the structure, since hydrogen and oxygen atoms are eliminated. The obtained structure is considered as highly unstable, leading to a combination of carbon atoms with neighbor carbon atoms. The structure of ACs is strongly dependent on the heat treatment temperature. As the treatment temperature increases, the structure reaches more stability. In general, one continuous network of porosity, in which microporosity (0.3 – 2 nm) and mesoporosity (2 – 50 nm) exist, is present in ACs. On the other hand, macroporosity (>50 nm) is regarded as being an open surface [111]. Two parameters which are pore size distribution and specific surface area are often used to determine ACs [105]. The specific surface area of commercially available ACs varies in the range between 500 and 1500 $m^2 g^{-1}$ or even 3000 $m^2 g^{-1}$ [112]. Microporous ACs are often in powdered form, while the granular ones are mesoporous [110]. Due to the excellent adsorptive ability of ACs, they are considered as a potential porous material for CO_2 capture [113]. Furthermore, these materials are often

used in applications such as wastewater treatment [114], catalysis [115] and supercapacitors [116].

Concerning lead-acid batteries, activated carbon [24,85,90,117], carbon black [23,91,118] and graphite [18,90] are used as an additive to the negative plates. Regarding AC, its addition increased the porosity as well as the active surface area of the negative electrode, which is reported to improve the electrolyte diffusion from surface to inner part [85]. Besides structural properties, the surface chemistry of AC is often modified to introduce specific surface groups, which is especially used in supercapacitors [20,22]. This approach is also applied in lead-acid batteries which is further described in the following chapter.

2.4.2 Surface chemistry

The influence of carbon surface chemistry, especially for activated carbons, on the electrochemical activity of electrodes is well known from applications like supercapacitors. Śliwak et al. [20] revealed an improved DL capacitance by using nitrogen-containing activated carbons in supercapacitors, in which the electrolyte was 1 M H_2SO_4. The enhanced performance was attributed to the presence of quaternary nitrogen groups and the low oxygen content. Hulicova-Jurcakova et al. [22] presented the combined effect of nitrogen- and oxygen-containing activated carbon on the performance of supercapacitors with 1 M H_2SO_4. The superior capacitance was associated with the improved electron transfer due to specific nitrogen groups such as quaternary and pyridinic N-oxides. Another study [21] showed also an enhanced capacitance and good rate capability of the electrodes containing functionalized activated carbon nanotubes. The improved capacitive behavior was related to the quinone oxygen, pyridinic and pyrrolic nitrogen of carbon due to its pseudocapacitive contribution.

In terms of lead-acid batteries, the impact of carbon surface chemistry was a focus only in a few studies. DuPasquier et al. [23] presented that the HER on carbon electrodes was increased by using carbon blacks with higher pH. They proposed that the HER during the overcharge of flooded lead batteries might be inhibited by using acidic carbon black additives. Another study [101] investigated activated carbons with acidic and alkaline surface functional groups in LABs. The activated carbon electrodes containing acidic groups exhibited an increased HER activity. This finding was changed after the electrodeposition of lead on these electrodes. In that case, the HER activity was decreased, which was related to the acidic surface groups being the active sites for the electrodeposition of lead. Hong et al. [24] reported the HER inhibition and improved charge acceptance for ultrabatteries by using nitrogen-doped activated carbon. It is known that the incorporation of nitrogen groups in the carbon structure increases the pH

of carbon [25]. Therefore, the studies mentioned above give contradictory results about the impact of carbon surface chemistry on the electrochemical performance of LABs. A comprehensive study on this topic is needed to explain the electrochemical findings. The following paragraphs describe the surface chemistry of carbon materials with a focus on the acidic and basic functional groups.

In general, the surface chemistry of carbon materials is determined by the presence of heteroatoms that exist in the carbon structure such as oxygen, nitrogen, sulfur and phosphorus [25]. The nature and quantity of the functional groups present on the carbon surface are related to the initial synthesis process and/or post-treatments [119]. Surface functional groups as well as the delocalized electrons in the carbon structure establish the acidic or basic character of the carbon materials [120].

Acidic surfaces

The acidic behavior of carbon is mainly associated with oxygen-containing surface groups [121,122]. These groups exist on the outer surface or edge sites of the basal plane of the carbon. Possible oxygen-containing groups include carboxylic, lactone, phenol, carbonyl, pyrone, chromene, quinone and ether groups, which are presented in Figure 15. Most of the surface oxygen-containing groups such as carboxylic, lactone, phenol and lactones contribute to the acidic character of carbons [25,123].

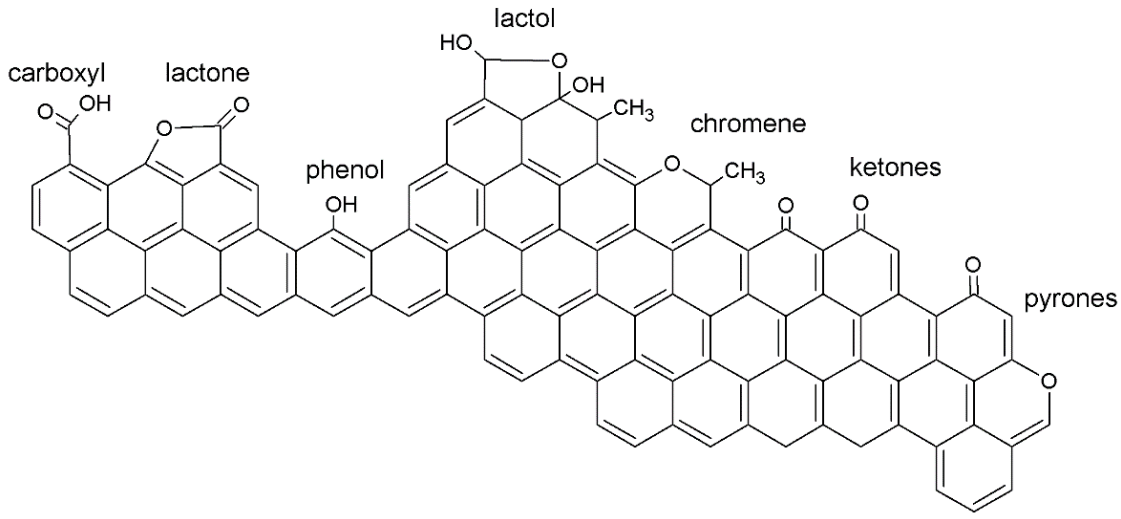

Figure 15: Oxygen-containing groups on a carbon basal plane (the figure was redrawn based on reference [124]).

Oxygen functional groups on the carbon surface can be obtained by treatments with oxidizing agents, either in the liquid phase or in the gas phase [25,119,125]. The liquid phase treatments include nitric acid, hydrogen peroxide, ammonium persulphate and sulfuric acid. On the other side, treatments with air, oxygen, ozone and nitrogen oxides

are considered as the gas phase [121,126–129]. In general, liquid phase treatments enable incorporating higher amounts of surface oxygen groups at much lower temperatures in comparison to the gas phase oxidations [130].

The most commonly used oxidant for carbon modification is concentrated or diluted nitric acid. This method is considered to be an effective way to control the surface properties of carbon via tuning the acid concentration, temperature and treatment time [121,126,127,131]. It has been demonstrated that liquid phase oxidations favor the formation of carboxylic and phenolic hydroxyl groups; whereas, the gas phase treatments mainly introduce phenol and carbonyl groups [119,130,132].

Basic surfaces

The basic character of carbon materials is mainly related to the π electrons in the basal planes of carbon structure and nitrogen-containing groups [124,133,134]. Delocalized π electrons in the basal plane are identified as Lewis-type basic sites [122,124,134]. Further, due to the adsorption ability of protons from solution, oxygen-free carbon sites have also contribution to the surface basicity. These sites can be found in π electron-rich regions on the basal plane [134].

The nitrogen groups include pyridine, pyrrole, pyridone, pyridine N-oxide and quaternary nitrogen. Further possible structures can be also amide and amine groups [135]. The types of nitrogen functional groups are presented in Figure 16. In order to increase the surface basicity, these nitrogen functional groups can be incorporated through either post chemical treatments or activation with nitrogen-containing precursors [136]. Post chemical treatments can be performed with ammonia [137–139], urea [140] and melamine [141]. Modification of carbon materials via ammonia gas at elevated temperatures has been widely used since the amount of surface nitrogen groups can be tuned via change of treatment temperature [142]. Additionally, via ammonia treatment, not only incorporation of nitrogen-containing groups but also the removal of oxygen-containing functionalities are achieved, which can improve the basic character of carbon materials [137,143,144].

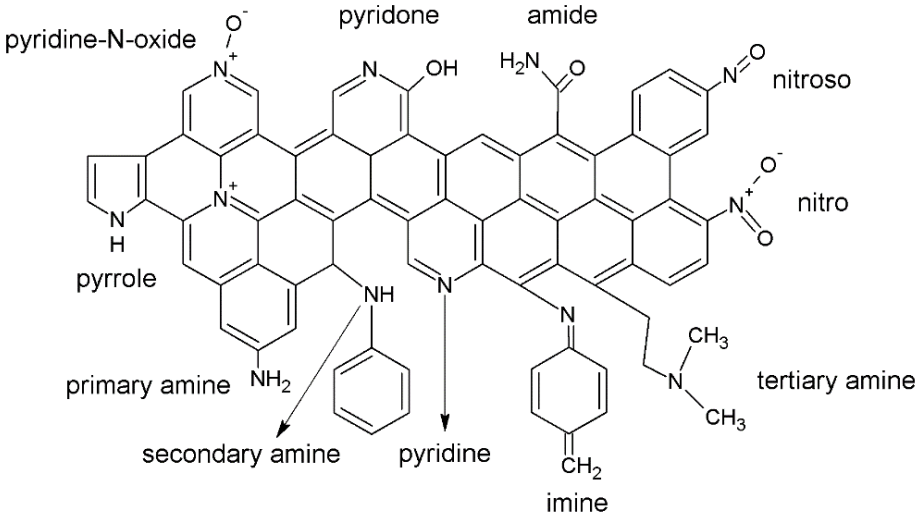

Figure 16: Types of nitrogen-containing functional groups on the carbon surface (the figure was redrawn based on reference [135]).

Heat treatment of carbon materials results in unsaturated surfaces due to the thermal desorption of acidic functional groups [25]. As mentioned above the removal of surface oxygen groups increases the surface basicity. At higher temperatures, strongly acidic groups (carboxylic, anhydrides and lactones) are decomposed, whereas, weakly acidic groups (carbonyl, phenone, quinone) are decomposed at lower temperatures [145,146]. Gas-phase treatment of carbon under N_2 or H_2 gas at elevated temperatures can remove the surface oxygen functionalities, which could increase the surface basicity [147–149]. Hydrogen is considered more effective since it can not only reduce the surface oxygen content and but also deactivate the active sites of carbon leading to a stabilization of the carbon surface [148,150].

In addition to the surface groups mentioned above and π electrons in the basal planes of carbon structure, certain oxygen groups have been proposed to have a contribution to the surface basicity of carbon. These oxygen-containing groups are chromene [151], ketone [152] and pyrrone [153].

3 Part 1: Dynamic charge acceptance tests on laboratory cell-level

The aim of this study is to improve the cell-level measurement methodology for dynamic charge acceptance with respect to active material development and to elucidate the impact of carbon additives on both short- and long-term DCA. For this purpose, a series of carbons providing external surface area ranging from 7 $m^2 g^{-1}$ to 159 $m^2 g^{-1}$ were used as additives in negative electrodes. Therefore, a comparison of different charge acceptance tests in terms of carbon material screening as well as the adaptation of DCA test methodology in 2 V cell-level can be investigated.

This chapter is divided into two main parts. Firstly, the preparation conditions and characterization techniques of carbon additives and the negative electrodes are described in the experimental part. The part also includes the characteristics of the applied laboratory cells as well as the respective electrical and electrochemical tests. Secondly, the characterization results obtained from the nitrogen sorption, scanning electron microscopy, and x-ray diffraction are overviewed and discussed. The part also focuses on the results of the different charge acceptance tests in terms of the carbon additive´s effect. Further, the relationship between dynamic charge acceptance and electrochemical activity of cells, obtained from cyclic voltammetry and electrochemical impedance spectroscopy, are presented and discussed. Afterwards, the chapter concludes with a summary. Part of the results obtained from this chapter was published in *Energy Technology* in January 2022 [154].

3.1 Experimental

The following chapters explain the experimental procedure used for the production and characterization of the carbon materials and negative electrodes. Moreover, the properties of laboratory cells as well as the executed electrical and electrochemical tests are outlined.

3.1.1 Preparation of spherical porous carbons

Similar to the published work [10,72], a new batch of five different amorphous carbon powders each with a specially adjusted particle size were provided by the Bavarian Center for Applied Energy Research (ZAE Bayern), the research group of Nanomaterials located in Würzburg. The spherical carbons possessing different particle sizes were synthesized via a sol-gel process in which the reactants of resorcinol and formaldehyde were used. The concentration of the reactants in the organic aqueous solution was kept below 20 % to lower the gel network formation. The particle sizes of the carbons were altered by varying the molar ratio of resorcinol to the catalyst (0.1 mol l^{-1} Na_2CO_3) from

700 to 3000. Then, the obtained solution was aged for 24 h at 85 °C. Afterwards, the particles were extracted from the dispersions by convective drying of the solutions over several days. Lastly, the obtained organic powder was pyrolyzed at 800 °C under an argon atmosphere. Further details regarding the synthesis procedure can be found in the literature [155]. Due to adjusted particle size, these spherical carbon particles exhibit different specific external surface areas. These five different carbons were named C1, C2, C3, C4, and C5 which are in the order of an increase of external surface area.

3.1.2 Preparation of negative electrodes and laboratory cells

Negative electrodes

The negative pastes composed of spherical porous carbon additives were prepared. The negative pastes consisted of 100 wt. % leady oxide (from ball mill process) as an active material, 13 wt. % distilled water, 8 wt. % diluted sulfuric acid (50 wt. %, diluted from concentrated sulfuric acid, ACS grade, Sigma Aldrich), 0.8 wt. % barium sulfate (Merck) as a nucleation agent, 0.2 wt. % sodium lignosulfonate (Vanisperse A, Borregaards Lignotech) and 2 wt. % carbon additive. The given concentrations are concerning the amount of leady oxide and its content is considered as 100 wt. %. The mixing of the paste components was done by using a speed mixer (Hauschild Germany, DAC 400.1) for a total of 15 min. During mixing, the paste temperature was kept below 65 °C. Directly after mixing, the negative grids (Pb-Ca-Sn alloy) were manually pasted with (17 ± 1) g paste. The negative grids have a dimension of 43×68×2 mm^3. Afterwards, the negative plates were cured at 45 °C in the oven in two steps. In the first step, the curing was performed for 15 h at a relative humidity of 99 %. In the second step, the relative humidity was decreased slowly to around 10 % and the negative plates were dried for 7 h. A picture of cured negative plates is shown in Figure 17.

Figure 17: Manually pasted negative plates containing carbon additives after curing procedure.

Laboratory cells

After the the preparation of negative plates, 2 V laboratory test cells were assembled. The laboratory cells consist of one negative plate, two positive plates, and a reversible hydrogen electrode (RHE, Hydroflex®, Gaskatel Germany) as a reference electrode. The positive plates are enveloped by polyethylene separators (Daramic® HP™, Daramic LLC). This asymmetric design of two positive electrodes and one negative electrode (2P1N) was chosen to limit all cell properties, such as capacity and charge acceptance, by the negative electrode. The test cells provide a 20 h discharge capacity of around 2.5 Ah. Figure 18 shows a picture of a laboratory cell as well as the plate stacking order inside the cell used in this study.

The container formation method was used to form the cured negative and positive plates. Therefore, the laboratory cells were filled with sulfuric acid with a density of 1.15 g ml^{-1}. The formation procedure consists of six different constant current steps. In the first five steps, cells are charged respectively with constant currents (CC) of $0.4 \cdot I_{20}$, $0.8 \cdot I_{20}$, $1.2 \cdot I_{20}$, and $1.6 \cdot I_{20}$ for 30 min each. The last steps include a CC charging with $2 \cdot I_{20}$ was applied for 34 h. The current I_{20} is calculated considering an empirical C_{20} capacity of 0.14 Ah g^{-1} regarding the weight of the cured NAM.

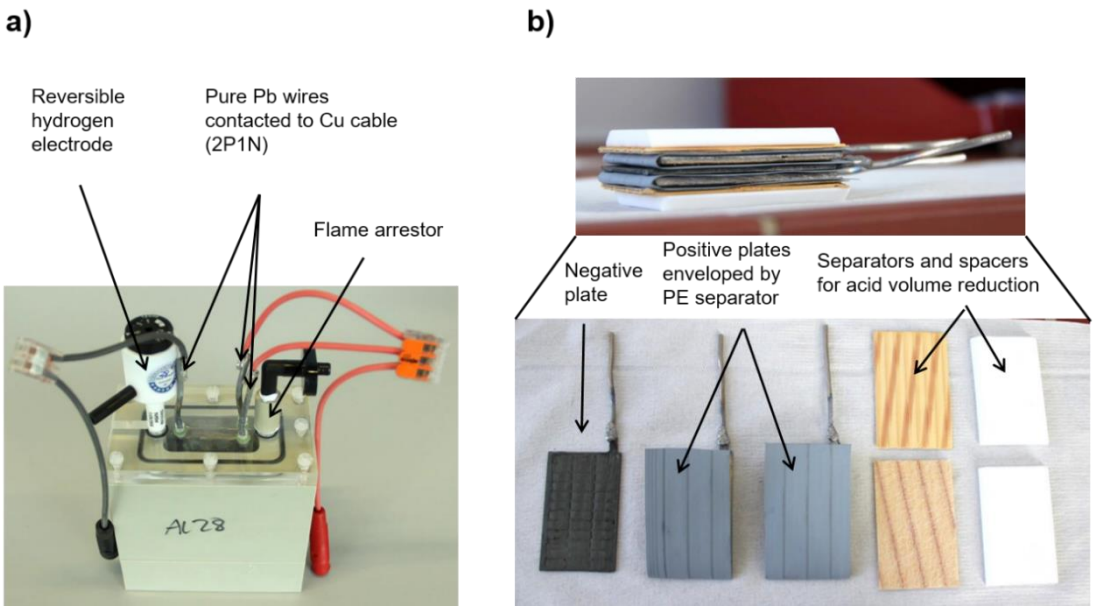

Figure 18: a) 2 V, 2.5 Ah laboratory cell consisting of two positive plates, one negative plate, a reference electrode and a flame arrestor; b) Plate stacking inside the cells showing one negative plate surrounded by wrapped positive plates, separators and spacers used to reduce the acid volume.

3.1.3 Characterization of carbon powders and negative electrodes

Nitrogen sorption

The textural properties of these five-carbon materials were determined by nitrogen sorption at 77 K using a volumetric adsorption instrument (ASAP2020, Micromeritics). The nitrogen sorption measurements were performed at ZAE Bayern. Prior to measurements, carbon powders were degassed at 300 °C for 12 h. The BET (Brunauer, Emmett and Teller) theory [156] was applied to determine the specific surface area (S_{BET}). The t-plot method was used to calculate the specific external surface area (S_{ext}), i.e. the envelope surface area of the microporous carbons, and the specific micropore volume (V_{mic}). For the determination of the average particle diameter (d_{part}), carbon particles are assumed to be spherical. The d_{part} is calculated by the ratio of the spherical surface ($S_{spherical}$) to the spherical volume ($V_{spherical}$) which is equal to the sum of V_{mic} and the volume of the non-porous carbon skeleton (V_C) divided by the S_{ext}.

$$\frac{V_{spherical}}{S_{spherical}} = \left(\frac{V_{mic} + V_C}{S_{ext}}\right) \tag{29}$$

where $V_{spherical} = 4/3\ \pi r^3$ and $S_{spherical} = 4\ \pi r^2$.

Based on the results obtained from the t-plot method and considering the density of the nonporous carbon as $\rho_c = 2.06$ g cm^{-3}, the average particle diameter (d_{part}) was estimated according to the formula below

$$d = \frac{6}{S_{ext}} \cdot \left(V_{mic} + \frac{1}{\rho_c}\right) \tag{30}$$

where the ρ_c is taken as 2.06 g cm^{-3} [157].

In case of the negative electrodes, the nitrogen sorption measurements were executed with Autosorb 3B Quantaschrome. Prior to analysis, the negative electrodes were outgassed at 150 °C for 24 h.

Scanning electron microscopy

Carbon powders and cured as well as cycled negative electrodes were analyzed by using scanning electron microscopy (SEM) to determine their morphological properties. SEM analysis for all samples was carried out with a Zeiss Supra™ SEM using the inlens and secondary ion detector. The carbon powders and cured negative plates were used as it is for the sample preparation for SEM analysis. In case of the cycled negative plates, directly after disassembly of test cells, the negative electrodes were washed with deionized water several times until the pH of the active mass was above 6. Then, the

electrodes were washed with ethanol for 2 min. This washing procedure was applied separately for each negative plate. Directly after washing, the negative plates were dried overnight at 60 °C under vacuum.

X-ray diffraction

The crystal structure of the cured negative electrodes was analyzed via X-ray diffraction (XRD) using PANalytical Empyrean diffractometer equipped with the Bragg-Brentano geometry. The measurements were executed with Cu K_α radiation between 15 ° and 80 ° 2θ with a step size of 0.0066 ° and a scan duration per step of 250 s. The fixed incidence angle of the radiation was 0.5 ° and the mask was 10 mm.

It is worth mentioning that all characterization methods described above were conducted once after the optimization of the respective method. Thus, the corresponding results shown later belong a single measurement.

3.1.4 Electrical and electrochemical testing of laboratory cells

Three different tests were applied on laboratory cells in order to determine the dynamic charge acceptance as well as to compare these tests on cell-level. These charge acceptance tests include both short-term and long-term tests. In case of short-term testing, charge acceptance (CA) test 2 according to SBA S0101:2014 [158] and DCA test from EN 50342-6:2015 specification [5] were executed. Regarding long-term testing, the Run-in DCA test (Test B) developed by Ford was employed. In addition to these charge acceptance tests, electrochemical impedance spectroscopy was performed on test cells as a side study to investigate the electrochemical properties of negative electrodes. The detailed procedure of these mentioned tests is described in the following paragraphs.

Sequence of electrical and electrochemical tests

The sequence of the electrical and electrochemical tests applied in this study is listed in Table 1. After the container formation of the negative and positive electrodes, the cells were subjected to the CA test 2 according to the SBA standard. The DCA test is divided into three different parts which are later on explained in the DCA test description. Firstly, the pre-cycling part of the DCA test was applied. Then, the cyclic voltammetry test was carried out at 100 % SoC to evaluate the electrochemical activity of lead-carbon electrodes. After the CV test, the cells were subjected to the qDCA part of the DCA test. After one day rest period, the EIS measurements were carried out at 80 % SoC on the cells. Then, the DCRss part of the DCA test was applied at 80 % SoC. After the completion of the whole DCA test, the 3 weeks of the Run-in DCA test was executed on the cells. After 3 weeks of Run-in cycling, the cells were rested for 31 days which is known as “airport parking” in the Run-in DCA test. Later on, the cells were further tested

with the 4 weeks of the Run-in DCA test. Furthermore, after the completion of the Run-in DCA test, 3 cells based on their performance (poor, moderate, good DCA) were chosen. These cells (C2, C3 and C4) were rested for 4 months, in which the resistors were disconnected from the cell terminals. Then, the cells were subjected to the pre-cycling test followed by 4 weeks of the Run-in test.

It should be mentioned that the reason for conducting the CV measurements after the pre-cycling part is to determine the discharge capacity of cells for validation of the cell setup (e.g. capacity limitation by negative electrode). However, the SBA test was still executed before the pre-cycling part due to the sensitivity of the SBA test on the history of cells.

Table 1: Electrical test sequence of the laboratory cells

Electrical tests	# of cells
Formation	5
CA test 2 (SBA)	5
Pre-cycling part of the DCA test (EN)	5
Cyclic voltammetry	5
qDCA part of the DCA test (EN)	5
Electrochemical impedance spectroscopy	5
DCRss part of the DCA test (EN)	5
3 weeks of Run-in DCA test (Ford)	5
31 days of airport parking	5
4 weeks of Run-in DCA test (Ford)	5
4 weeks of parking and pre-cycling test	3
4 weeks of Run-in DCA test (Ford)	3

In a first approach, the charge acceptance tests were applied with a two-wire connection. As it was found that the two-wire connection reduces the total charge currents compared to a four-wire connection due to a significantly increased internal resistance. Especially, the long-term Run-in DCA test was falsified by that. Therefore, it was decided to repeat all tests with a four-wire connection. In this thesis, only the results obtained from the four-point measurement are shown. For both cells with two- and four-wire connections, freshly formed cells were used and tested according to the test sequence described in Table 1. The electrochemical tests, which are CV and EIS, were executed with a four-point technique. It should be mentioned that these two test methods were applied on the cells which were subjected to charge acceptance tests with a two-point technique. These tests were not repeated for the cells tested via charge acceptance tests with a four-point technique since the history of the cells are the same and therefore the characteristics of

the obtained results are not expected to differ. In total, three laboratory cells per negative paste variant (15 cells) were tested for each electrical and electrochemical test. However, only the results of one cell per each paste variant (5 cells) are shown in this thesis since there was an error in the algorithm of the test program for the DCRss part of the DCA (EN) test for the remaining 10 cells. Even though the DCA results of 10 cells were similar to the 5 cells, those results were neglected for quantitative comparison.

Charge acceptance test 2 (SBA S0101:2014)

In the charge acceptance test 2 according to the SBA standard, fully charged laboratory cells are first discharged with $3.42 \cdot I_{20}$ for 30 min. Then, the cells are kept in a rest period of 16 h. Afterwards, a constant voltage of 2.42 V is employed for 10 s, in which the charging current is recorded. The average current determined from this 10 s charging pulse gives the charge acceptance of the cell.

Dynamic charge acceptance test (EN 50342-6:2015)

The DCA test is composed of three main parts which are the pre-cycling, the quick DCA (qDCA) test, and the dynamic charge acceptance real world stop/start driving cycle DCRss. The precycling part of the DCA includes two reserve capacity (RC) tests and one C_{20} discharge. After the completion of C_{20} capacity determination, the cells are recharged to only 80 % SoC. In the qDCA part, the pulse charge acceptance after charge operation at 80 % SoC and after discharge operation at 90 % SoC is determined. In both conditions, 20 microcycles with charging steps at a constant voltage of 2.47 V for 10 s are executed, and the average charge current obtained from these charge pulses is calculated. The average charge current determined after charge and discharge history are represented as I_c and I_d, respectively. In the last part of the DCA test, the DCRss part, an average charge acceptance at 80 % SoC is calculated during a one-week simulated Start-Stop drive cycle including regenerative braking. In order to simulate key-off loads, a resistor is connected across the cell terminals, which discharges the cell by around 0.8 % of C_{20}. In this test, the target of 80 % SoC is controlled via ampere-hour balancing. The average charge current, I_r, is measured from all regenerative charge pulses applied at a constant voltage of 2.5 V for 5 s. According to the average charge currents obtained from qDCA and DCRss parts, the normalized dynamic charge acceptance, I_{DCA}, of laboratory cells is calculated from the formula shown below [5].

$$I_{DCA}\left[\frac{A}{Ah}\right] = (0.512 \cdot \frac{I_c}{C_n}) + (0.223 \cdot \frac{I_d}{C_n}) + (0.218 \cdot \frac{I_r}{C_n}) - 0.181 \qquad (31)$$

Run-in DCA test (Ford, test B)

In this long-term test, a real-world usage profile in micro-hybrid vehicles is simulated, which differentiates this test from accelerated laboratory tests. The purpose of conducting the Run-in test is to investigate the Run-in effect, known as a DCA decline over several weeks of cycling, could be also revealed in 2 V laboratory cells or not.

The DCRss part of the DCA (EN) test includes the same weekly driving profile as the Run-in DCA test. The latter simulates the long-term customer usage profile. The Run-in DCA test was started after the end of DCRss (EN) test and the same key-off load (KOL) resistors were still connected to the battery terminals. Especially during rest periods (night, weekend and airport parking), KOLs were simulated by the resistors, which discharge the battery by 25 % SoC within 31 days.

The DCRss (EN) part represents the first week of the drive cycle. This is continued by the Run-in DCA test which takes another 3 weeks of modified DCRss test, followed by 31 days of airport parking break and another 4 weeks of modified DCRss test. The essential difference between the DCRss (EN) test and the Run-in test (modified DCRss) is the continuous SoC adjustment to keep 80 % SoC. In case of the DCRss (EN) part, the SoC is adjusted only by charge balancing, so-called Ah-balancing. That means, discharge events and charge drain via the KOL resistor are counted and compensated by recharge events. As the Run-in DCA test takes several weeks, only Ah-balancing would be insufficient since side-reactions and self-discharge are not compensated. Based on that, the following points explain the difference between these two tests.

- In the Run-in test, two-third of the Ah balance is controlled by quasi-open circuit potential (OCV) measurements every morning. The values obtained from this correction are called AhOCV. This OCV correction is neglected in the DCRss (EN) test.
- In the Run-in test, only one-third of the Ah drain by KOL resistor is compensated. The value obtained from this correction is called AhKOL. This reduced KOL correction enables having the quasi-OCV corrections if the actual OCV is below the targeted OCV value at 80 % SoC, which is defined in the test procedure as OCV80. On the other hand, if the actual OCV value is equal to or bigger than the OCV80 value, OCV correction does not take place and therefore it does not influence the Ah balance. In case of the DCRss (EN) test, Ah balance is completely covered by the AhKOL correction.

In the Run-in test, the following parameters were adjusted for the laboratory cells. In case of 12 V batteries, the dV value is generally between 10 mV and 15 mV which strongly depends on the battery technology. For 2 V cells, the dV value shall be normally divided by six. Due to different acid to active mass ratio in small laboratory cells, the change of

1 % SoC generates much lower dV. Taking this situation into consideration, a dV value of 1 mV was used. Moreover, based on the OCV values of the cells at the end of DCRss test (EN), the OCV80 was set as 2.105 V for all cells.

Cyclic voltammetry

After the pre-cycling part of the DCA test, the cyclic voltammetry measurements were performed at 100 % SoC to determine the double-layer capacitance and the hydrogen evolution reaction activity of the negative electrodes. The CV measurements were carried out on a Scienlab battery tester (Keysight, Germany). The fully-charged negative electrodes were cycled between the potential of $Pb/PbSO_4$ redox couple reaction at -0.35 V vs. RHE and -0.9 V vs. RHE. In case of the DL region, the negative electrodes were cycled between -0.5 V vs. RHE and -0.7 V vs. RHE. For both CVs, a scan rate of 10 mV s^{-1} was used.

Electrochemical impedance spectroscopy

Electrochemical impedance spectroscopy was performed on the cells after the end of the qDCA part of the DCA test. EIS measurement was applied to characterize non-linear processes as well as the dynamics of electrochemical processes. EIS measurements were applied by using Biologic VMP-300 Potentiostat. Electrochemical impedance spectrum was obtained by the galvanostatic method in which the sinusoidal current (I_{ac}) with a defined frequency (f) is applied and the voltage response (V_{ac}) is measured. In this work, the EIS spectra were recorded in a frequency range between 10 mHz and 6.5 kHz. The impedance resulting from the current and voltage signal is calculated according to the formula below.

$$Z\,(f,\, I_{dc}) = \frac{V_{ac}}{I_{ac}} \tag{32}$$

Besides the frequency of the input signal, the superimposed charge and discharge current influence the obtained impedance as well. A variation in polarity during the measurement can be prevented by using the superimposed charge and discharge current. This can ensure that all parts of the electrodes are involved in the electrochemical reactions. A superimposed current of $0.5 \cdot I_{20}$ was chosen.

The executed program of the EIS is shown in Figure 19. Each dc charge and discharge steps were applied with a constant current of $0.5 \cdot I_{20}$. The galvanostatic EIS (GEIS) measurements were performed with a current modulation of 44 mA (80 % of $0.5 \cdot I_{20}$) and a spectral density of 10 points per decade. The program was started when the cells were at 80 % SoC. Firstly, the cells were kept at 80 % SoC for one hour to record the open circuit potential. Afterwards, the cells were charged until 82 % SoC is reached. Then, the cells were discharged to 81 % SoC, and the GEIS measurements were started while the

cell was discharging with a dc current. The GEIS measurements were continued until the cell reaches 79 % SoC and then the cell was further discharged to 78 % SoC. The same procedure as well as the GEIS measurements were performed during charging. Finally, the GEIS during the discharge and charge process was repeated once more. In this test, the target SoC value was always controlled by either charging or discharging the cell with a constant current and a defined time.

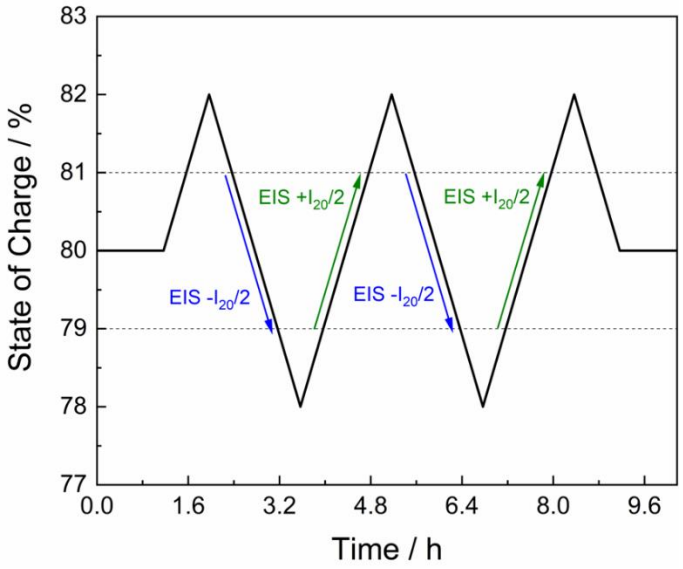

Figure 19: The program of EIS measurements executed on laboratory cells.

For data evaluation, the second GEIS measurement during the charge process was taken into account to compare the electrochemical state of the cell with the DCA.

3.2 Results and Discussion

This chapter covers the results of cell-level measurement methodology for DCA and gives a comparison of different charge acceptance tests regarding carbon material screening. Moreover, results obtained from electrochemical test methods such as cyclic voltammetry and electrochemical impedance spectroscopy are explained and discussed.

3.2.1 Properties of spherical porous carbons

3.2.1.1 Textural properties

The textural properties of the five different spherical porous carbons determined by N_2 sorption measurements are presented in Table 2. All carbon materials provide comparable BET surface area (S_{BET}) in the range between 686 $m^2\ g^{-1}$ and 718 $m^2\ g^{-1}$. A slight increase of S_{BET} in response to the decrease of particle size of carbons might be attributed to the increased outer surface and additional pores for smaller particles. It is assumed that the sum of the micropore surface area and the specific external surface

area form the total S_{BET}. An almost identical microporosity of all five carbons is observed due to the same carbon precursor and pyrolysis procedure for all five carbons. All carbons possess similar specific micropore volume (V_{mic}) in the range between 0.226 $cm^3\ g^{-1}$ and 0.262 $cm^3\ g^{-1}$. A slight decrease of V_{mic} with respect to the decrease of particle size can be explained by the reduction in specific weight fractions for smaller particles. The specific external surface area (S_{ext}), generated by the inner-particle pores and the envelope surface area of the particles, increases from C1 to C5. This increase can be attributed to the decrease in the average particle size (d_{part}). By variation of the d_{part} between 27 nm and 633 nm, the S_{ext} of the carbons is altered between 7.1 $m^2\ g^{-1}$ and 159.3 $m^2\ g^{-1}$. The textural properties of carbons obtained from the N_2 sorption measurements are in line with the published study [10], where spherical carbons synthesized by a similar procedure were used.

Table 2: Textural properties of the spherical porous carbons obtained from the N_2 sorption measurements (the table was reproduced from Bozkaya et al. [154])

Material	S_{BET} ($m^2\ g^{-1}$)	S_{ext} ($m^2\ g^{-1}$)	V_{mic} ($cm^3\ g^{-1}$)	d_{part} (nm)
C1	685.9	7.1	0.262	633
C2	699.1	20.3	0.262	221
C3	706.5	50.4	0.254	88
C4	713.3	92.1	0.244	48
C5	717.6	159.3	0.226	27

3.2.1.2 Morphological properties

The morphology of the carbon samples was analyzed via SEM. The obtained SEM micrographs are illustrated in Figure 20. As expected, the mean particle size of the carbons varies significantly. From C1 to C5, a reduction in the sizes of the carbon particles can be seen. In case of the carbons with larger particle sizes (C1 and C2), broader particle size distribution is observed. This phenomenon cannot be prevented due to the manufacturing process and is resulted from the continuous growth of the particles. As shown in the electrical test results (chapter 3.2.3) and also explained in [10], the remarkable difference between the mean particle size of these five different carbons is sufficient to evaluate and differentiate the electrochemical performance of the lead-carbon electrodes. The influence of the particle size distribution on the electrochemical properties can be considered negligible.

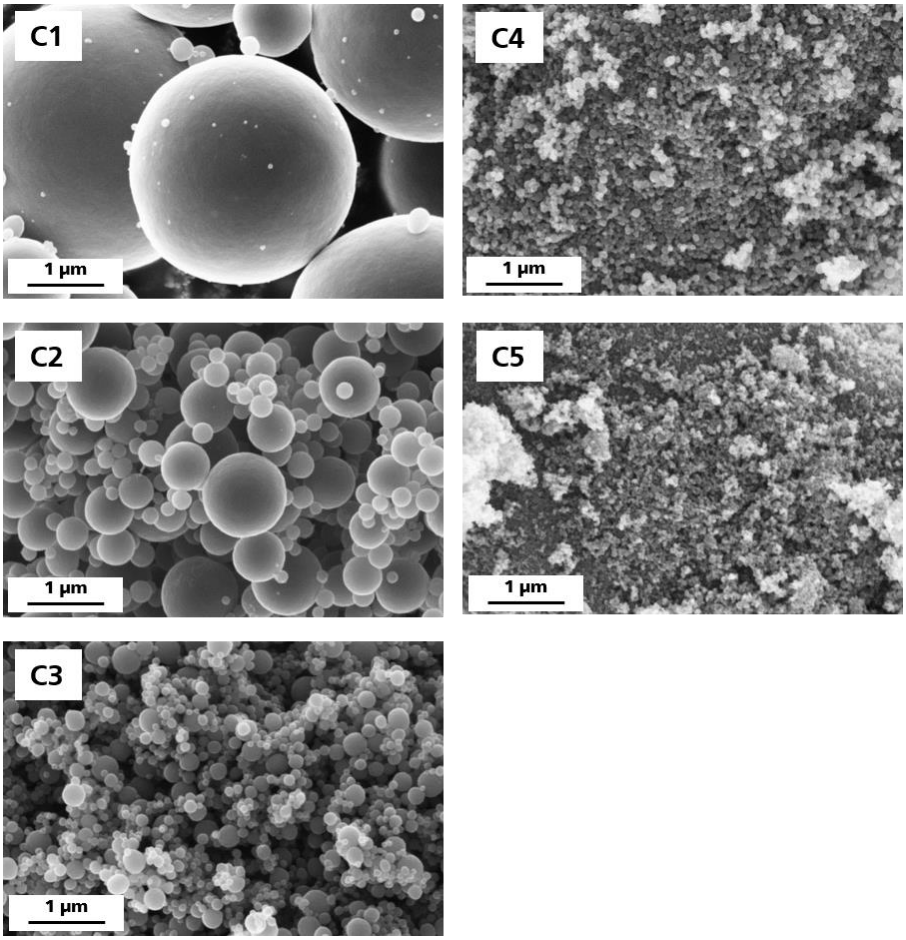

Figure 20: The SEM micrographs of the five different spherical porous carbons used as additives in the negative electrodes.

3.2.2 Properties of lead-carbon electrodes

To elucidate the influence of the carbon additives on the structural and chemical properties of the lead-carbon electrodes, the amount of the carbon additive as well as the water and lignosulfonate content was kept identical in the paste mixture of the negative electrodes. All negative electrodes consist of 2 wt. % carbon additive. Therefore, differences in the surface characteristics of the negative electrodes shall be originated from the carbon type. The following paragraphs explain and discuss the characterization results of the cured negative electrodes.

3.2.2.1 Textural properties

The specific and external surface area of the lead-carbon electrodes obtained from the N_2 sorption measurements are shown in Table 3. The S_{BET} of electrodes is obtained between 6.7 $m^2\ g^{-1}$ and 11 $m^2\ g^{-1}$. There is a tendency that carbons with larger particle sizes possess much higher S_{BET}. As the lead structure is known to have no microporosity,

all micropores in the negative electrode are attributed to the carbon additive. Interestingly, the S_{BET}, which is similar for all carbon types, varies significantly for the lead-carbon electrodes. It is assumed that the micropores are partially blocked. This blocking seems to be more dominant for smaller carbon particles since the S_{BET} becomes much lower. The micropores of negative electrodes containing bigger carbon particles might be maintained more due to a higher volume-to-surface ratio. Thus, it is more likely that outer parts of the carbon micropores might be partially blocked by the other paste components such as lignosulfonate and/or lead oxide during mixing and curing steps. For the case of S_{ext}, the negative electrodes exhibit values between 3 $m^2\ g^{-1}$ and 5.6 $m^2\ g^{-1}$.

Table 3: Textural properties of the lead-carbon electrodes obtained from the N_2 sorption measurements (the table was reproduced from Bozkaya et al. [154])

Electrode	S_{BET} ($m^2\ g^{-1}$)	S_{ext} ($m^2\ g^{-1}$)
C1	11.0	3.6
C2	10.9	3.0
C3	10.2	3.9
C4	6.9	4.4
C5	6.7	5.6

To understand the relationship between the external surface area of carbons and that of lead-carbon electrodes, the values obtained from the N_2 sorption measurements are plotted in Figure 21. Almost a linear correlation between the external surface area of carbons and lead-carbon electrodes can be established. This observation can be attributed to the assumption that the S_{ext} of the negative electrode is mainly generated by the specific surface area of lead oxide and the external surface area of carbon. Based on this assumption, the external surface area of negative electrodes can be estimated according to the equation given below.

$$S_{ext}\,(\text{electrode}) = [0.98 \cdot S\,(\text{lead oxide})] + [0.02 \cdot S_{ext}\,(\text{carbon})] \qquad (33)$$

The coefficients in the equation 33 correspond to a negative electrode comprised of 98 wt. % lead oxide and 2 wt. % carbon additive. As seen in Figure 21, the slope of the linear fit is 0.02, which matches with the equation 33. Therefore, it can be said that the negative electrodes containing carbon additives with higher S_{ext} tend to provide greater S_{ext} as well.

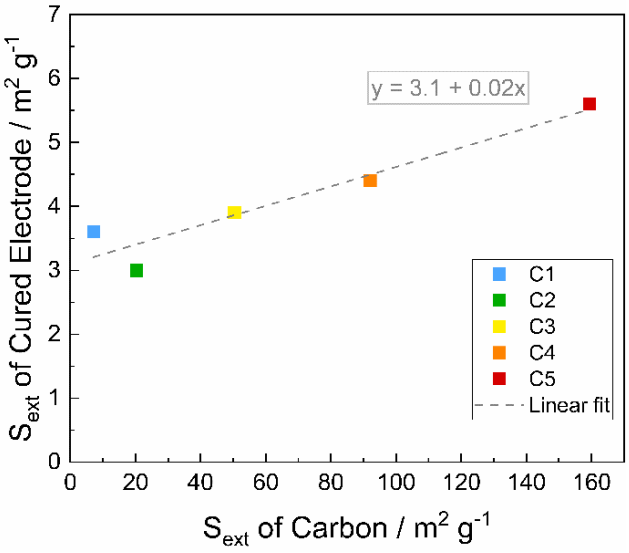

Figure 21: Relationship between specific external surface area of carbons and that of the cured negative electrodes (the figure was reproduced from Bozkaya et al. [154]).

3.2.2.2 Morphological properties

To elucidate the influence of the carbon structure on the morphological properties of the lead-carbon electrodes, the morphology of the negative electrodes was analyzed via SEM. The corresponding micrographs of the five different lead-carbon electrodes at different magnifications are shown in Figure 22. The SEM pictures at low and high magnifications are presented on the left and right sides of the Figure 22, respectively. The SEM micrographs show particles with lighter color which represents lead oxide and tribasic lead sulfate (3BS) formed during the curing process of the negative electrodes [2]. In all micrographs, the carbon particles can be observed as spherical particles, which generally appear darker than the surrounding lead structure. Carbons with bigger particle sizes (C1 and C2) are well distributed in the lead skeleton. In the case of electrodes containing carbons with smaller particle sizes (C3, C4 and C5), the carbon particles are mainly found as agglomerates of up to 5 µm. This agglomeration might change the electrochemical activity of such electrodes and might influence the adsorption of lignosulfonate to the carbon as well.

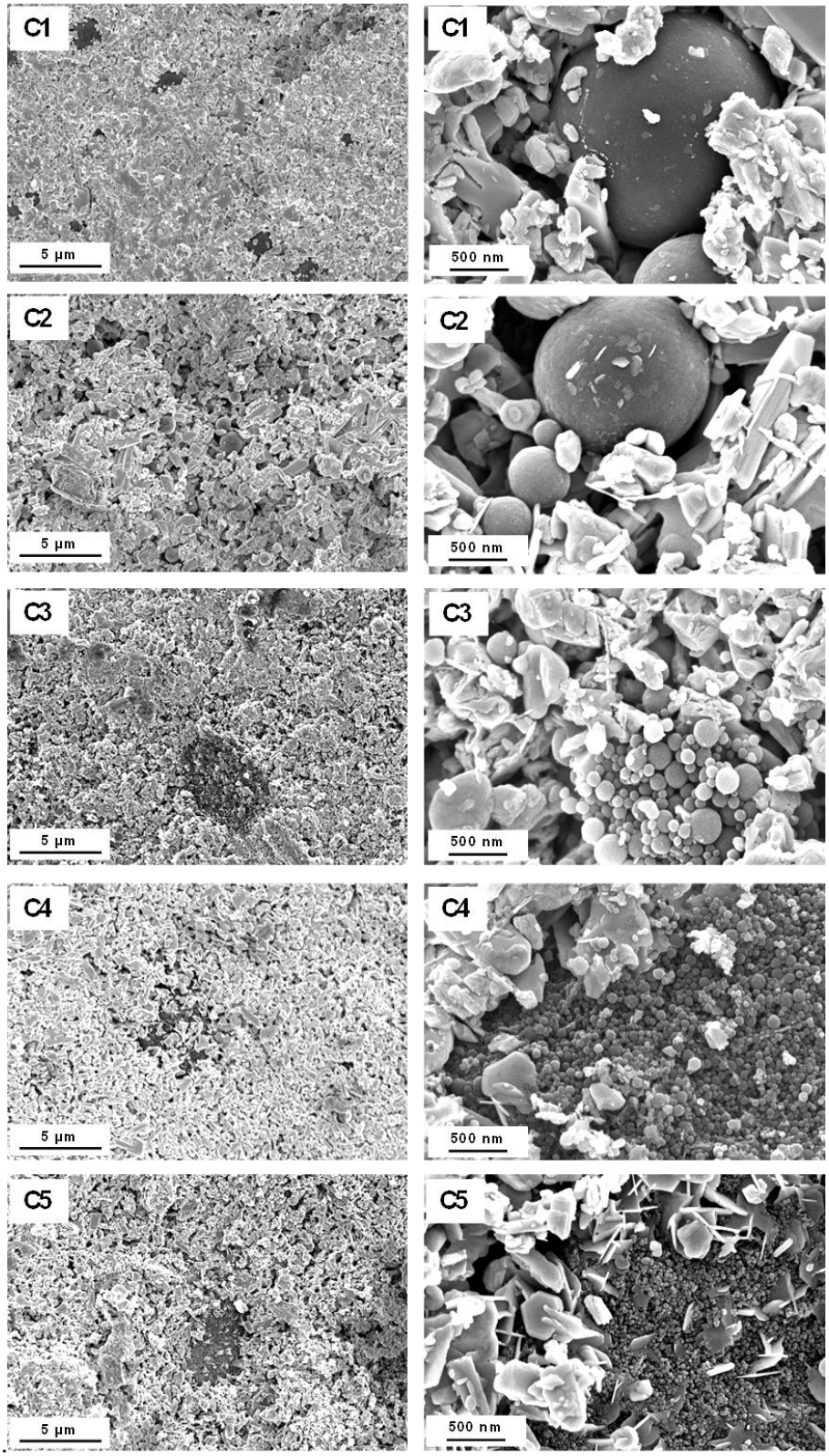

Figure 22: SEM micrographs of the cured lead-carbon electrodes containing C1, C2, C3, C4 and C5 additives (the figure was reproduced from Bozkaya et al. [154]).

3.2.2.3 Crystal structure

Since the amount of paste components as well as the mixing and curing steps were identical for all electrodes, the crystal structure of the negative electrodes is expected to be very similar. Still, to reveal if there are any differences in the crystal phases of the cured lead-carbon electrodes resulting from using different carbon additives, the XRD measurements were carried out. Figure 23 shows the XRD spectra of the cured negative electrodes with C1, C2, C3, C4 and C5 additives. The XRD patterns of all electrodes are almost identical. The crystalline phases of lead, 3BS, litharge and hydrocerussite are detected for all electrodes. The litharge and hydrocerussite correspond to PbO *alpha* and $2PbCO_3 \cdot Pb(OH)_2$, respectively. The latter is formed due to the reaction between CO_3^{2-} ions and $Pb(OH)_2$. These ions are present due to the oxidation of Ca, coming from the grid alloy, and its reaction with CO_2 forming $CaCO_3$ [2].

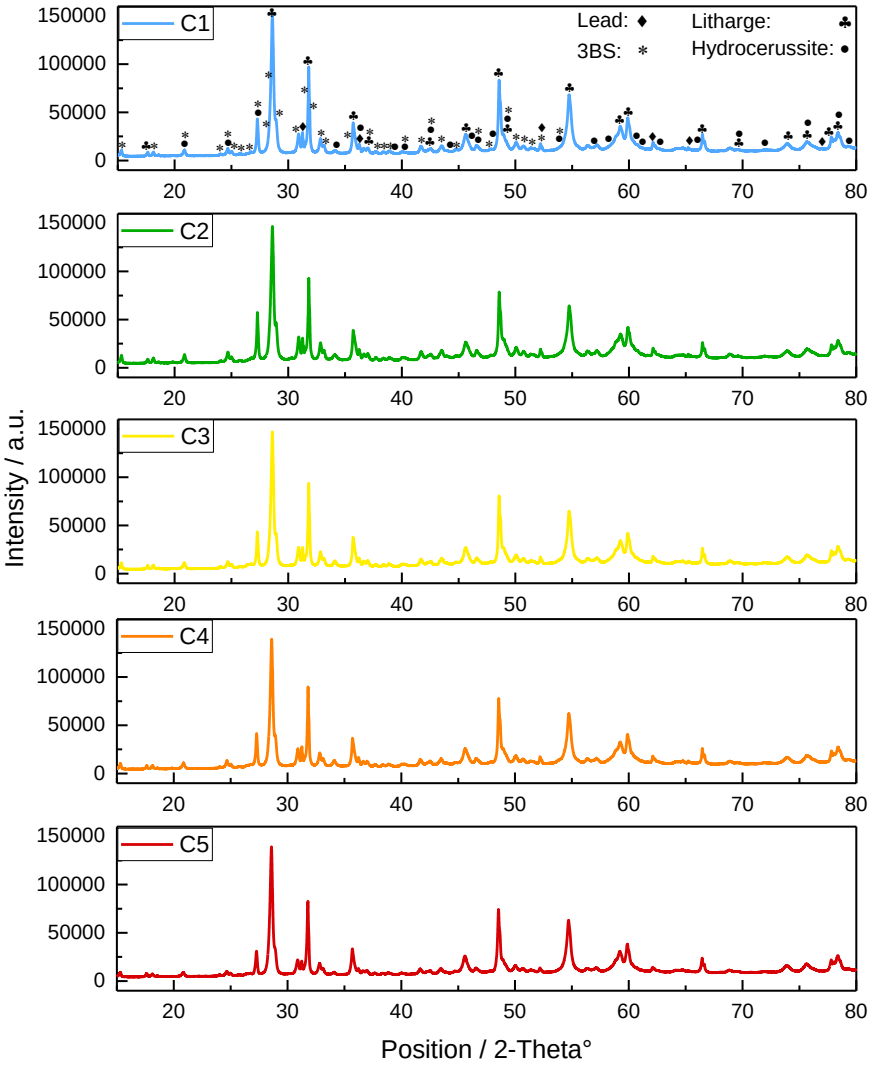

Figure 23: The XRD pattern of the cured lead-carbon (negative) electrodes containing C1, C2, C3, C4 and C5 additives.

The phase composition of the cured negative electrodes is presented in Figure 24. Mainly crystalline phases of PbO and 3BS are detected for all electrodes. There is only a slight tendency that the electrodes containing carbon additives with greater S_{ext} have a higher composition of PbO and a lower composition of 3BS. The only exception is obtained for the C1 electrode. Furthermore, all electrodes contain a very small amount of lead and hydrocerussite, which is between 1% and 3%.

As a result of the XRD measurements, no clear influence of carbon additives on the diffraction patterns as well as the crystalline phases can be revealed.

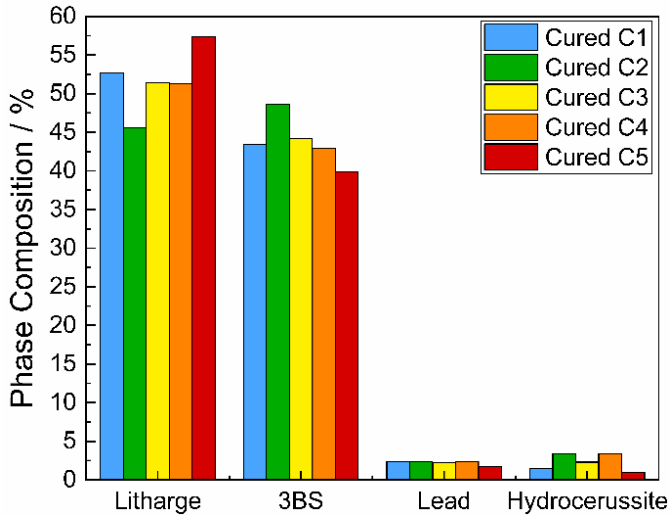

Figure 24: The crystalline phase composition of the cured negative electrodes containing C1, C2, C3, C4 and C5.

3.2.3 Dynamic charge acceptance of lead-carbon electrodes

This chapter presents and discusses the electrochemical performance of the lead-carbon electrodes in terms of charge acceptance. Three different charge acceptance tests are applied on the lead-acid cells, which includes CA test 2 according to the SBA standard and the DCA test from the EN as well as the Run-in (long-term DCA) test developed by Ford. The following paragraphs present first the formation profile of the lead-acid cells and then the results obtained from three different charge acceptance tests are compared.

Formation

Laboratory cells were formed by applying different constant currents stepwise. An example of a cell formation profile, including the cell voltage, half-cell potential of the positive and negative electrode vs. RHE, is shown in Figure 25a. During the formation of a negative plate, the lead compounds (3BS and PbO) are reduced to Pb through

electrochemical reactions. After the reduction of these lead compounds, with an increase of the potential, the hydrogen evolution reaction commences [1,2]. The sharp increase in the negative plate potential and the cell voltage after 15 h indicate a fully-charged negative electrode. The overcharge potential generated afterwards is limited due to the HER occurring at the negative electrode. In the case of the positive plate, PbO and basic lead sulfates are oxidized to PbO_2. As the concentration of these compounds diminishes, the positive plate potential will raise and then the oxidation of $PbSO_4$ takes place [1,2]. The slight increase of the positive plate potential after 15 h can be attributed to the oxidation of $PbSO_4$.

The cell voltage profile of laboratory cells containing five different carbon additives is presented in Figure 25b. Due to the limitation of overcharge potential by the HER, the electrochemical activity of cells in terms of the HER can be already predicted from the end of cell voltage. Higher cell voltages during overcharging indicate a greater HER overpotential on the negative electrodes, meaning a lower activity towards the HER. As seen in Figure 25b, the cells with higher S_{ext} of carbons (C3, C4 and C5) exhibit lower end of formation voltages (around 2.45 V). On the other hand, lower S_{ext} carbon-containing cells (C1 and C2) possess greater end of formation voltages (2.7 V for C1 and 2.5 V for C2).

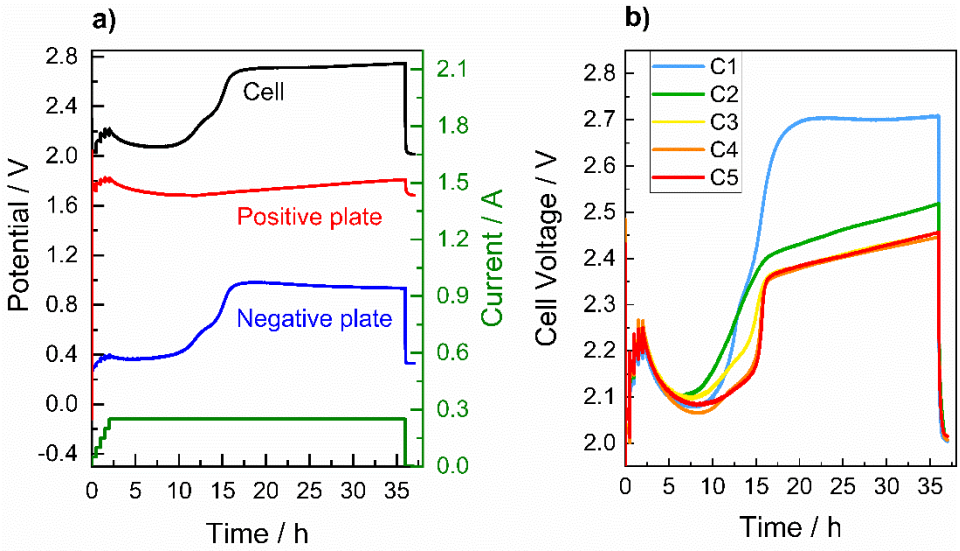

Figure 25: a) Cell voltage (black), half-cell potential of the positive (red) and negative plate (blue) vs. RHE as well as current profile (green) during formation. b) Voltage profile of laboratory cells containing C1, C2, C3, C4 and C5 additives during formation.

In general, the formation profile of the lead-acid cells shows that the negative plates with greater S_{ext} of carbon additive have a tendency to exhibit increased HER activity. At this

stage, it is not possible to differentiate the HER activities of the C3, C4 and C5 from the end of formation voltages of the cells.

3.2.3.1 Charge acceptance test 2 (SBA)

The charge acceptance test 2, developed by the Battery Association of Japan (SBA S0101:2014) is applied on the laboratory cells in order to evaluate the charge acceptance. In comparison to other charge acceptance tests, the SBA test is a short test, which includes only a single charge pulse for 10 s after a cell has been discharged to 91.5 % SoC.

Figure 26a illustrates the charge currents of cells containing five different carbon additives during the 10 s charge pulse. The obtained charge currents are normalized to the 20 h discharge capacity of a respective cell. The current overshoot during the first seconds is an artifact, which results from the voltage regulation of the test channel. However, its effect on the cumulative charge current is less than 5 % and therefore can be accepted. As can be seen in Figure 26a, there is a stepwise increase of the charging current values from C1 to C4. C4 and C5 cells possess almost the same normalized currents.

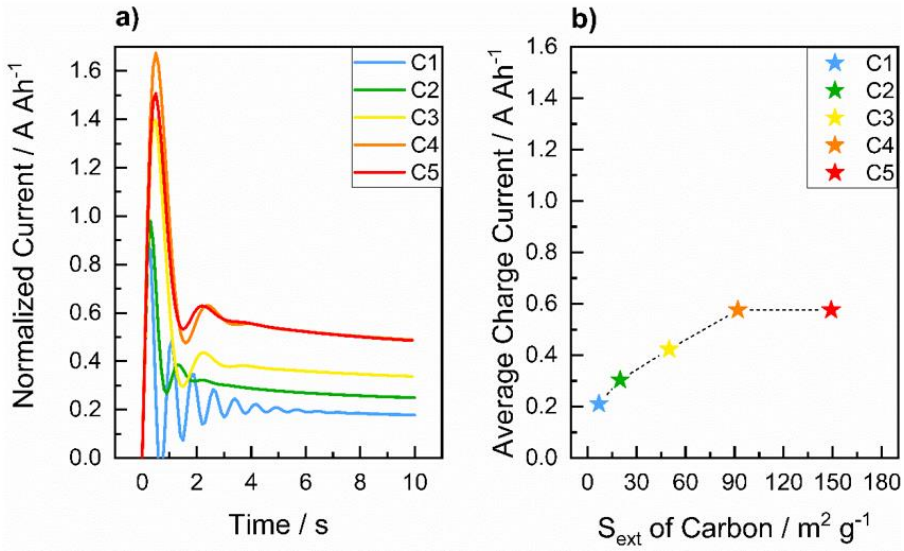

Figure 26: a) Current profiles of laboratory cells containing C1, C2, C3, C4 and C5 additives obtained from the CA test 2 according to the Japanese standard (SBA S0101:2014). b) Relationship between the charge acceptance and S_{ext} of carbon additives (the figure was reproduced from Bozkaya et al. [154]).

The average charge current calculated from the 10 s charge pulse is plotted with respect to the S_{ext} of carbons, which is shown in Figure 26b. The average charge current of cells are 0.21 A Ah^{-1}, 0.30 A Ah^{-1}, 0.42 A Ah^{-1} and 0.58 A Ah^{-1} for C1, C2, C3 and C4, respectively. There is almost a linear relationship between the charge acceptance and

S_{ext} of carbons. A further increase of the S_{ext} of carbon from 92.1 $m^2 g^{-1}$ (C4) to 159.3 $m^2 g^{-1}$ (C5) does not enhance the charging currents anymore. This might be due to several reasons. First, the charge acceptance might be saturating at high charging currents due to the limitations in the cell (e.g. grid design) instead of the negative active material formulation. Second, the charge acceptance limitation might arise from the limitation of mixing small carbon particles in the negative paste. As the particle size of carbon is smaller, the mixing of such carbon particles in the negative paste is much more difficult since the carbon particles tend to agglomerate. This phenomenon can be clearly seen in the SEM micrographs of the cured negative electrodes (Figure 22), especially for C4 and C5. Third, the cell with C4 additive might provide the maximum adsorption of lignosulfonate to the carbon surface. An additional surface provided by the C5 additive may not affect the interaction between lignosulfonate and carbon remarkably.

For further understanding, the half-cell potentials as well as the cell voltage profiles of all cells during 10 s charge pulse are compared in Figure 27. The half-cell potential values of negative and positive electrodes are plotted with respect to the RHE. The profile of the negative electrode potential (Figure 27a) and cell voltage (Figure 27c) suggest that the charge acceptance is limited by the negative electrode. In the case of the positive electrode (Figure 27b), the change in potential values is negligible, which is in the range between 1.75 V and 1.83 V vs. RHE. Therefore, the cell setup with the oversized positive electrodes clearly limits the negative electrode, which leads to the measurement of the current consumption of the negative electrode during the SBA charge acceptance test.

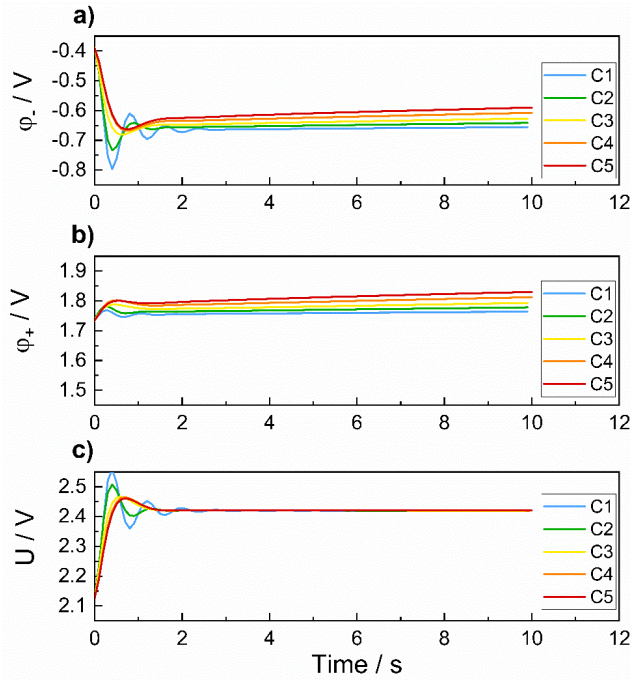

Figure 27: a) Negative electrode potential; b) positive electrode potential; c) cell voltage profile during 10 s charge pulse obtained from CA test 2 according to SBA.

The SBA test results show that the charge acceptance test containing a single charge pulse can reveal the influence of carbon external surface area on the charging currents. However, the charge acceptance of the cells containing C4 and C5 cannot be differentiated at this point. The following chapters further discuss whether the impact of carbon additives is similar in its magnitude for the other charge acceptance tests.

3.2.3.2 Dynamic charge acceptance test (EN)

In the DCA test according to the EN 50342-6, the charging currents of batteries are determined after charge history at 80% SoC, after discharge history at 90% SoC and during one week stop/start drive cycle at 80% SoC. The obtained average charge current values are named as I_c, I_d and I_r, respectively. Based on these three average charge currents, a general dynamic charge acceptance is then calculated according to equation 31.

The normalized charge currents of cells containing C1, C2, C3, C4 and C5 additives after charge history, after discharge history and during one week simulated stop/start drive cycle are shown in Figure 28. In the case of I_c (Figure 28a), increased charging currents are observed from C1 to C3 over the 20 charge pulses. By using C4 and C5 carbon additives in the negative electrodes, no further enhancement of I_c is observed. Regarding I_d (Figure 28b), the charging currents are promoted from C1 to C4, where similar currents values are obtained for C4 and C5. The saturation of charge acceptance values was also observed in the SBA test. This phenomenon is especially obtained for the cells providing high charging currents (>1 A Ah^{-1}) and it might be associated with the unknown limiting effects in the cell (e.g. electrode grid and dispersion of carbon particles). Further, the obtained charging behavior of cells for I_c and I_d are similar to the trend observed for 12 V batteries [74]. It can be seen that I_c is much lower than I_d. It is assumed that this is due to the fact that after charge history all small lead sulfate crystals are already dissolved in the previous charge step and therefore only big and poorly soluble lead sulfate crystals are available for the charge pulses of the test [159,160]. Figure 28c presents a one-week simulated stop/start drive cycle of lead-acid cells. In this I_r graph, each dot represents the charging currents obtained from each trip. One day of a drive cycle consists of 3 trips and each day is followed by a night parking. After the completion of 5 days of cycling, 2 days of weekend parking take place. It can be seen in Figure 28c that the charging currents of cells are enhanced by increasing carbon´s external surface area. The cycling trend in the DCRss profile of laboratory cells is known from 12 V batteries [74]. An increased charging current during each trip (3 trips per day) and a reduced charging current after every night are observed for all cells. For the cells C1, C2 and C3, this trend is not observed on the first day of cycling.

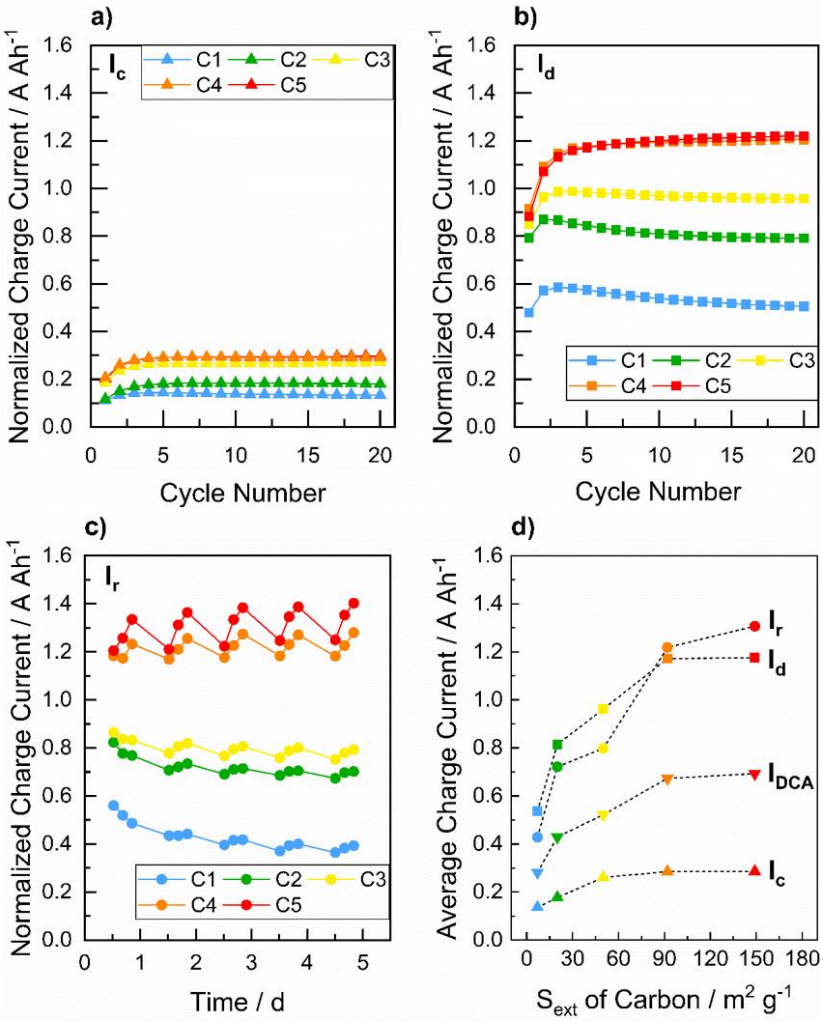

Figure 28: a) Normalized charge current of cells containing C1, C2, C3, C4 and C5 additives after charge history (I_c); b) after discharge history (I_d); c) during one week simulated stop/start drive cycle (I_r) obtained from the dynamic charge acceptance test (EN 50342-6:2015). d) Relationship between average charge current (I_c, I_d and I_r) and dynamic charge acceptance (I_{DCA}), where the I_{DCA} is calculated from the equation 31. The figure was adapted from Bozkaya et al. [154].

The average charge currents (I_c, I_d and I_r) calculated from the charge pulses, as well as the dynamic charge acceptance (I_{DCA}) are plotted with respect to the external surface area of the carbon additives (Figure 28d). Obviously, the charge acceptance of cells is improved via an increase of carbon´s external surface area for all short-term histories which was also shown for similar carbons [72]. The average charge currents I_c and I_d are improved by a factor of 2 (from 0.14 A Ah^{-1} to 0.29 A Ah^{-1} for I_c, from 0.54 A Ah^{-1} to 1.18 A Ah^{-1} for I_d). In case of I_r, the charging current is enhanced by a factor of 3 (from 0.43 A Ah^{-1} to 1.31 A Ah^{-1}). The dynamic charge acceptance of C1, C2, C3, C4 and C5 cells are 0.28 A Ah^{-1}, 0.43 A Ah^{-1}, 0.52 A Ah^{-1}, 0.67 A Ah^{-1} and 0.69 A Ah^{-1}, respectively.

An increase of the external surface area of carbon from 7.1 $m^2 g^{-1}$ (C1) to 159.3 $m^2 g^{-1}$ (C5) promotes the final DCA by a factor of 2.5.

For further understanding, the half-cell potentials as well as the cell voltage profiles of all cells during 10 s charge pulse are compared in Figure 29. The presented voltage profiles are taken from the 10th cycle of the DCA_{pp} profile after discharge history (I_d). The voltage overshoot during the first seconds is an artifact due to the voltage regulation of the battery test channel. This is much more dominant for the cell with the lowest charge acceptance (C1). However, the impact of the voltage overshoot on the charge acceptance is negligible, which is less than 5%. The voltage profile of the negative electrode (Figure 29a) and the complete cell (Figure 29c) imply that the charge acceptance is limited by the negative electrode. For the positive electrode (Figure 29b), the change in potential during the 10 s charge pulse is around 10 mV, which is considered negligible. Thus, similar to the observations obtained from the SBA CA test, the limitation of the negative electrode in this cell setup enables measuring the current consumption of the negative electrode during the DCA test.

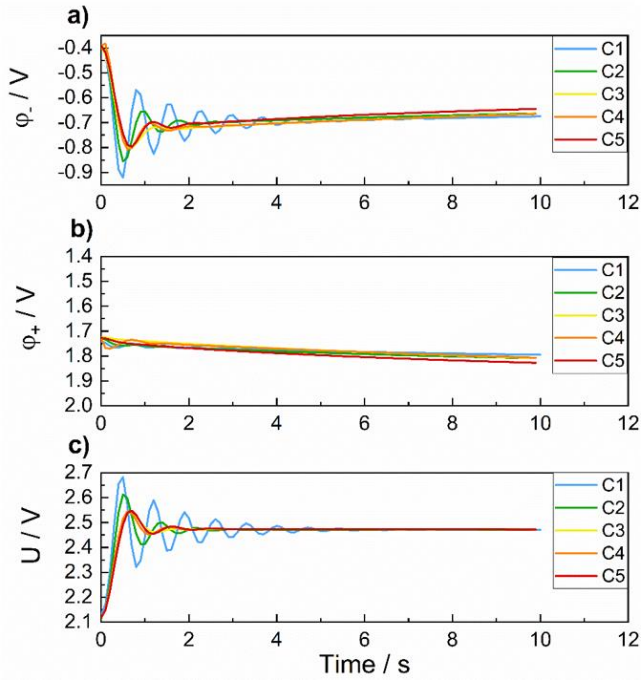

Figure 29: a) Negative electrode potential; b) positive electrode potential; c) cell voltage profile during 10 s charge pulse obtained from the 10th cycle of the DCA_{pp} profile for I_d.

The results obtained from the dynamic charge acceptance test according to the EN 50342-6:2015 show that the impact of carbon external surface on three different charging currents as well as the final DCA can be revealed. It is observed that the influence of carbon additives on the charge acceptance values depends on the history

of cells. After charge history, only I_c of C1, C2 and C3 can be differentiated. The I_c of C3, C4 and C5 are similar, which is even the same for C4 and C5. After discharge history, it is possible to distinguish the I_d of C1, C2, C3 and C4. The I_d of C4 and C5 are almost the same. Similar behavior was also observed for the charging currents obtained from the SBA test (chapter 3.2.3.1). This similarity can be attributed to the fact that both I_d and the CA test 2 from the SBA standard are determined after discharge history of cells. During one week simulates stop/start drive cycle, the carbon surface effect is the most dominant. Still, the I_r of C4 and C5 is comparable. The following chapter shows and discusses whether the impact of carbon external surface area can be still obtained in a long-term DCA test.

3.2.3.3 Run-in DCA test (Ford)

The long-term Run-in DCA test developed by Ford simulates a real-world usage profile in micro-hybrid vehicles. The Run-in test is a sequence of several weeks of stop/start drive cycles similar to the DCRss part of the DCA test. Differences between the Run-in DCA test and the DCA (EN) are explained in the experimental part (chapter 3.1.4). The Run-in test consists of 3 weeks of modified DCRss test followed by 1 month of airport parking and then 4 weeks of modified DCRss test.

General evaluation

The recuperation currents (I_{recu}) of laboratory cells obtained from the DCRss part of the DCA (EN) test (first week) and the subsequent conducted Run-in DCA test are presented in Figure 30. Each dot represents the average DCA during a simulated trip. Each week includes 5 days of stop/start cycling and 2 days of weekend parking. Each day consists of 3 trips. Thus, one week contains 15 trips in total, which corresponds to 15 dots (average DCA) in Figure 30. The continuous curves show the moving weekly average for each cell, which is calculated by averaging 15 I_{recu} values. Similar to the DCRss part of the DCA (EN) test (Figure 28c), a weekly trend of the I_{recu} is also observed for the Run-in test, which is known from commercially available car batteries [26]. The charge acceptance increases during the simulated daytime and throughout the first 5 days of the simulated week and is reduced during the night as well as over the weekend. As a result, the DCA is strongly affected by these rest periods. This trend is observed for C3, C4 and C5 cells during 3 weeks of the Run-in and 4 weeks of the Run-in test executed after airport parking. In case of cells with very low charge acceptance (C1 and C2), this trend cannot be observed after airport parking.

During 1 month of a rest period, so-called airport parking, only key-off load resistors discharge the cells. Hence, the cells require a certain time period to reach the targeted 80% SoC level again. After one month of airport parking, for C3, C4 and C5 cells, DCA

decreases first within one week and then it increases towards the end of the week. This observation can be explained in the following sentences. Since the cells have lower SoC than 80 % after airport parking, the cells were charged at all possible steps (current and voltage setpoints depending on the SoC deviation from 80 % SoC) to reach the target SoC. Due to this sequence of charging events, lower DCA values are obtained, as the batteries are charged with a short-term charge history (compared to I_c in the EN test). When the cells reach the target SoC, the cells are either discharged or kept at rest during the “SoC-deviation” steps, which results in higher DCA values.

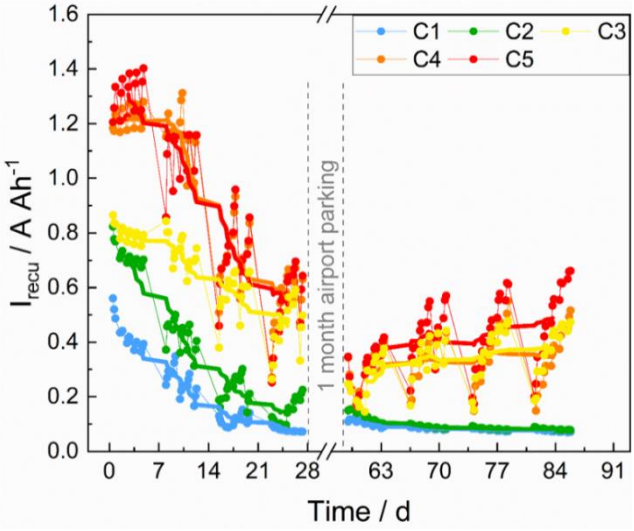

Figure 30: The recuperation currents of the laboratory cells containing C1, C2, C3, C4 and C5 additives obtained from the 1 week of DCRss part of the DCA (EN) test, 3 weeks of Run-in DCA test, and another 4 weeks of Run-in DCA test (the figure was reproduced from Bozkaya et al. [154]).

Functionality of test algorithm

In order to keep the SoC level at the target of 80 % SoC, the Run-in test includes an ampere-hour (charge) balance as explained in the experimental part (chapter 3.1.4). One-third of the quiescent drain caused by the key-off load is compensated for the charge balance of each cell. This key-off load correction (AhKOL) takes place after parking of each trip (3.3 hours), after night parking (12 hours) and after weekend parking (60 hours). Besides, two-third of the charge balance is controlled by the quasi-open circuit potential which is measured every morning. This correction (AhOCV) occurs if the open-circuit voltage of a cell falls below the targeted value at 80% SoC (OCV80). As a result of the combination of both AhKOL and AhOCV corrections in this test, the quasi-OCV recorded overnight and weekend rest periods, which is called V6h, should show the characteristic weekly sawtooth swing. To investigate the validation of this algorithm in a 2 V cell-level, a more detailed analysis of the Run-in results is made by plotting the V6h values recorded after night and weekend parking (Figure 31). Each point represents

the OCV of a cell measured after certain parking periods. The V6h values start at day 8 since the 3 weeks of the Run-in DCA test results have been executed after 1 week of the DCRss part of the DCA (EN) test. Thus, the same x-axis (time) is kept for plotting the V6h values to avoid confusion. The first V6h values are the OCV of each cell before starting the Run-in test. The first V6h values of the cells are between 2.097 V and 2.104 V, meaning that no difference in the OCV of the cells is introduced after 1 week of the DCRss (EN). The following five V6h values are the daily quasi-OCVs of each cell after night parking from Monday to Friday. The sixth V6h value corresponds to the quasi-OCV after weekend parking. Only the first week of the 3 weeks of the Run-in test (from day 8 to day 15) and the first week of the 4 weeks of the Run-in test (from day 62 to day 69) consist of seven V6h values. Since these two starting weeks include an OCV value after DCRss (EN) and an OCV after airport parking. As seen in Figure 31, all cells possess the characteristic weekly sawtooth swing during 3 weeks of the Run-in test (from day 8 to day 30). The weekend parking is the main driver of the sawtooth swing since the low V6h on Monday morning is increased in the following day. Another contribution to this sawtooth swing of V6h values results from the fact that the targeted OCV value (OCV80), which is 2.105 V at 80% SoC for all cells, is tried to be reached by either charge, discharge or rest periods. Considering the V6h values of the second part of the Run-in test (from day 62 to day 91), the algorithm works for C3, C4 and C5 cells. However, the V6h is increasing for the cells with a low external surface area of carbons (C1 and C2). Due to the low rechargeability of the C1 and C2, which can be seen from the last moving average values of I_{recu} at the end of the first Run-in test, these cells cannot be efficiently charged to reach the OCV80 values after airport parking. The V6h values of the cells are between 2.062 V and 2.070 V after airport parking due to the introduced significant acid stratification. Therefore, the reason for the continuous increase of the V6h values for C1 and C2 might be explained by their low DCA.

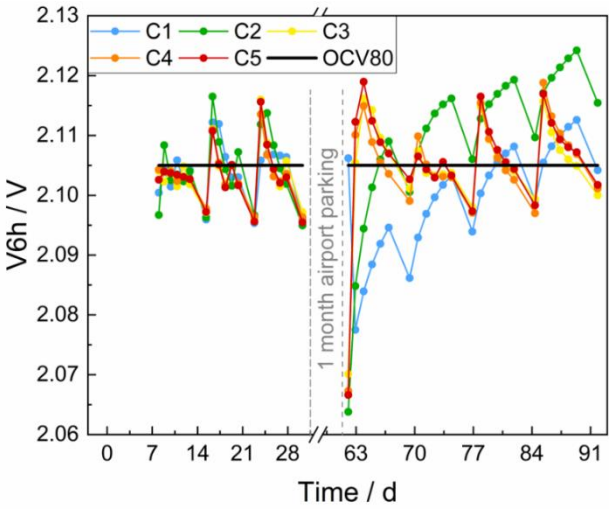

Figure 31: Cell voltages (V6h) after standstill (night and weekend parking) obtained from the Run-in DCA test (the figure was reproduced from Bozkaya et al. [154]).

Carbon effect

The impact of the external surface area of carbon during the drive cycle can be explained in the following sentences. In the first 3 weeks of the Run-in cycling, the cells containing higher S_{ext} (C4 and C5) possess the highest recuperation currents (Figure 30). As the external surface area of carbon additives decreases, a reduction in the charge acceptance of cells is observed. After airport parking, the impact of carbon external surface area seems to differ (Figure 30). Only high DCA cells (C3, C4 and C5) and low DCA cells (C1 and C2) can be differentiated. This observation is probably related to the self-amplifying effect of low DCA. The batteries with a poor charge acceptance tend to fade overproportionally in this test due to the increased number of charging steps after charge history. The cells C1 and C2 cannot be efficiently charged (even at continuous charging), as the charging currents falls below 0.15 A Ah^{-1}. In the case of the batteries with a superior charge acceptance, the recuperation currents can be kept still high during several weeks of the Run-in test. Based on the above findings, a correlation between carbon external surface area and the DCA can only be revealed for the first 3 weeks of the Run-in test.

Run-in effect

As can be seen in Figure 30, a remarkable decline in the recuperation currents of all cells after each weekend is observed for the first 3 weeks of the Run-in test. After airport parking, all cells reach stabilized DCA values at the end of the Run-in test. This behavior is generally observed for 12 V lead-acid batteries after several weeks of cycling, which is known as “Run-in” effect [74]. In this work, a similar trend is also achieved with 2 V lead-acid cells containing different carbon additives.

It has been revealed that the Run-in effect is mostly reversible [74]. In order to elucidate the reversibility of laboratory cells, three selected cells (C2, C3 and C4) were further tested. After the completion of the Run-in test, the resistors were disconnected from the cell terminals and then the cells were rested for 4 months. It is known that the 2 V lead-acid cells used in this work have an acid density of 1.26 g ml^{-1} at 80% SoC. After this 4 months of a rest period, the acid density of all cells was between 1.248 g ml^{-1} and 1.256 g ml^{-1}. The acid density of cells was adjusted to 1.26 g ml^{-1}. Then, the cells were subjected to the pre-cycling test, including two times reserve capacity and one 20 hour-rate discharge capacity determination. Afterwards, the 4 weeks of the Run-in test was carried out. The recuperation currents of C2, C3 and C4 cells obtained from the second Run-in test is presented in Figure 32. In order to compare the DCA values before and after the pre-cycling test, the I_{recu} obtained from the first Run-in test is also included in Figure 32. It can be seen that the recuperation currents of all cells significantly increase after the pre-cycling test (from 0.08 A Ah^{-1} to 0.48 A Ah^{-1} for C2, from 0.38 A Ah^{-1} to

0.69 A Ah^{-1} for C3, and from 0.35 A Ah^{-1} to 0.68 A Ah^{-1} for C4). Within the first week of the Run-in test, I_{recu} values of all cells significantly decrease. From the second week on, the reduction in I_{recu} of all cells is relatively low, which implies a stabilized DCA. The obtained results suggest that the Run-in effect is also largely reversible in cell-level as in the case of 12 V batteries. The pre-cycling test which is applied after the first Run-in DCA test clearly helps refreshing the laboratory cells leading to much higher DCA values.

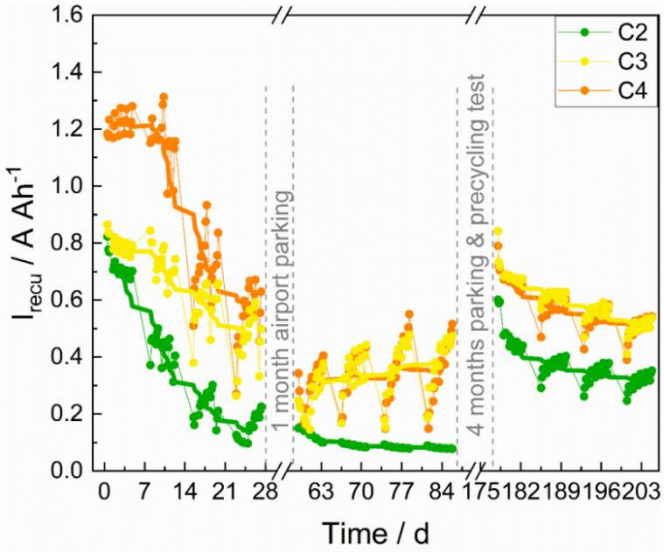

Figure 32: The recuperation currents of the laboratory cells containing C2, C3 and C4, obtained from the first Run-in DCA test and the second Run-in DCA test followed after the pre-cycling test.

3.2.3.4 Comparison of charge acceptance tests

As shown in previous chapters, the rechargeability of 2 V laboratory cells was investigated by three different charge acceptance tests including short- and long-term tests. The short-term tests are charge acceptance test 2 and dynamic charge acceptance according to battery association of Japan (SBA S 0101:2014) and European norm (EN 50342-6:2015), respectively. The long-term test is the Run-in DCA test which simulates a real-world usage profile in a micro-hybrid vehicle. The results obtained from these three different charge acceptance tests are compared in Figure 33.

A strong correlation between charge acceptance according to SBA and EN standards is observed (Figure 33a). The SBA test determines the charge acceptance from a single charge pulse at 91.5% SoC after discharge history. The EN test evaluates the so-called “dynamic charge acceptance” after charge history (80% SoC), after discharge history (90% SoC) and during several microcycles (80% SoC). Despite the differences in these tests, the impact of carbon additives on recharge currents is qualitatively similar. The higher external surface area of carbon clearly improves both $I_{CA\ 2\ (SBA)}$ and $I_{DCA\ (EN)}$.

Further, the recharging ability of cells with high S_{ext} of carbon (C4 and C5) cannot be differentiated in both SBA and EN tests. In terms of quantitative comparison, the average charge currents obtained from the DCA test ($I_{DCA\ (EN)}$) are slightly higher than the ones obtained from the CA test 2 ($I_{CA\ 2\ (SBA)}$) for all cells. This observation is different than the obtained trend with other 2 V lead-acid cells [161]. It was found that the cells deliver higher charge currents obtained from the SBA test in comparison to the EN test. This finding is explained within the test protocol itself. Since the charge acceptance is determined only after discharge history of cells by SBA test, the obtained charge current is expected to be higher than the DCA test including CA determination after or during different histories [161]. In this work, the cells were subjected to the SBA test directly after formation. The DCA (EN) test was conducted after the pre-cycling and cyclic voltammetry tests as explained in the experimental part (chapter 3.1.4). In general, execution of the capacity determination tests such as the pre-cycling and initial cycling test help to increase the active mass utilization of lead electrodes due to charge and discharge cycling at slow rates. This leads to a slight increase in the discharge capacity of the negative electrodes which might also slightly enhance the charging currents. Therefore, higher charge acceptance values obtained by the SBA test in comparison to the EN test might be attributed to the test execution order.

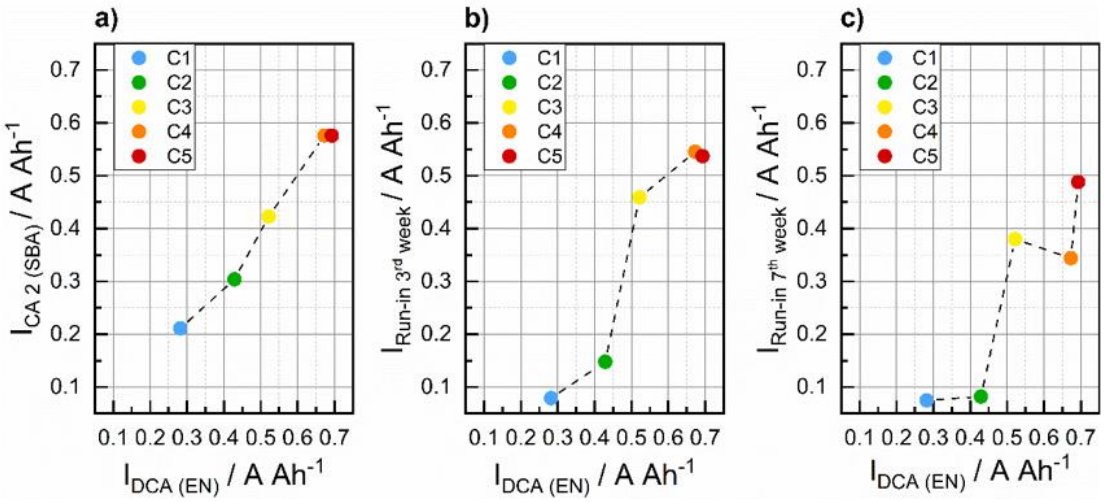

Figure 33: Relationship between charge acceptance values of cells containing different carbon additives obtained from a) DCA (EN) test and CA test 2 (SBA); b) DCA (EN) test and 3 weeks of Run-in DCA test (Ford); and c) DCA (EN) test and complete Run-in DCA test (Ford). The figure was reproduced from Bozkaya et al. [154].

Figure 33b presents the relationship between the charge acceptance values obtained from the DCA (EN) test and the DCA after 3 weeks of the Run-in test. The $I_{Run\text{-}in\ 3rd\ week}$ values are the last moving average of I_{recu} (day 25 in Figure 30) for each cell. It can be seen in Figure 33b that the cells containing carbon additives with low S_{ext} (C1 and C2)

show significantly lower charge acceptance after 3 weeks of the run-in drive cycle in comparison to the DCA (EN) test. The charge acceptance of C1 and C2 cells is 0.28 A Ah^{-1} and 0.43 A Ah^{-1} in the DCA (EN) test, whereas the values of 0.08 A Ah^{-1} and 0.15 A Ah^{-1} are reached after 3 weeks of Run-in for C1 and C2, respectively. In the case of the C3, C4 and C5 cells, slightly lower charge acceptance values are observed in the Run-in test when compared with the DCA test. This obtained trend might be due to the protocol of the Run-in test itself since the low DCA batteries are depressed to the minimum levels within the Run-in test. The charge acceptance of C3, C4 and C5 cells according to the DCA test is 0.52 A Ah^{-1}, 0.67 A Ah^{-1} and 0.69 A Ah^{-1}. In the Run-in test, the values are decreased to 0.46 A Ah^{-1}, 0.55 A Ah^{-1} and 0.54 A Ah^{-1}, correspondingly. Even after 3 weeks of the Run-in test, the impact of carbon external surface area on the DCA can be observed. Compared to the short-term DCA test, only variations in the DCA values are observed. However, this observation changes after 1 month of airport parking followed by 4 weeks of the Run-in test. The DCA values obtained at the end of the Run-in test (day 84 in Figure 30), are compared with the ones acquired from the short-term DCA test (Figure 33c). It can be seen that no clear correlation can be achieved between the DCA (EN) and the completed Run-in test. The DCA of C1 and C2 becomes equal at the end of the Run-in test, which is 0.08 A Ah^{-1}. As explained before, this might be resulted from the increased Run-in effect, meaning a decline in DCA value in very low DCA. In the case of the C3, C4 and C5 cells, the Run-in DCA values are 0.38 A Ah^{-1}, 0.34 A Ah^{-1} and 0.49 A Ah^{-1}, respectively. Despite the clear difference between C3 and C4 cells in the short-term DCA (EN) test, these cells reach similar DCA values after several weeks of DCA testing. This might be either due to the good cycling ability of the C3 cell or an unknown fading behavior of the C4 cell. At this point, it is not possible to determine the origin of this similarity completely. Within the Run-in test executed after airport parking, only a differentiation between high (C3, C4 and C5) and low DCA (C1 and C2) cells can be made.

In general, the discrepancy between the DCA (EN) and Run-in tests can be attributed to the fact that no stable DCA levels can be reached within the short-term DCA test. Therefore, it is expected to receive much higher charge acceptance values within the short-term DCA (EN) test. The impact of carbon type on the charge acceptance is similar for both DCA (EN) and 3 weeks of the Run-in test. Nevertheless, the influence of carbon type seems to differ for the Run-in test applied after 1 month of airport parking. This might result from the accelerated acid stratification as well as the formed large $PbSO_4$ crystals due to the long-term parking period. Hence, revealing the influence of carbon external surface area on the long-term DCA testing can be made up to a certain extent. Although the shorter version of the DCA test, according to EN, was implemented to predict the real DCA value, neither the trend of carbon additives nor the DCA can be kept through the whole Run-in DCA test. Further investigation in this topic, such as testing higher number of cells or even more carbon additives, is necessary at this point.

3.2.4 Electrochemical activity of lead-carbon electrodes

In order to establish a correlation between the charge acceptance of lead-acid cells and the electrochemical properties of lead-carbon electrodes, the electrochemical activity of negative electrodes was investigated via cyclic voltammetry and EIS measurements.

3.2.4.1 Cyclic voltammetry

The impact of carbon external surface area on the current-potential relationship of the negative electrodes has been shown and discussed in [10,72]. In this work, it was essential to reproduce the observed trends with the carbon additives used in this study to establish a relationship between the electrochemical activity of the negative electrodes and the charge acceptance of the lead-acid cells obtained from three different test methods. Further, it is important to compare the double-layer capacitance of the negative electrodes obtained from cyclic voltammetry and the electrochemical impedance spectroscopy, which is discussed in the next chapter.

The cyclic voltammetry measurements were performed at the fully-charged state of cells in order to have a homogeneous and defined acid density over the electrode surface. Figure 34 shows the current-potential profile of 5 different negative electrodes obtained from the CV measurements at a scan rate of 10 mV s^{-1}. The shown voltammograms are the 10^{th} cycle for each negative electrode. The current values are normalized to the 20 h discharge capacity of the corresponding negative electrode to eliminate the effects from different electrode weights. The negative electrodes are cycled between the OCV of the electrode (-0.38 V vs. RHE), determined by the equilibrium potential of the main reaction ($Pb/PbSO_4$), and -0.9 V vs. RHE. As seen in Figure 34, during negative polarization, first $PbSO_4$ to Pb reduction takes place which is around -0.4 V vs. RHE. By further negative polarizations, the decomposition of the electrolyte occurs due to the hydrogen evolution reaction, which is especially dominant at potentials lower than -0.7 V vs. RHE. The anodic current at potentials above -0.4 V vs. RHE is caused by the oxidation of Pb to $PbSO_4$. When the start potential of -0.38 V is reached, the voltage scan is reversed and the electrode is charged again. The start and end potential are chosen -0.38 V in this study.

It can be recognized in Figure 34 that the HER activities of the negative electrodes are different. In order to see the impact of carbon type clearly, the absolute current values at a fixed potential at -0.9 V vs. RHE are plotted with respect to the external surface area of the respective carbon, which is shown in Figure 35. A correlation between the HER activity and S_{ext} of carbon is observed. The negative electrodes with higher S_{ext} carbons (C3, C4 and C5) possess greater affinity towards the HER. Further, a saturation of the HER currents can be observed for electrodes with very high S_{ext}. This might be attributed

to the insufficient dispersion of the C4 and C5 carbons which have much smaller primary particles in comparison to other carbons. Therefore, these carbons might be agglomerated in the negative electrode structure, which is observed in the SEM micrographs of the cured negative electrodes (Figure 22).

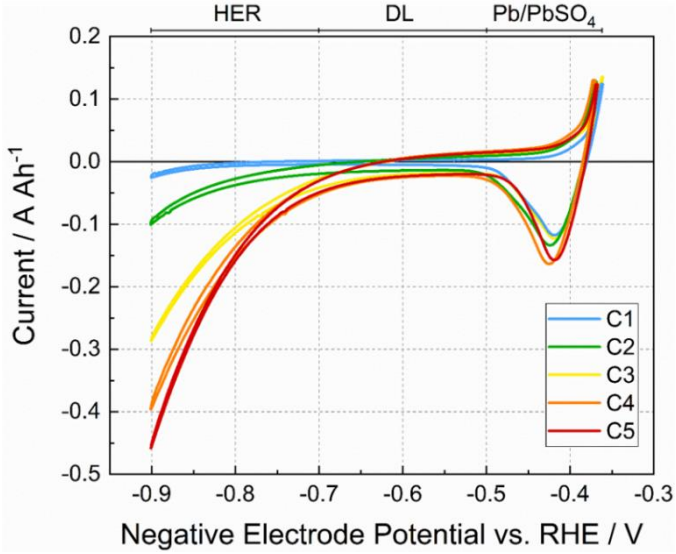

Figure 34: Current-potential relationship of the fully-charged negative electrodes at a scan rate of 10 mV s^{-1} obtained from the cyclic voltammetry test.

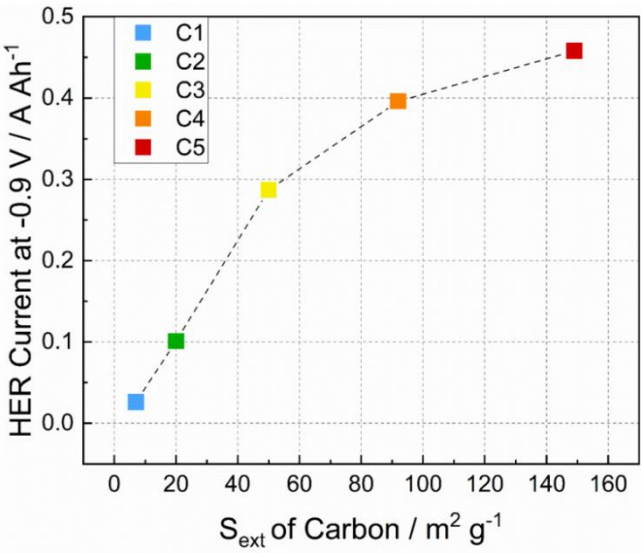

Figure 35: Relationship between the HER currents of negative electrodes and external surface area of carbons.

In addition to the HER activity, the double-layer capacitance of the negative electrodes was also investigated in order to relate the electrochemical active surface of the electrode to the DCA. The negative electrodes were cycled between -0.5 V and -0.7 V

vs. RHE, which corresponds to the potential range between the HER and $Pb/PbSO_4$ reaction in which all faradaic reactions can be neglected. The scan rate of 10 mV s^{-1} is chosen for the CV measurements since the capacitive component can be clearly distinguished from the slower redox reactions[1]. Figure 36 shows the 10th cycle obtained from the CV measurements of fully-charged negative electrodes in the DL region. It can be seen that all voltammograms possess differences in the curvature at higher negative potentials due to the contribution of the HER, which is especially pronounced for the electrodes with higher S_{ext} carbons (C3, C4 and C5). From the average current of forward and backward scan direction, all CVs have a minor cathodic offset current, which is around -0.002 A Ah^{-1}. This phenomenon might be due to the oxygen reduction reaction (ORR)[2]. As described before, the electrodes are fully-charged in CV measurements. Therefore, the diffusion-limited Pb reduction can be eliminated at this point and the only remaining diffusion-limited reaction is the ORR.

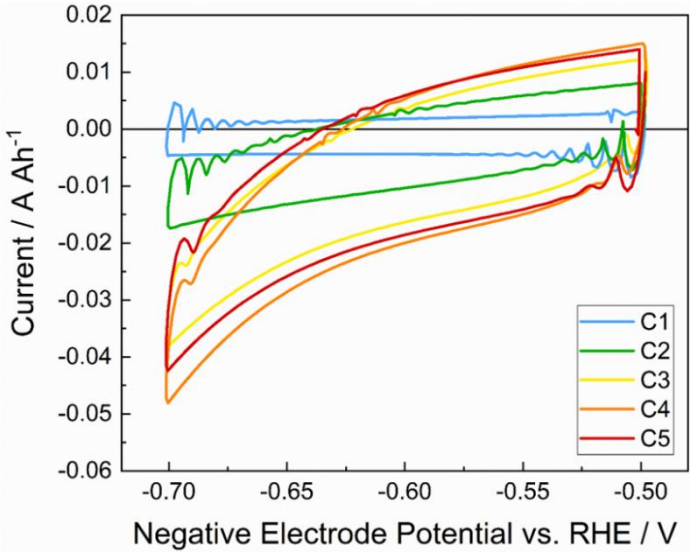

Figure 36: Current-potential relationship of fully-charge negative electrodes in the double-layer region at a scan rate of 10 mV s^{-1} obtained from the cyclic voltammetry test.

By evaluating the difference between forward and backward scans, the differential double-layer (DL) capacitance of each negative electrode was calculated (equation 3). Figure 37 presents the DL capacitance of the negative electrodes in the potential region between -0.53 V and -0.65 V vs. RHE. The DL capacitance values are divided to the 20 h discharge capacity of each negative electrode to eliminate the difference originating from

[1] A higher scan rate of 100 mV s^{-1} or more would be even more suitable to characterize the capacitive currents but are hindered by the very high porosity of electrodes which produce too high currents that can be handled by the galvanostat.

[2] During overcharging, the oxygen is evolved at the positive electrode and is partially dissolved. Afterwards, oxygen diffuses to the negative electrode and is reduced to water.

the weight of electrodes. It is noticeable that there is a slight increase of the DL capacitance of the negative electrodes in higher potentials which is attributed to faradaic reactions such as the HER and Pb reduction and oxidation. As seen in Figure 37, the DL capacitance values increase stepwise from C1 to C5, in which C4 and C5 possess similar values. In order to investigate the impact of carbon on the DL capacitance, the normalized DL capacitance value at a fixed potential of -0.59 V vs. RHE is plotted with respect to the external surface area of carbon, which is shown in Figure 38. Higher S_{ext} of carbon clearly pronounces the DL capacitance of the negative electrodes. It can be seen that increase of S_{ext} from 92.1 $m^2\ g^{-1}$ to 159.3 $m^2\ g^{-1}$ does not enhance the DL capacitance values further. This saturation is much more pronounced for the DL capacitance case as compared to the HER activity, where the C5 electrode shows a slightly higher HER affinity than the C4. This observed saturation for the DL capacitance values might be again attributed to the agglomeration of these small-sized carbon particles (C4 and C5) in the negative electrode structure. Due to this agglomeration, not all small particles could be accessible for the formation of the electrolytic double-layer, which leads to no further improvement in the DL capacitance value.

As a result of the CV measurements, different electrochemical processes are observed, which are the reversible main redox reaction ($Pb/PbSO_4$), the charge of the electrolytic double-layer and the irreversible side reactions (HER and ORR). The obtained results clearly show the influence of the carbon additives on the electrochemical activity of the negative electrodes in terms of HER and the DL capacitance. A similar observation is also obtained for the charge acceptance of lead-acid cells. Therefore, the question arises whether the accelerated electrochemical activity of the negative electrodes could be the reason for an improved charge acceptance.

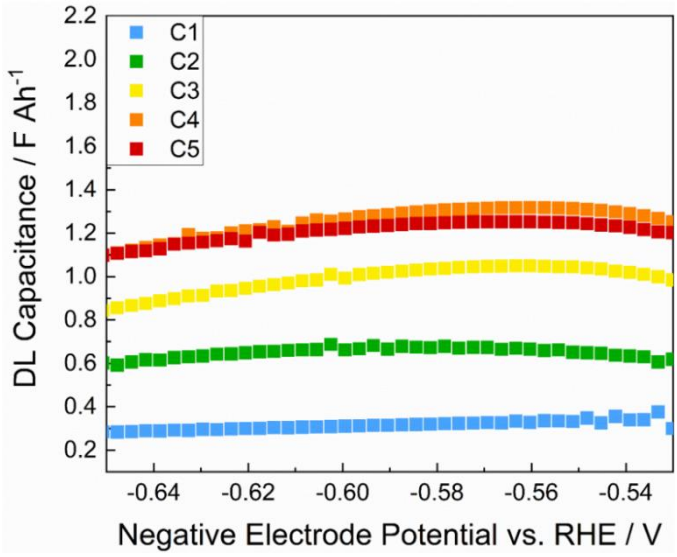

Figure 37: The differential double-layer capacitance of each negative electrode presented in Figure 36.

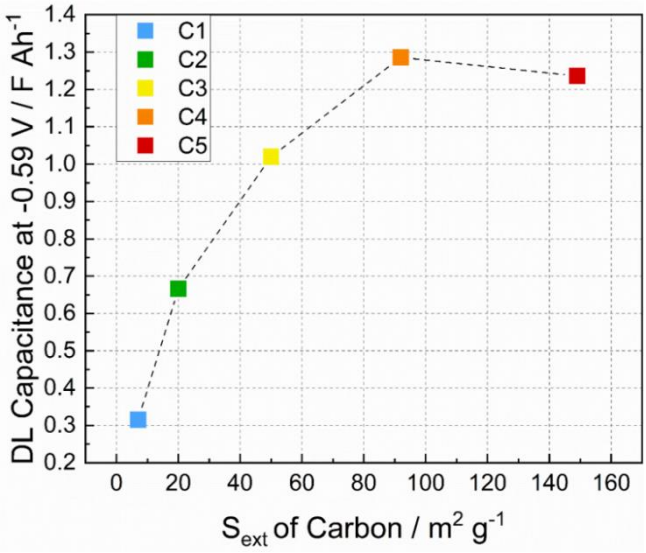

Figure 38: Relationship between the differential double-layer capacitance of negative electrodes and external surface area of carbons.

To findout the current contribution of the HER and the DL capacitance, the absolute current values of the HER, DL and DCA are compared at the respective electrode potential. For the determination of charge acceptance, charge pulses applied in all three tests were conducted at a constant voltage of around 2.5 V on cells, which corresponds to around -0.7 V vs. RHE for negative electrodes. According to the CV measurements conducted in the complete potential window of negative electrodes (Figure 34), the HER currents at -0.7 V vs. RHE are determined. Figure 39 shows the relationship between the HER current values and the charge acceptance of cells obtained from three different tests. For all charge acceptance tests, higher HER activity of negative electrodes seems to improve the recharging ability of cells. According to the cyclic voltammetry measurements performed at 100% SoC, the difference in the HER currents between C5 and C1 is determined as 0.045 A Ah^{-1}. In terms of the charge acceptance tests performed mainly at 80% SoC, the difference in the charging currents of C5 and C1 are 0.37 A Ah^{-1}, 0.41 A Ah^{-1} and 0.46 A Ah^{-1} according to SBA, DCA (EN) and Run-in tests, correspondingly. Therefore, the difference in charge acceptance is almost ten times higher than the differences within the HER. Additionally, the current contribution of the HER is further reduced at the partial state of charge in comparison to the complete state of charge. Therefore, the current values resulted from the HER cannot generate the variations in DCA since the measured currents from the CV and CA tests differ by one order of magnitude.

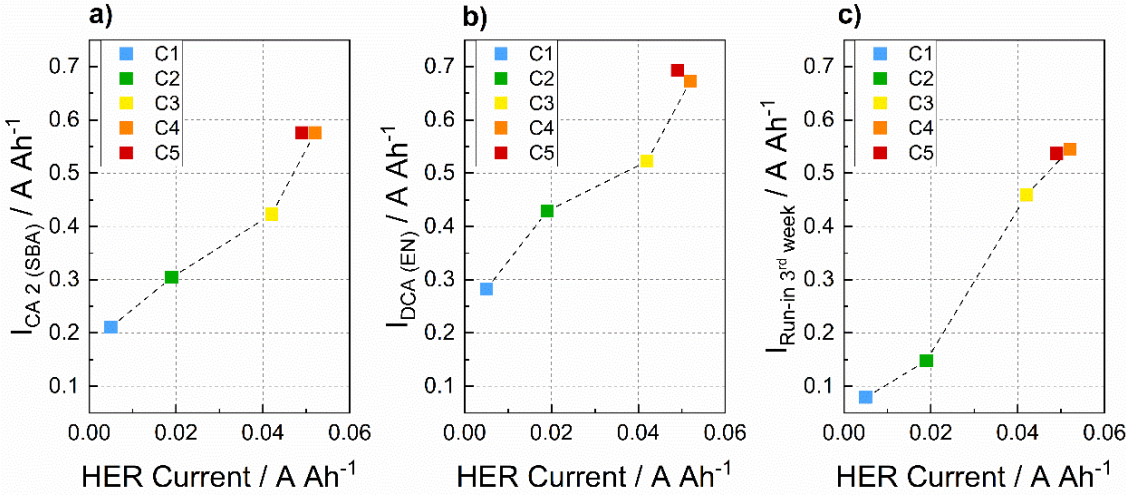

Figure 39: Relationship between the HER activity of the negative electrodes at -0.7 V vs. RHE obtained from the cyclic voltammetry measurements and the charge acceptance according to a) CA test 2 (SBA); b) DCA test (EN) and c) 3 weeks of Run-in DCA test (Ford).

Considering the influence of the DL capacitance, the values calculated at the potential of -0.59 V vs. RHE according to the CV measurements are plotted against the charge acceptance of cells, which is shown in Figure 40. A correlation between the DL capacitance of negative electrodes and the charge acceptance of cells according to three different tests can be established. When the DL capacitance of C5 and C1 is compared, the difference is 0.92 F Ah^{-1}. As a consequence of a charge pulse, the negative electrodes are polarized by 0.3 V, which generates a maximum charge of 0.28 As Ah^{-1} according to the formula $Q = C \cdot \Delta U$. For example, SBA and EN charge acceptance tests include a charge pulse for 10 s. That means an additional charge current of 0.028 A Ah^{-1} can be generated due to the difference in DL capacitance of C5 and C1. However, the difference in charge acceptance of these cells is around 0.4 A Ah^{-1}. This value is more than one order of magnitude bigger in comparison to variation in the DL capacitance. Hence, the DL capacitance alone cannot generate this difference in DCA.

As a result of the cyclic voltammetry measurements, higher electrochemical activity of the negative electrodes in terms of HER activity and the DL capacitance seems to enhance the charge acceptance of lead-acid cells according to CA test 2 (SBA), DCA (EN) and Run-in DCA test (Ford). Based on the calculations made by the differences in the DL capacitance values as well as the HER currents, neither the DL capacitance nor the HER could be the reason for the improved DCA of 2 V lead-acid cells. This implies that the increase in charge acceptance and electrochemical activity has a similar origin but the effect on the DCA is much higher. That could be attributed to the increased electrochemically active surface area of negative electrodes through an increase in the external surface area of carbon. A similar observation was obtained by [10] just for the

DCA (EN) test. In this work, other charge acceptance tests both in the short- and long-term deliver also similar results and correlations. The following chapter presents and discusses whether the DCA increase can be explained by the electrochemical processes which are investigated with the electrochemical impedance spectroscopy.

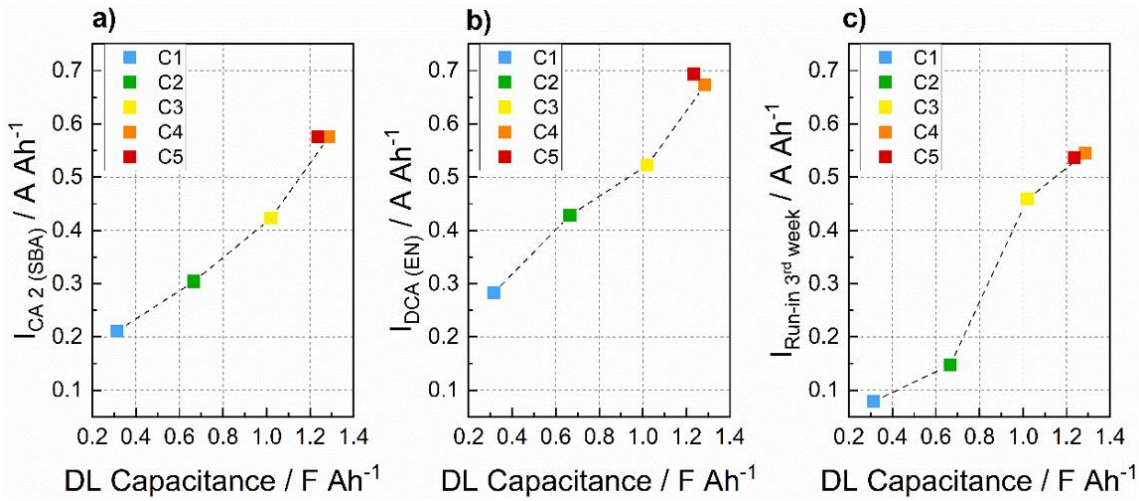

Figure 40: Relationship between the differential double-layer capacitance of the negative electrodes obtained from the cyclic voltammetry measurements and the charge acceptance according to a) CA test 2 (SBA); b) DCA test (EN) and c) 3 weeks of Run-in DCA test (Ford).

3.2.4.2 Electrochemical impedance spectroscopy

The EIS measurements were performed to analyze the dynamic behavior of lead-acid cells. One way to represent the impedance (Z) is a Nyquist diagram which illustrates its real part on the x-axis and its imaginary part on the y-axis. The Nyquist-diagram of complete cell, positive and negative electrode over a frequency range from 6.5 kHz to 10 mHz is shown in Figure 41. It should be first mentioned that the ohmic offset is removed for a better comparison of the impedance. The positive imaginary part in the high-frequency region is generated by the inductive impedance which is related to the inductance of the cables as well as current collectors [162]. The spectrum of complete cells appears as semi-circle and tail (Figure 41a), which is consistent with the other impedance spectra measured with superimposed dc currents [45,47,163]. The high-frequency semi-circle of the Nyquist diagram is often associated with the charge-transfer resistance and the double-layer capacitance [164–166]. In general, the cells with higher S_{ext} of carbons tend to possess smaller semi-circles. The smallest semi-circle is obtained by C4 and C5, followed by C3. On the other hand, the cells with lower S_{ext} of carbons, C1 and C2, provide the largest semi-circles. The tail part might be attributed to the diffusion hindrance [164]. The impedance spectrum of the positive electrode is presented in Figure 41b. A similar shape in the spectra of the positive

electrode was also observed for the 2 V, 10 Ah lead-acid cells, in which the EIS measurements were executed at 80 % SoC with superimposed dc discharge current [47]. By comparison of Nyquist plots in Figure 41, it can be said that the differences of the cell impedance are mainly originated from the negative electrode. The spectrum of negative electrodes is comprised of two semi-circles (Figure 41c). The first and second semi-circles of all negative electrodes are located in the frequency region from 6.5 kHz to ~1 Hz and from ~1 Hz to 10 mHz, respectively. Smaller first and second semi-circles are obtained for negative electrodes with higher S_{ext} of carbons. Here, the spectrum of negative electrodes C3, C4 and C5 is very similar. For the case of C1 and C2, both semi-circles are remarkably larger. The observation of two semi-circles in the spectra of negative electrodes was also obtained by other researchers [47,162]. Based on the electrical equivalent circuit of lead-acid batteries [167], the first semi-circle is attributed to the charge-transfer resistance and the double-layer capacitance. However, the processes for the observation of the second semi-circle is so far not understood [168].

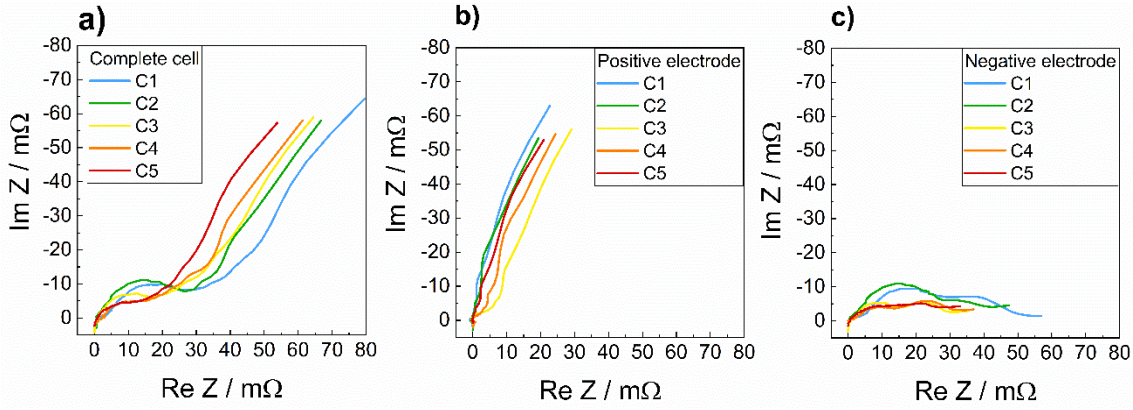

Figure 41: Nyquist plot obtained from the electrochemical impedance spectroscopy executed after the qDCA part of the DCA (EN) test for a) complete cell; b) positive electrode and c) negative electrode. The EIS measurements were performed with a superimposed charge current of $0.5 \cdot I_{20}$.

For further evaluation of the influence of carbon additives, the spectrum of negative electrodes is fitted. Therefore, the relation between high-frequency effects during charging in EIS and dynamic charge acceptance of cells can be compared. Figure 42 shows the chosen equivalent circuit model for the EIS measurements. This equivalent circuit model consists of one semi-circle used for fitting the first semi-circle of the negative electrode spectrum in the frequency range from 2 Hz to 128.5 Hz. This frequency region is known to be related to the electrodeposition and electrooxidation of Pb^{2+} ions [162]. This simplification in the fitting process is performed in order to reduce the distortion of the second semi-circle on the first semi-circle which is determined in this work to be sufficient for evaluating the carbon influence on the DCA. Further, the effects of porosity, which is dominant in the very high-frequency region, are also eliminated.

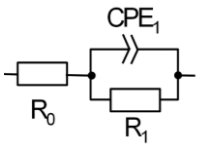

Figure 42: Equivalent circuit model for the electrochemical impedance spectra of negative electrodes.

The equivalent circuit model (Figure 42) includes a resistance R_0 in series to the parallel connection of the constant-phase element (CPE_1) and a resistance R_1. Since the ohmic offset is removed, the resistance R_0 equals to 0. The CPE enables readjusting the compression of the semi-circles by using the parameter ξ_1. An inductive part within the equivalent circuit is not considered since the very high-frequency region is eliminated in the fitting. The formula of the equivalent circuit model for the first semi-circle is:

$$Z = R_0 + \frac{R_1}{1 + [\tau_1 \cdot (j\omega)]} \tag{34}$$

where τ_1, j and ω stand for time constant, imaginary number and angular frequency, correspondingly.

The fit has a constant compression parameter ξ_1=0.6581 for all cells, so that different cells can be compared with each other without having variations in the compression factor. The fitting of the negative electrode spectrum visualized in the Nyquist diagram and Bode plots is shown in the Appendix (Figure A.1). Additionally, the Bode plots of the complete cell, negative electrode and positive electrode are presented in the Appendix (Figure A.2).

The relationship between the fitting parameters of the EIS spectra of negative electrodes and the external surface area of carbon additives is demonstrated in Figure 43. The time constant τ_1 of all negative electrodes is similar and only slightly depending on the carbon additive (Figure 43a). Considering charger-transfer resistance (Figure 43b), negative electrodes having a high external surface area of carbon tend to provide lower resistances. However, no direct correlation can be made to the S_{ext} of carbon. As seen in Figure 43c, a clear increase of capacitance values with respect to the S_{ext} of carbon is observed. Altogether, as the carbon external surface area increases, the resistances decrease, while the capacitance values become higher.

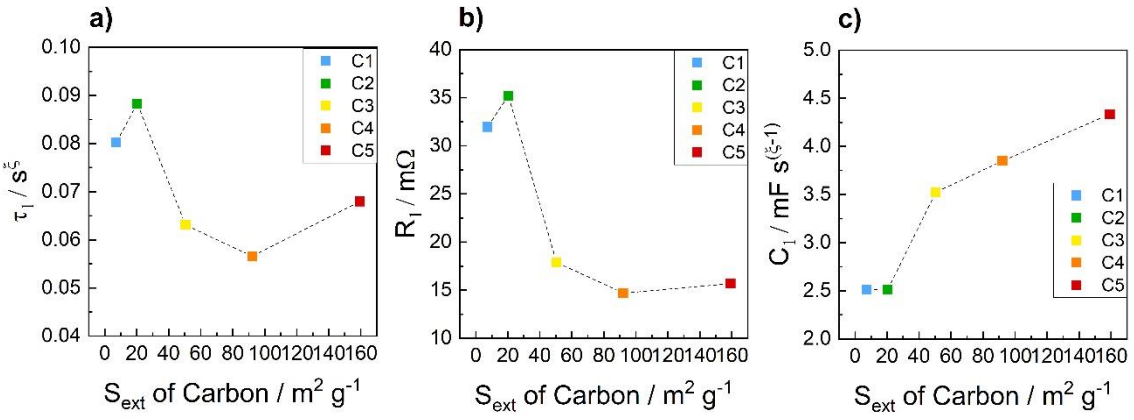

Figure 43: Fitting parameters obtained according to the formula of the equivalent circuit model ((34): a) time constant; b) resistance and c) capacitance.

To establish a general relation of DCA and EIS, the charge acceptance values obtained from the DCA (EN) test as well after the 3 weeks of the Run-in DCA test are plotted with respect to the capacitances obtained from the EIS (Figure 44a-b). Since the EIS measurements were performed after the qDCA test, the SBA test results are not included. According to the obtained results, there seems to be a general trend between EIS and DCA. An almost linear correlation between the charge acceptance and capacitance values is obtained. This linear proportionality can be still maintained even after 3 weeks of run-in drive cycles. It can be said that the EIS might be used to predict the DCA of cells. However, differentiation of short-term cycled cells from Run-in cells cannot be done at this point. Further attention is also expanded to the relationship between the capacitance values obtained from the EIS and CV measurements. As can be seen in Figure 44c, a proportionality between EIS and CV is obtained.

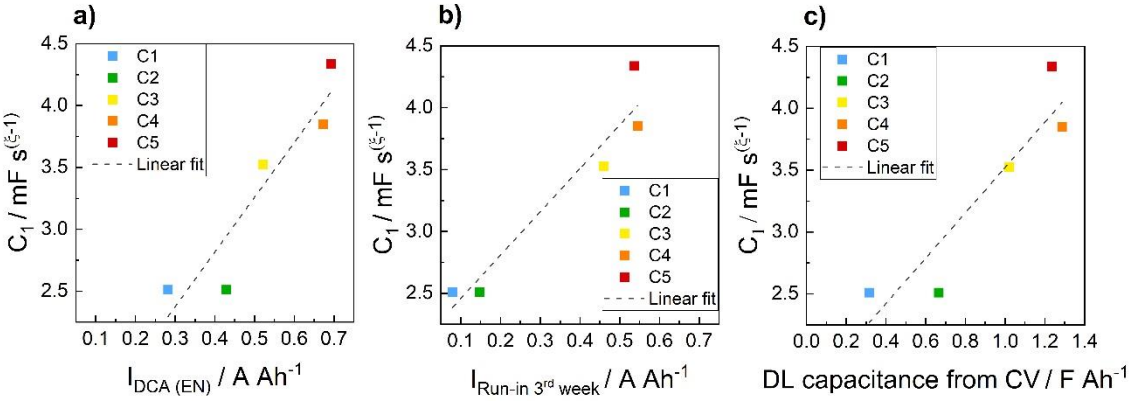

Figure 44: Relationship between capacitance values obtained from the EIS and DCA according to a) DCA (EN) test; b) 3 weeks of Run-in DCA test. c) Correlation between capacitance obtained from the EIS and CV.

As a result of the EIS measurements, the following conclusion can be made. The carbon additive influences the impedance of negative electrodes significantly. The higher the external surface area of the carbon, the higher the capacitance of the first semi-circle. Interestingly, the 3 weeks of the run-in drive cycle does not alter this tendency. An enhancement of the DCA by the greater external surface area of carbon is in line with the increase of the capacitance and the decrease of the resistance. These findings above can be explained by assigning the resistance R_1 to the charge transfer resistance of the main reaction of the NAM (reduction/oxidation of Pb^{2+} ions) and the capacitance C_1 to the respective double-layer capacitance, which is also suggested by other literature [47,162,167]. The additional external surface area introduced by the carbon seems to lower the charge transfer resistance by increasing the electrochemical active surface area for the reduction of Pb^{2+} ions.

3.3 Summary

The goal of this study was to investigate the influence of carbon additives on both short- and long-term DCA tests. For this reason, five different amorphous carbons with a particularly adjusted particle size and thereby differing in specific external surface areas were employed as additives in the negative plates of 2 V, 2.5 Ah lead-acid cells. The S_{ext} of carbons varied between 7.1 $m^2\ g^{-1}$ and 159.3 $m^2\ g^{-1}$, while the d_{part} changed between 27 nm and 633 nm. A similar V_{mic} and S_{BET} of all five carbons were obtained. All lead-carbon (negative) electrodes were prepared by including 2 wt. % carbon additive. A correlation between the S_{ext} of lead-carbon electrodes and carbon additives is established. In the SEM micrographs of the cured lead-carbon electrodes, an agglomeration of the carbon particles was observed for the ones with smaller particle sizes of carbons. According to the XRD measurements, no significant influence of the carbon additives on the diffraction patterns and the crystalline phases of the cured lead-carbon electrodes was found. The 2 V lead-acid cells consisted of one negative electrode and two positive electrodes (2P1N) to limit all cell properties like capacity and charge acceptance by the negative electrode. All cells possessed a 20 h discharge capacity of around 2.5 Ah.

All lead-acid cells were subjected to three different charge acceptance tests, which can be differentiated as short-term (CA test 2 from SBA and DCA from EN) and long-term (Run-in DCA test from Ford) tests. According to the CA test 2, the DCA (EN) and the first 3 weeks of the Run-in DCA test, the cells containing carbons with higher S_{ext} possessed higher DCA. A clear correlation between the DCA and the S_{ext} of carbon was obtained. However, the DCA values above 0.5 A Ah^{-1} showed a limit of this correlation, which was attributed to other aspects that limited the carbon impact, such as agglomeration of small-sized carbon particles. The 4 weeks of the Run-in DCA test executed after 4 weeks of airport parking did not reveal a clear correlation to the previous charge acceptance

tests. This observation was associated with the significant reduction of the recuperation currents to the minimum levels for the poor DCA cells, which occurs due to the Run-in test protocol. Only cells providing a higher charge acceptance can keep a certain DCA. In that case, only differentiation between high and low DCA cells was observed. Therefore, the influence of carbon external surface area in long-term DCA testing can be revealed up to airport parking. Furthermore, the cycling behavior of 2 V cells during the DCA (EN) and Run-in DCA test was found similar to that already known for 12 V lead-acid batteries [74,77]. The cycling behavior in the DCA (EN) test includes an increased charging current during each trip and a reduced charging current after every night for the DCRss part. In case of the Run-in DCA test, a substantial decrease in the recuperation currents after each weekend, stabilized DCA values after airport parking (Run-in effect) and reversibility of the Run-in effect after pre-cycling of laboratory cells. To sum up, the short charge acceptance tests from SBA and EN standards as well as the first 3 weeks of the Run-in DCA test seem to be applicable for carbon additive screening in 2 V cells. As the impact of carbon external surface area cannot be fully obtained after airport parking, testing a higher number of 2 V cells and investigating other parameters of carbon additives such as surface chemistry can be considered to gather further understanding in this topic.

For further understanding of the electrochemical properties of lead-acid cells, CV and EIS measurements were conducted. According to the CV, both HER and DL capacitance of negative electrodes were enhanced via an increase of S_{ext} of carbon. Saturation of the HER currents and the DL capacitances was obtained for electrodes with higher S_{ext}. In case of EIS, based on the fitting of the negative electrode spectrum visualized in the Nyquist diagram, an increase of capacitance and a decrease of charge-transfer resistance values with respect to the S_{ext} of carbon were observed. Considering the ECM for the impedance of negative electrodes, the resistance R_1 was attributed to the charge-transfer reaction of the reduction and oxidation of Pb^{2+} ions, while the capacitance C_1 was related to the double-layer capacitance. Moreover, a clear proportionality between the charge acceptance and capacitance values obtained from EIS was achieved. This correlation was maintained for the DCA (EN) and 3 weeks of the Run-in DCA test.

It should be also mentioned that the correlation between the DCA and the DL capacitance according to CV was already established in a previous study [72]. This dissertation extended this correlation for various charge acceptance tests as well as for the resistance and capacitance values obtained from EIS. These findings suggest that the DCA is strongly influenced by the surface effects introduced by carbon additives. As the electrochemical activity of negative electrodes is significantly affected by the surface effects as well, both CV and EIS methods can be used for carbon additive screening to improve the DCA of batteries.

4 Part 2: Influence of carbon surface chemistry on negative electrodes

The aim of this study is to understand the impact of carbon surface functional groups on the electrochemical properties of lead-carbon electrodes in terms of the hydrogen evolution reaction (HER) activity and the dynamic charge acceptance. To elucidate this effect, commercial activated carbon was chemically modified via different treatment methods to introduce different surface functional groups in the carbon structure. The resulting activated carbons, providing a broad pH range of 2.5 to 11.1, were used as additives in the negative electrodes of 2 V lead-acid cells.

The chapter is divided into three main parts. First, the experimental procedure including preparation and characterization of carbons as well as manufacture and electrical testing of laboratory cells are explained. Second, the chemical and physical properties of carbons as well as the electrochemical activity and the dynamic charge acceptance of cells are presented and discussed. Third, the obtained results and main findings are summarized. Part of the results obtained from this chapter was published in the *Journal of Energy Storage* in December 2021 [169].

4.1 Experimental

This chapter provides the properties and preparation of the carbon materials used in this study. Further, the preparation of negative electrodes as well as the applied electrical tests are explained.

4.1.1 Chemical modification of activated carbons

Commercial activated carbon (Kuraray YP-50F) produced from coconut shell through a physical steam activation was used as received as the starting material for all modifications. In order to obtain carbon materials with acidic and basic surface characteristics, the commercial activated carbon (AC) was modified with different chemical treatment methods.

Basic activated carbons

Pristine AC was modified with ammonia gas at three different temperatures in order to incorporate nitrogen groups and vary its content on the carbon surface. For these three ammonia treatments, around 5 g of pristine activated carbon was placed in an alumina boat which was put into a quartz glass tube of the tubular horizontal furnace (Wisag AG, GERO-tube furnace 70-500/12). Firstly, pristine AC was dried overnight at 100 °C under a flow rate of 10 L h^{-1} of nitrogen (Linde, nitrogen 5.0). Afterwards, the furnace was heated until the desired temperature (200 °C, 500 °C or 700 °C) under nitrogen flow.

After the desired temperature was reached, the atmosphere was changed from nitrogen to ammonia (Linde, ammonia 5.0). The sample was treated with ammonia with a flow rate of 10 L h^{-1} at this temperature for 2 h. Then, the furnace was cooled down to 100 °C under ammonia flow. Finally, at 100 °C, the gas flow was changed from ammonia to nitrogen again and the furnace was cooled down to room temperature under nitrogen flow (10 L h^{-1}). All steps of the furnace treatment were performed with a heating rate of 5 °C min^{-1}. The activated carbons obtained from the ammonia treatments at 200 °C, 500 °C and 700 °C are named as AC-b1, AC-b2 and AC-b4, correspondingly.

In addition to the nitrogen-doped ACs, pristine AC was treated with hydrogen (Linde, hydrogen 5.0) to remove most of the surface oxygen groups. Around 10 g of pristine AC was placed into a changeable atmosphere furnace (MUT Advanced Heating GmbH Jena, CAF 200/200-2200G) and heated to 650 °C with a rate of 20 °C min^{-1} in a flow of hydrogen (0.5 L min^{-1}). The sample was kept at 650 °C for 3 h under a hydrogen atmosphere. Then, the sample was cooled down to room temperature under hydrogen flow. At room temperature, the atmosphere was changed from hydrogen to nitrogen (0.5 L min^{-1}) and the sample was kept at this temperature for an additional 1 h. The activated carbon obtained from the hydrogen treatment is named AC-b3.

It should be noted that gas-phase treatments of carbon with ammonia at high temperatures have been used for nitrogen functionalization by other researchers [139,142]. This is also valid for the hydrogen treatment to remove the surface oxygen groups of carbon [147–149]. The experimental procedure was modified and optimized for the modification of activated carbon used in this work.

Acidic activated carbons

To oxidize the activated carbon with the desired oxygen content, gas- and liquid-phase treatments were performed. Gas-phase oxidation was implemented by using air. On the other hand, liquid phase treatments include hydrogen peroxide and nitric acid with different concentrations. These treatment methods for carbon oxidation have been studied before [130,132,170] and they are optimized in this study to obtain activated carbons with different amounts of oxygen.

For the air treatment, around 7 g of pristine AC was placed in a quartz glass tube of the tubular horizontal furnace (Carbolite 301, Barloworld Scientific). The furnace was heated from room temperature to 350 °C with a rate of 5 °C min^{-1} in a flow of nitrogen (Air Liquide, nitrogen 5.0) with a rate of 0.7 L min^{-1}. The sample was kept at this temperature for 6 h under air atmosphere (Air Liquide, synthetic air 5.0) with a flow rate of 0.5 L min^{-1}. Afterwards, the furnace was cooled down to room temperature under nitrogen flow. The obtained activated carbon from air treatment was named AC-a1.

For the hydrogen peroxide treatment, about 7 g pristine AC and 200 ml of hydrogen peroxide (30 wt. % H_2O_2 in water containing stabilizer, Sigma-Aldrich) were placed in a round-bottom flask. The treatment was performed for 5 h at room temperature. This mixture was filtered and the obtained powder was washed with distilled water until neutral pH. Then, the carbon powder was dried in the oven at 110 °C for 1 h. The received sample was named AC-a2.

Three different nitric acid treatments were performed in order to vary the oxygen content of the ACs. The concentrated nitric acid (65 % HNO_3, pure p.a., POCH) was diluted to 33 % and 20 %. For each nitric acid treatment, around 7 g of pristine AC and 250 ml of nitric acid with the desired concentration (20 %, 33 % and concentrated) were introduced in a round-bottom flask connected to reflux. All treatments were performed at 65 °C and the reflux system was activated during modification time. For 20 % and 33 % nitric acid modifications, the treatment time was 3 h. In case of the concentrated nitric acid treatment, the duration was prolonged to 5 h. After the completion of all treatments, the filtration, washing and drying procedure were the same as the hydrogen peroxide treatment. The carbon powders obtained from 20 %, 33 % and concentrated nitric acid treatments were labeled as AC-a3, AC-a4 and AC-a5, respectively.

Overall, 9 different modified activated carbons including 5 acidic and 4 basic carbons were prepared to study the influence of carbon surface chemistry on the electrochemical properties of the lead-acid cells. The overview of the treatment conditions and types for these activated carbons is shown in Table 4.

Table 4: Overview of the activated carbons used in this study

Material	Treatment type	Temperature (°C)	Duration (h)
AC-b1	NH_3	200	2
AC-b2	NH_3	500	2
AC-b3	H_2	650	3
AC-b4	NH_3	700	2
AC-a1	air	350	6
AC-a2	H_2O_2	25	5
AC-a3	20 % HNO_3	65	3
AC-a4	33 % HNO_3	65	3
AC-a5	conc. HNO_3	65	5

Reference carbon blacks

Two commercial carbon blacks (Lamp black 101 from Orion Engineered Carbons and PBX51 from Cabot Corporation) exhibiting low and high BET surface area were used as benchmark carbons. These two carbon blacks (CB) were named CB-low and CB-high, respectively.

4.1.2 Preparation of negative electrodes and laboratory cells

Negative electrodes

The negative pastes were prepared in the same way as in the investigation of charge acceptance tests in cell-level study (chapter 3.1.2). The only difference is the carbon as well as the water content used in the paste mixture. For the study of basic activated carbons, concentration of 1 wt. % and 2 wt. % carbon was used. In the case of the acidic activated carbons, only 1 wt. % carbon was used in the negative paste mixture. Depending on the carbon concentration in the negative paste, 12 wt. % water for the pastes with 1 wt. % carbon and 14 wt. % water for the 2 wt. % carbon were used.

After the negative paste preparation, the pasting and curing procedure were also kept the same as in chapter 3.1.2. For the carbon surface chemistry study, smaller negative grids having the dimension of 6.7 x 2.9 x 1.2 cm were used. Figure 45 shows a picture of a negative grid, the cured negative and positive electrodes.

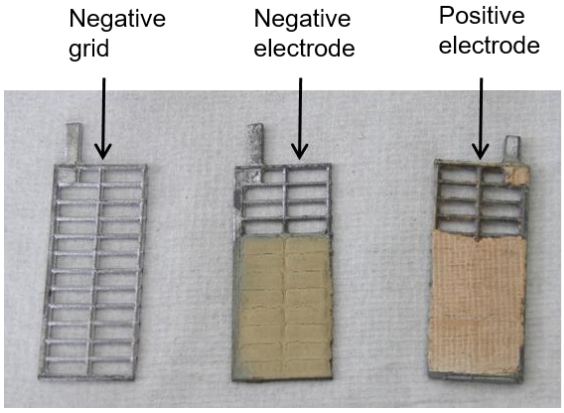

Figure 45: A negative grid, manually pasted negative electrode after curing process and a cured positive electrode.

Laboratory cells

After the negative electrode manufacture, 2 V laboratory cells possessing a 20 h discharge capacity of 1.2 Ah were assembled. Similar to the charge acceptance tests study, the cells are composed of one negative plate, two positive plates and a reversible

hydrogen electrode (RHE, Hydroflex®, Gaskatel Germany). The positive electrodes were again enveloped by polyethylene separators (Daramic® HP™, Daramic LLC). The cell was closed by using parafilm. Figure 46 presents a laboratory cell and the stacking of negative and positive electrodes. In this study, the spacers were again used to decrease the acid volume in the test cells.

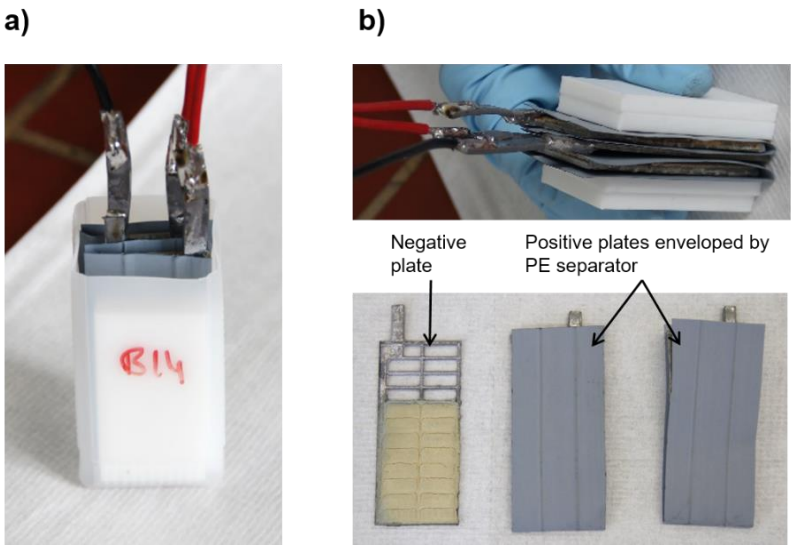

Figure 46: a) 2 V, 1.2 Ah laboratory cell; b) Stacking of plates inside the cell, where a single negative electrode is surrounded by two positive electrodes enveloped by the separator.

The container formation method was used to form the negative and positive electrodes. For the formation, the cells were filled with sulfuric acid with a density of 1.15 g ml^{-1}. The same formation procedure as in chapter 3.1.2 was applied.

4.1.3 Characterization of carbon powders

Elemental analysis

The elemental analysis of carbon powders to determine C, H, N and S content was performed by using the Elementar Vario MICRO analyzer. The oxygen content determination was done by the direct method using a Euro Vector 3018 analyzer.

X-ray photoelectron spectroscopy (XPS)

The XPS technique was used to analyze the surface concentrations of carbon, nitrogen and oxygen. The measurements were performed by Surface Science Instruments S-Probe with detector upgrade. The source of X-ray radiation was monochromatic Al Kα set at 10 kV. The atomic concentrations of carbon, nitrogen and oxygen were calculated from the photoelectron peak areas by using Shirley background subtraction. For the

determination of the type of nitrogen and oxygen groups, the deconvolution of N1s and O1s peaks was implemented. The following binding energies were chosen according to the possible groups in the activated carbons.

For N1s peak:

- Pyridinic-nitrogen: 398.3 eV [142]
- Pyrrolic-nitrogen, pyridonic-nitrogen, amides, amines and lactams: 399.8 eV [139,142,171]
- Quaternary-nitrogen: 401.3 eV [172]
- Pyridine N-oxide: 402.2 eV [139]

For O1s peak:

- C=O in carbonylic and quinone: 531 eV [132,173]
- C=O in ester and anhydrides; C-O-C in ethers; C-OH in phenols and carboxylic: 532.3 eV [132,174,175]
- C-O in ester and anhydrides: 533.5 eV [132,174]
- Carboxyl and chemisorbed oxygen: 535.3 eV [174,175]

Nitrogen sorption

The textural properties of activated carbons were determined by nitrogen sorption at 77 K using Autosorb iQ, Quantachrome Instruments. Prior to the measurements, the samples were degassed overnight at 180 °C. The BET surface area was calculated according to the Brunauer, Emmett and Teller method [156]. The total pore volume (V_T) was determined from the amount of nitrogen adsorbed at a relative pressure of p/p_0 = 0.96. The micropore volume (V_{DR}) and the average micropore size (L_0) were calculated by applying the Dubinin-Radushkevich (DR) and Stoeckli equations [176] correspondingly. The difference between V_T and V_{DR} was used to calculate the mesopore volume (V_{mes}).

pH

For the determination of surface acidity/basicity of activated carbons, pH measurements were followed. Around 0.2 g of the carbon powder was dispersed in 10 ml of double-distilled water. The dispersion was performed by using an ultrasonic finger for 10 min at a power of 80 W. Then, the prepared dispersion was kept until it sediments. After the sedimentation, the pH of carbons was measured by using a portable pH meter (pH 315i handheld meter) equipped with a pH electrode (InLab Basics pH 0-14, Mettler Toledo). For both acidic and basic carbon powders, a three-point calibration method was used.

Electrical conductivity

Similar to the published work [177], the electrical resistance of carbon powders was estimated by a two-point technique using Keithley SourceMeter Model 2400. The carbon samples poured in the PTFE cylinder were compressed by two copper plates. The compression pressure of 1400 N was applied for the measurements. The dc electrical conductivity, σ, was calculated according to the following formula

$$\sigma = \frac{h}{R \cdot A} \tag{35}$$

where h is the sample height in m, R is the electrical resistance in Ω and A is the area of the plunger in m^2.

Figure 47 illustrates the measurement setup as well as carbon powder placed in the PTFE cylinder.

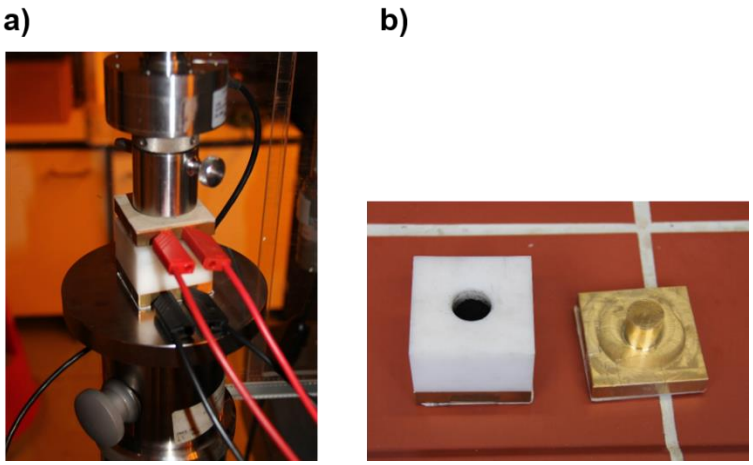

Figure 47: a) The setup of an electrical conductivity measurement; b) Carbon powder poured in the PTFE cylinder.

It should be mentioned that all characterization methods described above were conducted once after the optimization of the technique. Therefore, the corresponding results are from a single measurement.

4.1.4 Electrical and electrochemical testing of laboratory cells

After the container formation of the cells, the acid density of the freshly formed cells was adjusted to 1.28 g ml^{-1}. Then, the initial capacity test was executed on the cells. Afterwards, the fully charged cells were subjected to cyclic voltammetry measurements. Last, the DCA (EN) test was performed on lead-acid cells to evaluate their rechargeability. For the study of 1 wt. % carbon, 36 cells were prepared, which includes three cells for each carbon type (9 modified ACs, 1 pristine AC and 2 reference CBs).

Regarding the study of 2 wt. % carbon, 21 cells were prepared, which consists of three cells per carbon type (4 modified basic ACs, 1 pristine AC and 2 reference CBs). Additionally, 3 cells containing a negative electrode without any carbon additive were manufactured.

Initial capacity test

This test includes three times the determination of the discharge capacity at 20 h rate. The fully charged cells were first discharged with 20 h rate current and then they were charged with a constant voltage of 2.67 V with a current limitation of $5 \cdot I_{20}$. This procedure was repeated three times.

Cyclic voltammetry

The electrochemical activity of negative electrodes in terms of the HER and double-layer (DL) capacitance was analyzed via cyclic voltammetry measurements at 100 % SoC, The CVs were performed with a Scienlab battery tester (Keysight, Germany). For the determination of the HER activity, the fully charged negative electrodes were cycled between the potential of $Pb/PbSO_4$ redox couple reaction at -0.38 V vs. RHE and -0.88 V vs. RHE. Regarding the DL capacitance determination, the negative electrodes were cycled between -0.46 V vs. RHE and -0.56 V vs. RHE. All CV measurements were carried out with a scan rate of 10 mV s^{-1}.

Dynamic charge acceptance (EN 50342-6:2015)

The influence of carbon surface chemistry on the charging behavior of negative electrodes was determined by DCA (EN) test. According to the EN, the DCA test consists of three main parts which are the pre-cycling, the qDCA and the dynamic charge acceptance real word stop/start driving cycle DCRss. Since the initial capacity test was performed directly after the cell formation, the pre-cycling part of the DCA test was excluded. Only, one C_{20} determination was followed and then the qDCA and DCRss parts were executed on the cells. The same procedure of the qDCA and DCRss parts was done as described in chapter 3.1.4.

4.2 Result and Discussion

This chapter covers the results of various characterization techniques for carbon materials to determine their physical and chemical properties. Moreover, the results obtained from the cyclic voltammetry and dynamic charge acceptance test for lead-acid cells are explained and discussed.

4.2.1 Properties of modified activated carbons

4.2.1.1 Elemental composition

In order to determine the elemental composition of the modified carbons, elemental analysis via thermal decomposition was performed. The results from the elemental analysis of the acidic and basic ACs are summarized in Table 5. The carbons are listed according to the oxygen content in descending order. Pristine AC consists of mainly oxygen functional groups in the bulk (2 wt. %). It can be seen that with the help of acidic treatments, the amount of oxygen in the bulk can be substantially altered. Gas-phase treatment with air originates a modest increase in the oxygen content (3.4 wt. % O for AC-a1). On the other hand, the liquid phase treatments (H_2O_2 and HNO_3) of AC result in a remarkable increase in the oxygen content (from AC-a2 to AC-a5). The H_2O_2 treatment promotes the oxygen content to 4.9 wt. % (AC-a2). Further liquid phase treatments with HNO_3 increase the amount of oxygen stepwise, which can be attributed to the change of concentration of HNO_3. A raise in HNO_3 concentration enables incorporating more oxygen groups in the carbon structure, which is already a known effect from other publications [153,178,179]. Treatment with 20 % HNO_3, 33 % HNO_3 and concentrated HNO_3 promote the oxygen content of AC to 7.3 wt. %, 11.2 wt. % and 13.8 wt. %, respectively. Further, a noticeable increase of the nitrogen content (around 1 wt. % N) is also observed for the AC-a3, AC-a4 and AC-a5, which is due to the HNO_3 treatment [119,180].

Concerning the basic treatments of AC, the change of both nitrogen and oxygen content is observed. Gas-phase treatments with NH_3 introduce nitrogen groups in the carbon structure. An increase of treatment temperature tends to enhance the nitrogen content of AC, which is also observed by other studies [126,137–139,142]. Chemical modifications applied at 200 °C (AC-b1) and 500 °C (AC-b2) increase the oxygen content to 0.7 wt. %. The ammonia treatment performed at 700 °C (AC-b4) results in oxygen content of 2 wt. %. Apart from the incorporation of nitrogen, the oxygen content of activated carbons decreases. This can be attributed to the fact that oxygen groups can be replaced by nitrogen-containing groups via ammonia treatment at elevated temperatures [142,181]. In the case of the treatment with H_2 (AC-b3), the oxygen content of AC is significantly reduced (0.8 wt. %). It is known that high temperatures treatments under inert atmosphere or hydrogen can remove the oxygen functional groups up to some extent [132,147–149].

In general, elemental analysis results show that the oxygen content of AC can be varied via gas- (air) and liquid-phase (H_2O_2 and HNO_3) oxidative treatments. Basic treatments performed under NH_3 and H_2 result in a reduction of oxygen content. Through ammonia treatments, the nitrogen groups can be also incorporated into the AC. As a result of

several chemical modifications, a series of AC with different oxygen content is developed. The oxygen content of activated carbon decreases in the order from AC-a5 to AC-b4.

Table 5: Elemental analysis of the pristine and modified activated carbons (the table was adapted from Bozkaya et al. [169]).

Material	Treatment type	C (wt. %)	N (wt. %)	O (wt. %)	H (wt. %)
AC-a5	conc. HNO_3	86.2	1.1	13.8	1.1
AC-a4	33 % HNO_3	88.8	1.2	11.2	0.9
AC-a3	20 % HNO_3	92.7	1.0	7.3	0.5
AC-a2	H_2O_2	95.1	< 0.3	4.9	0.5
AC-a1	air	96.6	< 0.3	3.4	0.7
AC	-	96.5	< 0.3	2.0	0.6
AC-b1	NH_3	96.5	0.7	1.6	0.7
AC-b2	NH_3	97.2	0.7	1.1	0.5
AC-b3	H_2	98.2	< 0.3	0.8	0.6
AC-b4	NH_3	96.6	2.0	0.6	0.5

4.2.1.2 Elemental composition of carbon surface

XPS measurements were performed in order to determine the composition of the surface functional groups in the modified ACs. In contrast to elemental analysis, which measures the total elemental composition accounting for surface and bulk, XPS is used to analyze the surface chemistry of carbons. The atomic percentage of C, N and O obtained from XPS is shown in Table 6. By oxidative treatments of AC, the atomic concentrations of oxygen increase from 5 at. % for AC to 5.6 at. % for AC-a1, 7.6 at. % for AC-a2, 9.9 at. % for AC-a3, 11.6 at. % for AC-a4 and 13.6 at. % for AC-a5. The oxygen content determined by elemental analysis (Table 5) and XPS (Table 6) is similar for highly oxidized ACs (AC-a4 and AC-a5). On the other side, the oxygen content on the surface of AC-a1 and AC-a2 is much higher than that of the bulk material. This observation can be attributed to the treatment conditions. Since the modifications with air, H_2O_2 and low concentration of HNO_3 increase the oxygen content moderately, mainly the surface of AC might be oxidized rather than the bulk. Further, all nitric acid treatments introduce low concentrations of nitrogen on the surface of AC, which changes between 0.5 at. % N and 1.3 at. % N. Similar results were also obtained in the bulk of ACs determined by elemental analysis.

In the case of the gas-phase ammonia treatments, the surface nitrogen content is increased to 1.2 at. % for AC-b1, 1.7 at. % for AC-b2 and 2.5 at. % for AC-b4. It seems

that an increase in treatment temperature increases the composition of nitrogen-containing groups stepwise. It is known that ammonia decomposes to free radicals (nitrogen, atomic hydrogen, NH_2, NH) when the modification of carbon materials is performed at elevated temperatures. These free radicals react with the possible sites of the carbon, which forms nitrogen-containing functional groups [182,183]. Surface oxygen groups can be replaced by such free radicals at high temperatures, which leads to a decrease in the oxygen content of the ACs. As seen in Table 6, the composition of oxygen reduces from 5.1 at. % to 3.4 at. % for AC-b1, 1.5 at. % for AC-b2 and 0.9 at. % for AC-b4. Higher amount of nitrogen incorporation leads to a higher loss of surface oxygen content. In case of the hydrogen treatment of AC, the surface oxygen groups are mainly removed, in which the concentration of oxygen is 1.1 at. % for AC-b3. It should be also mentioned that the concentrations of nitrogen and oxygen on the surface of all modified basic ACs provide much higher values in comparison to that of bulk material determined via elemental analysis. This phenomenon is expected since all basic treatments include gas-phase, which alters mainly the surface of the carbon materials. It is also known that the external surface of activated carbons is generally more oxidized than the inner surface due to the microporosity of activated carbons [184].

Table 6: XPS of the pristine and modified activated carbons (the table was adapted from Bozkaya et al. [169]).

Material	C (at. %)	N (at. %)	O (at. %)
AC-a5	86.4	1.0	13.6
AC-a4	87.1	1.3	11.6
AC-a3	89.6	0.5	9.9
AC-a2	92.4	nd	7.6
AC-a1	94.4	nd	5.6
AC	94.9	nd	5.1
AC-b1	95.4	1.2	3.4
AC-b2	96.8	1.7	1.5
AC-b3	98.9	nd	1.1
AC-b4	96.6	2.5	0.9

In order to obtain further information about the type of oxygen and nitrogen functional groups on the surface of ACs, the O1s, C1s and N1s spectra of the selected ACs were analyzed. Figure 48 presents the deconvolution of the O1s spectra of pristine AC and all modified acidic ACs. The O1s peak consists of four types of subpeaks which are named carbonylic, phenolic, ester and chemisorbed oxygen. The carbonylic peak at mean binding energy of 531 eV presents the C=O in carbonylic and quinone structures. The

phenolic peak located at mean binding energy of 532.3 eV stands for C-OH in phenols, C-O in ethers, C=O in ester and anhydrides and carboxylic. The ester peak positioned at mean binding energy of 533.5 eV shows the C-O in esters and anhydrides. The peak at mean binding energy of 535.3 eV presents chemisorbed water and oxygen on the carbon surface. This chemisorbed peak can be also associated with carboxylic groups but according to the published studies [132,174,185,186], the contribution of carboxylic groups was not taken into account due to the low intensity of the peak. The discussion from now on is done based on the name of the peaks written in Figure 48 to avoid excessive wording in the text. Furthermore, the right-hand side of Figure 48 shows the relative abundance of each oxygen type. According to these values, percentages of the respective oxygen groups are calculated based on the total oxygen amount obtained from XPS, which is shown in Table 7.

As seen in Figure 48, pristine AC consists of mainly phenolic type of oxygen groups followed by ester and carbonylic groups. The contribution of the last peak, chemisorbed oxygen, is relatively low (Table 7). After the air treatment of AC (AC-a1), the concentration of the phenolic group decreases and that of both ester and carbonylic groups increase. In the case of all liquid-phase treated samples (from AC-a2 to AC-a5), the concentration of phenolic groups substantially increase. Stronger oxidative treatment of AC clearly promotes the formation of the phenolic group. It has been shown in another study that gas-phase oxidative treatment of AC originates higher amounts of oxygen groups in the form of quinone and carbonyl groups, while liquid-phase treatments mainly increase the concentration of carboxylic and phenolic groups [132]. Since the binding energy of the carbonylic peak represents also quinone groups and that of the phenolic peak represents carboxylic groups, the results of this study fit perfectly with the published work [132]. Moreover, liquid-phase treatments introduce both carbonylic and ester groups, in which the effect is not as pronounced as the phenolic group.

When the methods used for surface oxidation of carbon materials are reviewed, the most commonly preferred oxidants are concentrated or diluted nitric acid and air [119]. Especially, oxidation with nitric acid has been considered as an efficient process since the change of treatment conditions such as acid concentration, treatment duration and temperature can alter the type and amount of surface oxides [121,125–127,131]. In this work, an increase in nitric acid concentration (from AC-a3 to AC-a5), not only introduce higher amounts of oxygen groups on the carbon surface but also change the type of surface oxides in a systematic way. The concentration of both phenolic and ester groups increased stepwise from AC-a3 to AC-a5. The concentration of carbonylic group slightly increased for AC-a5 in comparison to AC-a3 and AC-a4.

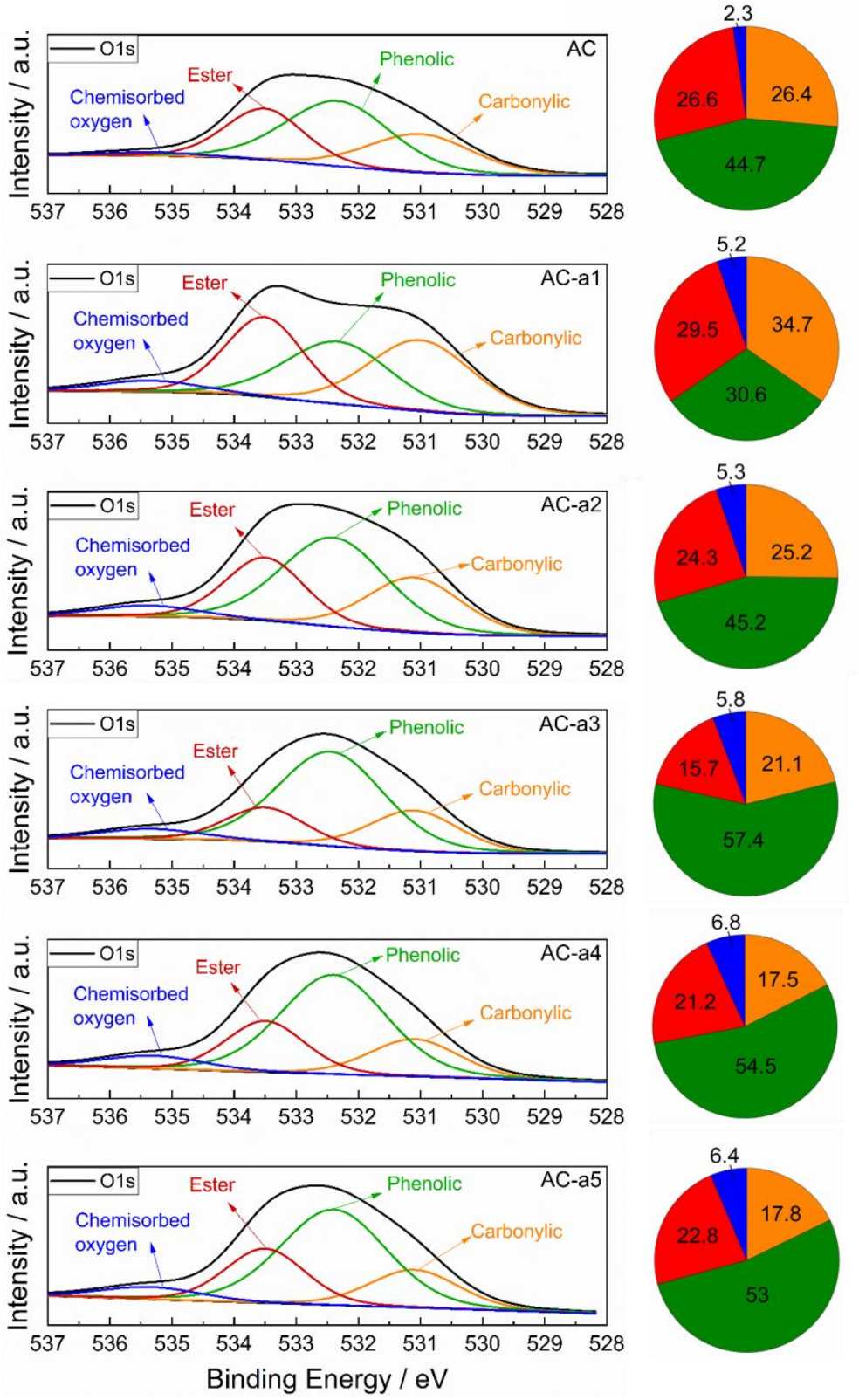

Figure 48: Deconvoluted O1s spectra of pristine AC and acidic carbon samples and the pie charts presenting a relative abundance of the respective oxygen-containing functional groups.

Table 7: The contribution of the relevant oxygen functional groups according to Figure 48, values given in % of the total oxygen amount

Material	Type of surface oxygen groups (%)				O_{total} (at. %)
	Carbonylic	Phenolic	Ester	Chemisorbed	
AC	1.3	2.3	1.4	0.1	5.1
AC-a1	1.9	1.7	1.7	0.3	5.6
AC-a2	1.9	3.4	1.8	0.4	7.6
AC-a3	2.1	5.7	1.6	0.6	9.9
AC-a4	2.0	6.3	2.5	0.8	11.6
AC-a5	2.4	7.2	3.1	0.9	13.6

Figure 49 shows the deconvolution of N1s spectra of basic ACs treated with ammonia. The N1s peak is comprised of four types of subpeaks which are pyridinic (N6), pyrrolic and pyridonic (N5) as well as amides, amines and lactams (NC), quaternary (NQ) and pyridine N-oxide (NX). These peaks are located at mean binding energy of 398.3 eV, 399.8 eV, 401.3 eV and 402.2 eV, respectively. The configuration of these nitrogen atoms on the carbon surface can be found in Figure 16. The right-hand side of Figure 49 presents the relative abundance of each nitrogen group type. Additionally, the concentrations of the relevant nitrogen groups, calculated based on the total nitrogen amount obtained from XPS, are shown in Table 8. It can be clearly seen that an increase of surface nitrogen content by higher treatment temperature (from AC-b1 to AC-b4), the relative abundance of pyridinic-N and quaternary-N increases while that of pyrrolic-N, pyridonic-N, amides, amines and lactams decrease. Considering the pyridine N-oxide, no clear trend is observed. The percentage of this nitrogen group type based on the total amount of nitrogen is equal for all samples (Table 8).

It is stated that ammonia treatments with higher temperatures incorporate more stable nitrogen functional groups. At a temperature of 200 °C, a reaction between ammonia and oxygen groups on the carbon surface leads to the generation of amides, amines, imides and nitriles [142]. In the case of temperatures above 250 °C, the incorporation of nitrogen into the carbon double bond can occur but only to a small extent [126]. Pevida and the coworkers modified commercial activated carbon with ammonia at 600 °C, 700 °C and 800 °C. Their XPS results show that an increase in modification temperature from 600 °C to 700 °C not only increases the total nitrogen content on the carbon surface but also introduces a higher concentration of pyridinic-N and pyrrolic-N. However, for the case of treatment at 800 °C, a decrease in total nitrogen content as well as a reduction in concentration of pyridinic-N and pyrrolic-N are observed in comparison to the sample treated at 700 °C [142]. Further study also states that NC groups can be converted into pyrrolic-N and pyridinic-N by high-temperature treatments [137]. In this thesis, the

treatment of AC at 200 °C (AC-b1) leads to the highest concentration of amides and amines (NC). Moreover, an increase in treatment temperature promotes both total nitrogen content and the concentration of pyridinic-N, which correlates with the published work [142]. In contrast to the published work, the concentration of pyrrolic (N5) and NC decreases in this work. This contradiction might be attributed to the peak fitting of the N1s spectra since only two peaks were taken into account. These peaks are pyridinic-N at 398.3 eV and pyrrolic-N at 400 eV [142]. Therefore, the contribution of quaternary-N and pyridine N-oxide is not taken into account in that published work.

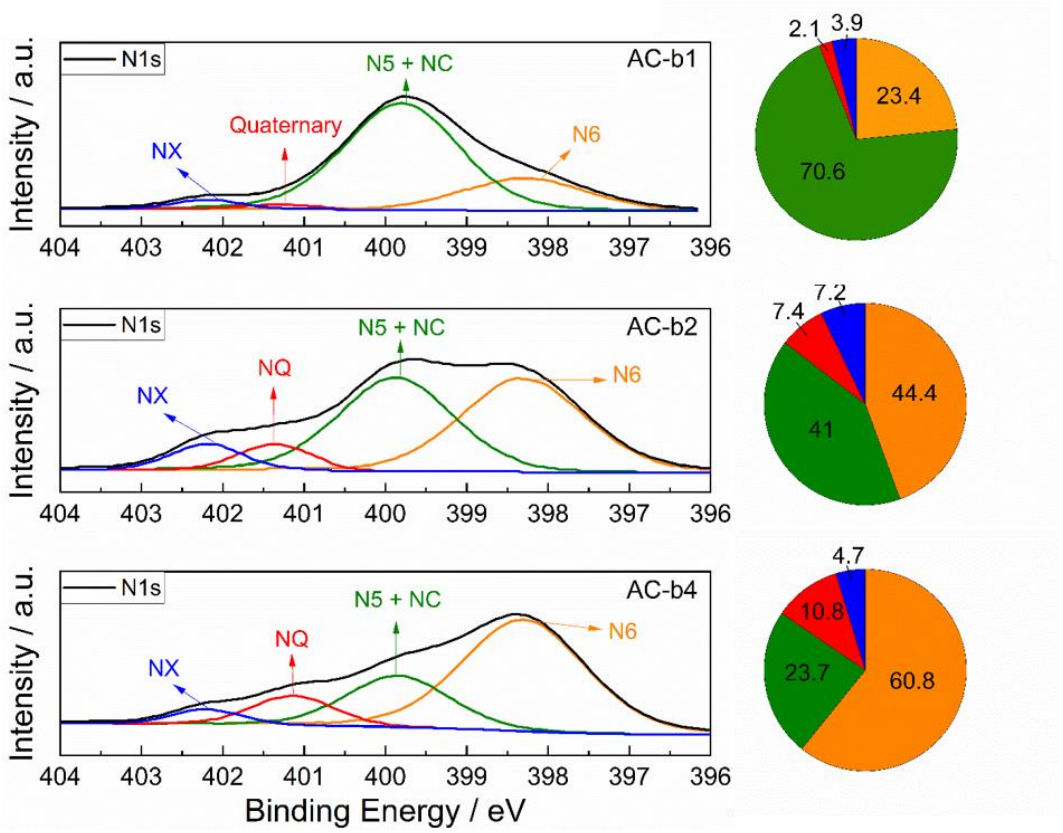

Figure 49: Deconvoluted N1s spectra of basic carbons treated with ammonia and the pie charts presenting a relative abundance of the respective nitrogen-containing functional groups (the figure was reproduced from Bozkaya et al. [169]).

Table 8: The contribution of the relevant nitrogen functional groups according to Figure 49, values given in % of the total nitrogen amount

Material	Type of surface nitrogen groups (%)				N_{total} (at. %)
	N6	N5 + NC	NQ	NX	
AC-b1	0.3	0.8	~0	0.1	1.2
AC-b2	0.8	0.7	0.1	0.1	1.7
AC-b4	1.5	0.6	0.3	0.1	2.5

4.2.1.3 Textural properties

The textural parameters of all activated carbons as well as reference carbon blacks, characterized by nitrogen sorption, are shown in Table 9. All ACs possess a specific surface area (S_{BET}) of 1530-1770 $m^2\ g^{-1}$. In comparison to pristine AC, AC-a1 and AC-a2 provide slightly higher S_{BET}, total pore volume (V_T) and micropore volume (V_{DR}). Furthermore, a reduction in the mesopore volume (V_{meso}) is observed. In the case of AC-a3, AC-a4 and AC-a5, lower S_{BET}, V_T, V_{DR} and V_{meso} are obtained after the modification of AC with nitric acid. The only exception is observed for AC-a3, which exhibits similar micropore volume as pristine AC. Moreover, all oxidized ACs provide a larger average pore diameter (L_0) than pristine AC. The maximum change in the specific surface area of the oxidized activated carbon is 9 %, which is observed for AC-a5 and AC-a1. It is reported that the textural properties of activated carbon upon oxidation might change due to the widening of pores, formation of new pores or opening inaccessible micropores [132,187]. It has been reported that the gas-phase oxidations such as O_2 and N_2O increase the S_{BET}, V_T, V_{DR}, V_{meso} and L_0 [132], which matches with the textural properties of the air treated AC (AC-a1) except for the decrease in mesopore volume for AC-a1. In the case of the oxidized carbons via liquid-phase, the variation of textural properties is only negligible and it also depends on the treatment conditions such as acid concentration [119,132]. In this work, two types of liquid-phase oxidation methods, H_2O_2 and HNO_3, provide different trends in terms of structural properties. The treatment via H_2O_2 results in comparable textural parameters as pristine AC. However, the change in textural parameters of ACs is more pronounced for the nitric acid treated ones. This obtained result can be attributed to the fact that HNO_3 is a stronger oxidizing agent than H_2O_2, which can be also observed by the introduction of higher content of oxygen groups in the carbon structure. The presence of higher content of oxygen groups might lead to blockage of micropores and collapse of pore walls, which is also observed in [22,149]. Moreover, the decrease in all types of pore volume and the increase in average pore diameter for nitric acid treated samples suggest the destruction of pore walls.

Considering all modified basic ACs, an increase in S_{BET}, V_T, V_{DR} and L_0 is obtained, while V_{meso} decreases. The increase of specific surface area as well as the micropore volume of ACs might be attributed to partial gasification of the carbon in the presence of ammonia [149] and hydrogen [147] at higher temperatures. It has been stated that the free radicals formed during ammonia treatment might lead to an increase in porosity [138] via the creation of new micropores [182] or enlargement of existing pores [142,182,188].

The obtained results claim that the textural properties of the modified ACs are in a comparable range with pristine AC. In general, the specific surface area and the total pore volume of AC are increased via both gas-phase acidic and basic treatments. Among them, the maximum variation in the S_{BET} and V_T is 10 % and 4 %, respectively. On the

other hand, the liquid-phase acidic treatments except for the modification with H_2O_2 decrease the specific surface area and the total pore volume of AC. In comparison to pristine AC, the highest change of S_{BET} and V_T is 9 % and 8 %, correspondingly. The variation in the textural parameters of the modified ACs is inevitable due to the functionalization of the carbon structure itself. Still, such variations in this study are relatively small.

In the case of the reference CBs used in the negative plates of lead-acid cells, CB-low and CB-high possess a S_{BET} of 30 $m^2\ g^{-1}$ and 1520 $m^2\ g^{-1}$, correspondingly. CB-low provides a rather small V_T which can be considered as non-microporous. On the other side, CB-high has a much larger V_T, which suggests that it is mainly comprised of mesopores.

Table 9: Textural parameters if all ACs and reference CBs obtained from N_2 sorption measurements (the table was adapted from Bozkaya et al. [169]).

Material	S_{BET} ($m^2\ g^{-1}$)	V_T ($cm^3\ g^{-1}$)	V_{DR} ($cm^3\ g^{-1}$)	V_{mes} ($cm^3\ g^{-1}$)	L_0 (nm)
AC-a5	1530	0.720	0.593	0.127	1.20
AC-a4	1570	0.736	0.602	0.134	1.17
AC-a3	1590	0.734	0.607	0.127	1.25
AC-a2	1700	0.792	0.648	0.144	1.21
AC-a1	1740	0.806	0.667	0.139	1.25
AC	1690	0.786	0.606	0.180	1.09
AC-b1	1750	0.820	0.682	0.138	1.26
AC-b2	1770	0.819	0.679	0.140	1.26
AC-b3	1740	0.814	0.681	0.133	1.29
AC-b4	1760	0.818	0.673	0.145	1.23
CB-low	30	0.036	0.012	0.024	1.30
CB-high	1520	1.476	0.599	0.877	1.31

4.2.1.4 Surface polarity (pH)

In order to determine the influence of chemical treatments on the acidic and basic character, pH measurements were conducted. Figure 50 presents the pH of all ACs with respect to the surface oxygen content obtained via XPS. It can be seen that an increase of oxygen content of carbon decreases the pH of ACs. However, the correlation between pH and surface oxygen content is slightly different for the oxidized ACs and ammonia and hydrogen-treated ACs. The pristine AC has a pH of 9.5. The increase in ammonia treatment temperature promotes the pH of carbon to 10.1 for AC-b1, 10.6 for AC-b2 and

11 for AC-b4. The removal of surface oxygen groups of AC by hydrogen treatment remarkably increases the pH to 11.1 for AC-b3. In case of the oxidized ACs, the increase in surface oxygen content decreases the pH of carbon more significantly. In comparison to pristine AC, air and hydrogen peroxide treatments decrease the pH of carbon to 7.4 for AC-a1 and 6.4 for AC-a2, respectively. Stronger oxidative treatments performed with nitric acid decrease the pH even further. The pH of AC-a3, AC-a4 and AC-a5 is 4.6, 3.5 and 2.9, correspondingly.

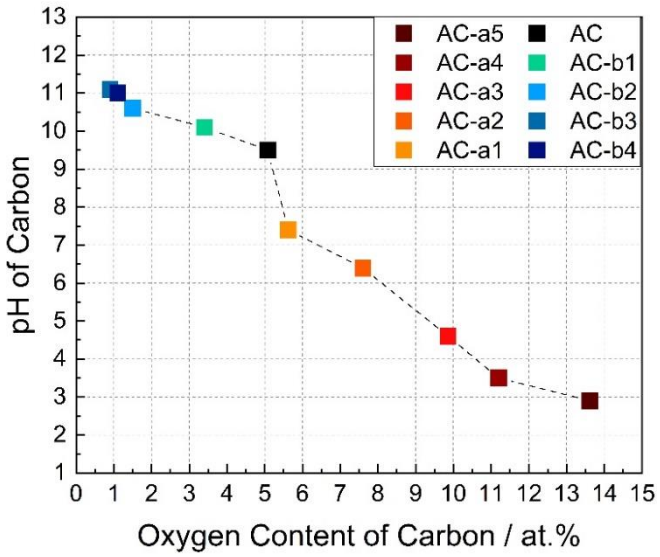

Figure 50: Relationship between surface oxygen content obtained from XPS and pH of ACs (the figure was adapted from Bozkaya et al. [169]).

All these observations are in line with the expectations based on the literature. As explained in the theoretical part (chapter 2.4.2), the acidic or basic behavior of the activated carbon surface is related to the surface functional groups and the delocalized electrons of the carbon structure [120]. The basic character of the activated carbon surface is mainly associated with the nitrogen-containing functional groups and delocalized π-electrons which attract protons [124,134,149]. The basicity of the activated carbon surface is increased via nitrogen and hydrogen treatments. Through ammonia treatment, the acidic surface groups are replaced by basic nitrogen functional groups as shown in the results obtained from XPS and pH. The increased surface basicity by ammonia treatment has been also presented by some researchers [126,181,185]. The presence of pyridinic-N seems to be responsible for the basic character of nitrogen-doped ACs [189], which fits the results obtained from the N1s deconvolution (Figure 49). On the other side, hydrogen treatment removes most of the surface oxygen groups. Previous studies have also shown that the removal of surface oxygen groups at elevated temperatures enhances the basicity of the carbon surface [121,190]. Regarding the acidic behavior of activated carbon surface, it mainly arises from the presence of oxygen-containing surface groups [121,122]. In this thesis, all oxidative treatments make

the carbon surface more acidic compared to pristine AC. As the surface oxygen content increases, the incorporation of the types of oxygen groups such as phenolic and carboxylic acid increases (Table 7). According to the published studies, carboxylic acid and phenolic groups enhance the surface acidity of ACs [134,191], which correlates with the results obtained from this thesis.

4.2.1.5 Electrical conductivity

The electrical resistance of the AC powders was determined as described in chapter 4.1.3. The measurements of acidic and basic carbons were performed at different times. For each set of measurements, the reference measurements were done by using pristine AC. Figure 51 presents the electrical conductivity of pristine AC and acidic ACs with respect to the oxygen content of ACs obtained from XPS. As expected, the conductivity values are higher for the measurements executed with a higher pressure. For both measurements under a pressure of 1400 N and 800 N, the relationship between the surface oxygen content and conductivity of ACs is the same. The higher oxygen content of carbon tends to decrease the electrical conductivity of the activated carbon. The electrical conductivity of AC-a3 is only slightly lower than the AC-a2 despite the remarkable difference in surface oxygen content. This observation might be attributed to the presence of nitrogen groups for the nitric acid treated samples as shown in Table 6. It is known that nitrogen groups might improve the electrical conductivity of the carbon structure [192,193]. The combined effect of nitrogen and oxygen surface groups on the electrical conductivity might be the reason for the slight difference between the conductivity of AC-a3 and AC-a2. When ACs modified with nitric acid (AC-a3, AC-a4 and AC-a5) are compared, there is almost a linear correlation between the electrical conductivity and oxygen content of carbons.

Figure 52a presents the electrical conductivity of pristine AC and basic ACs with respect to the surface oxygen content. It is observed that the conductivity values of pristine AC measured at different time differ for both 800 N and 1400 N. The conductivity values of pristine AC in Figure 51 is almost doubled in comparison to the values in Figure 52 even if the measurements were conducted in the same way. The origin of this quantitative difference might be due to a two-point measurement setup. Therefore, the contact resistances, e.g. due to the oxygen layer on top of the copper plates, cannot be avoided. Still, the conductivity of carbon powders can be qualitatively compared. As seen in Figure 52a, lowering the oxygen content of AC seems to enhance the electrical conductivity values. However, the relationship is not straightforward. Although the surface oxygen content of AC-b3 and AC-b4 is very similar, there is a significant difference in the conductivity values, which might be due to the presence of nitrogen groups in the AC-b4 sample.

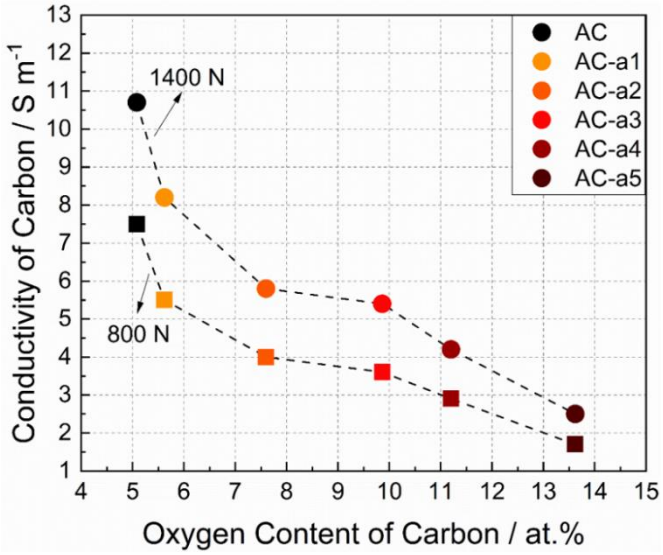

Figure 51: Relationship between surface oxygen content obtained from XPS and electrical conductivity of pristine AC and acidic ACs. The electrical conductivity measurements were performed by applying a pressure of 800 N and 1400 N.

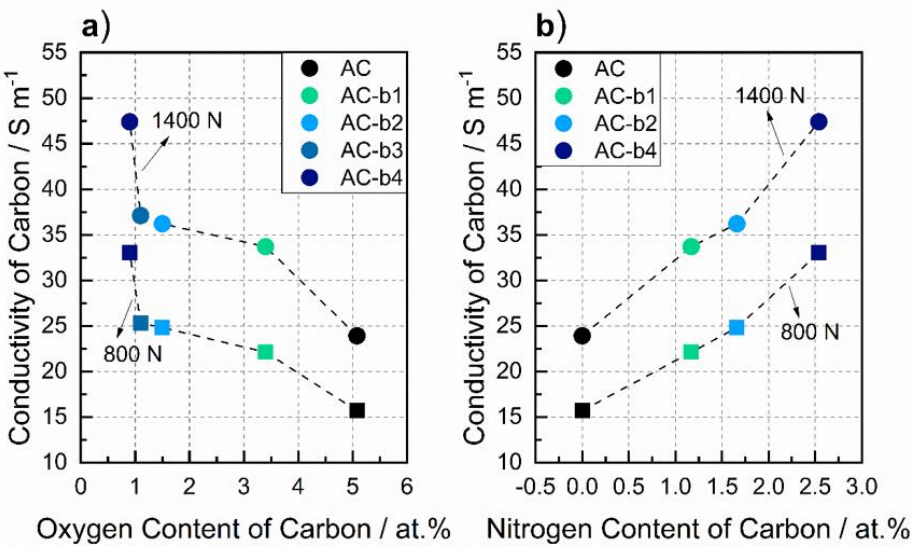

Figure 52: a) Relationship between surface oxygen content and electrical conductivity of pristine AC and basic ACs, b) Relationship between surface nitrogen content and electrical conductivity of pristine AC and ammonia-treated ACs.

Moreover, the relationship between the electrical conductivity and surface nitrogen content for ammonia-treated ACs and pristine AC is shown in Figure 52b. There is almost a linear relationship between the surface nitrogen content and conductivity. This enhancement of electrical conductivity values might be related to the incorporation of quaternary-N groups via ammonia treatment. Due to the positively charged nitrogen in the quaternary-N, the electron transfer through carbon might be enhanced [22]. As shown in the deconvolution of the N1s spectra obtained from XPS (Figure 49), the

relative abundance of quaternary-N groups increases stepwise as the surface nitrogen content increases.

As a result, the electrical conductivity of acidic carbon decreases with incorporation of higher oxygen content in the carbon structure. On the other hand, the inclusion of nitrogen groups improves the electrical conductivity of ACs. Since the nitrogen groups are mainly incorporated in the carbon structure by replacing the oxygen groups, the detrimental effect of oxygen groups shall be also considered in this manner.

4.2.2 Electrochemical activity of lead-carbon electrodes

To understand the impact of carbon surface chemistry on the electrochemical properties of lead-carbon electrodes, the electrochemical activity of the negative electrodes was investigated via cyclic voltammetry measurements. The focus of these measurements is the HER activity as well as the DL capacitance of the negative electrodes, which is shown and discussed in the following paragraphs.

4.2.2.1 Influence of carbon pH

The cyclic voltammograms of negative electrodes (one cell per NAM variant) containing 1 wt. % acidic and basic ACs are presented in Figure 53. The voltammograms represent the 10^{th} cycle whereby all current values are normalized to the 20 h discharge capacity of the respective negative electrode. The current-potential profile of negative electrodes can be explained as follows. The negative electrodes are charged in the voltage scans from -0.38 V to -0.88 V vs. RHE resulting in cathodic currents. At the reversal direction from -0.88 V to -0.38 V vs. RHE, the negative electrodes are discharged and therefore anodic current values are obtained. The reduction and oxidation of Pb to $PbSO_4$ is observed at around -0.4 V vs. RHE. At more negative polarization, the HER starts to dominate the current generation at potential values smaller than -0.7 V vs. RHE.

As seen in Figure 53, the HER activity of negative electrodes is affected by the surface chemistry of the carbon additives. In order to have a closer look into this, the HER currents at -0.85 V vs. RHE are plotted against the pH of activated carbons (Figure 54). Oxidative treatments of AC suppress the HER activity of the negative electrodes. On the other hand, the HER activity is significantly increased via ammonia and hydrogen treatments of AC. In general, higher surface basicity of carbon accelerates the HER but the influence of carbon pH on the HER seems to differ for acidic and basic carbons. Considering the oxidized carbons (from AC-a5 to AC-a1), there is almost a linear relationship between carbon pH and the HER currents of negative electrodes. An increase in pH of carbon from 2.9 to 7.4 promotes the HER currents by more than factor 3. In case of basic carbons (from pristine AC to AC-b4), the increased surface basicity

from 9.5 to 11 results in a remarkable change in the HER activity. The HER current for AC-b4 is almost five times higher than that of the AC electrode.

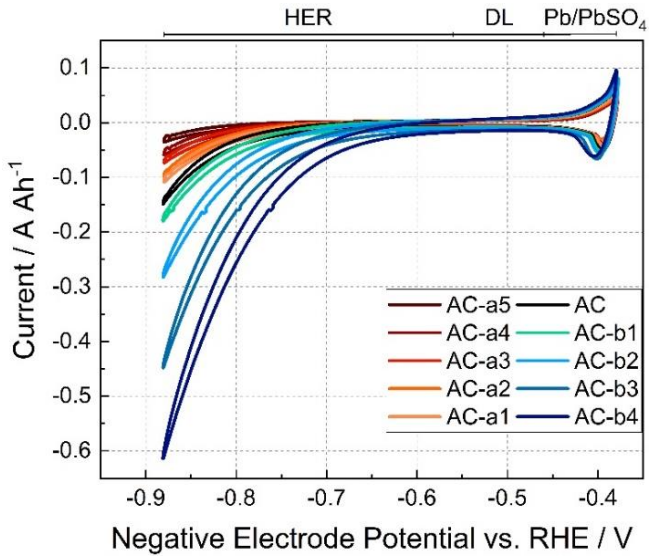

Figure 53: Current-potential relationship of fully-charged negative electrodes, including 1 wt. % acidic and basic activated carbons, at a scan rate of 10 mV s^{-1} obtained from the cyclic voltammetry test (the figure was adapted from Bozkaya et al. [169]).

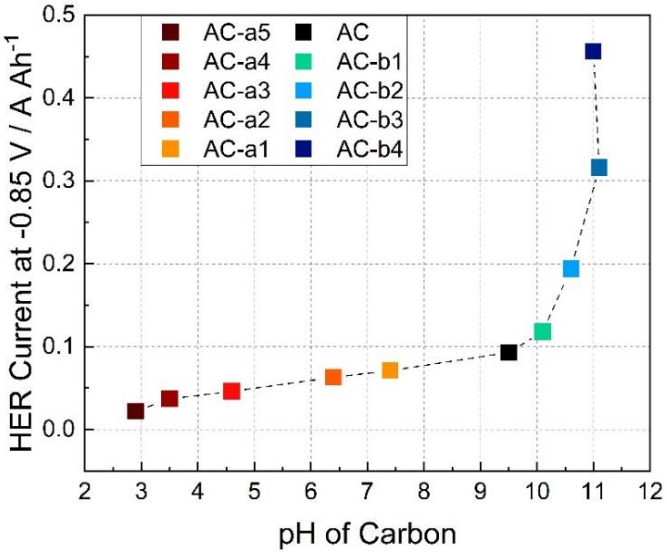

Figure 54: Relationship between the HER currents of negative electrodes with 1 wt. % ACs and pH of carbons (the figure was adapted from Bozkaya et al. [169]).

Although oxygen-containing carbon surface groups are known to increase the electrocatalytic activity of carbon´s surface [119], a decrease in the HER of lead-carbon electrodes via oxidized ACs is observed. A similar trend was also obtained by another study, in which the oxidized carbon blacks were used as additives in the negative plates

of lead-acid batteries [118]. The decreased activity of the HER might be attributed to the interaction of the carbon surface with other paste components such as lignosulfonate. The acidic functionalities might be passivated by the adsorption of lignosulfonate. Another explanation for the reduction of the HER might be due to the acidic groups being the active sites for electrodeposition of lead. Wang et al. [101] found out that the acidic functional groups on the AC surface are promoting the lead electrodeposition leading to an inhibition of the HER in lead-carbon batteries. Moreover, the decreased electrical conductivity of the acidic ACs, originating from the detrimental effect of oxygen groups, might be also a reason for the decreased HER activity.

Considering the nitrogen-doped and hydrogen-treated carbons, the enhanced HER might be originated from the improved rate of proton adsorption on the carbon surface via higher surface basicity. Furthermore, this increased activity might result from the enhanced electrical conductivity of carbons for the basic ACs (as previously shown in Figure 52), which might lead to an improved electron transfer through the carbon surface. Among the nitrogen-doped carbons, the enhanced HER activity might be explained by the presence of pyridinic-N groups, as the relative abundance of pyridinic-N increases in the following order AC-b1 < AC-b2 < AC-b4 (Figure 49). Pyridinic-N seems to improve the HER to the highest extent, which might be due to providing more adsorption sites for hydrogen [194,195]. On the contrary, pyrrolic-N might be the reason for the diminished HER affinity from AC-b4 to AC-b1. Pyrrolic-N is known to provide an easier formation of bonds between nitrogen and hydrogen, which have a very high binding energy. Therefore, the formation of hydrogen molecules can be hindered [196]. In case of the hydrogen-treated carbon (AC-b3), the increased HER activity might be attributed to the delocalization of the π-electrons in the graphene layers [148], which could generate active sites for the adsorption of hydrogen.

For understanding the effect of carbon surface functional groups on the non-faradaic processes, the DL capacitance of the negative electrodes was also investigated. The current-potential profile of the negative electrodes with acidic and basic ACs is shown in Figure 55. All negative electrodes were cycled between -0.46 V and -0.56 V vs. RHE, which is associated with the potential window between HER and $Pb/PbSO_4$. The voltammograms represent the 10^{th} cycle whereby all current values are normalized to the 20 h discharge capacity of the corresponding negative electrode. From the first look, differences in the curvature at higher negative potentials can be realized, which is a result of the HER current contribution. Probably due to the oxygen reduction reaction, a cathodic offset current of around -0.002 A Ah^{-1} is observed.

The DL capacitance of the negative electrodes is calculated by taking the difference between forward and backward scans according to equation 3. The obtained DL capacitance values were shown in Figure 56. In comparison to a negative electrode with

pristine AC, the DL capacitance is lower for all acidic AC-containing electrodes. On the other hand, all negative electrodes with basic ACs show and enhanced DL capacitance. Here, the only exception is observed for the AC-b1, which shows almost the same capacitance value as AC.

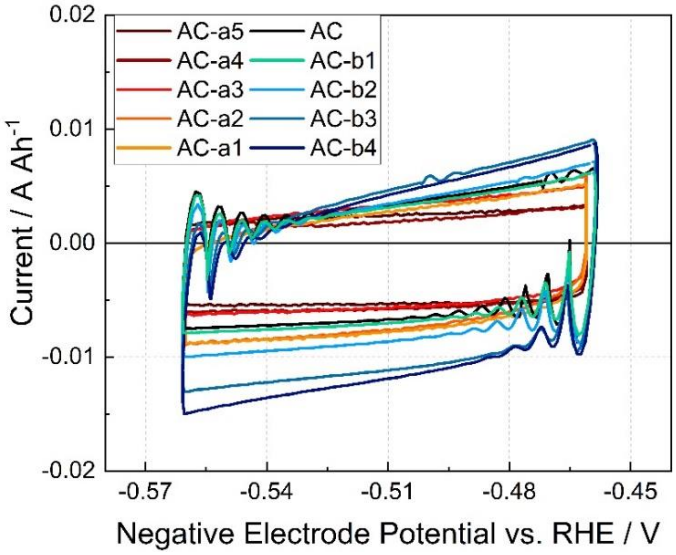

Figure 55: Current-potential relationship of fully-charged negative electrodes, containing 1 wt. % acidic and basic activated carbons, in the double-layer region at a scan rate of 10 mV s^{-1} obtained from the cyclic voltammetry test (the figure was adapted from Bozkaya et al. [169]).

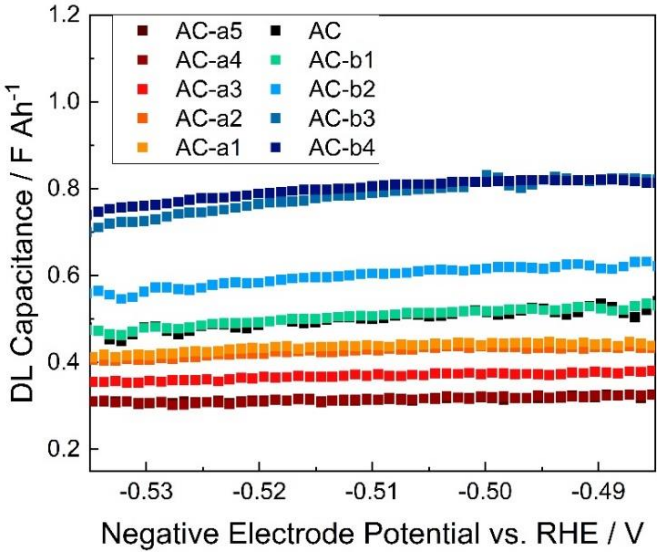

Figure 56: Differential double-layer capacitance of negative electrodes of each negative electrode in Figure 55 (the figure was adapted from Bozkaya et al. [169]).

The DL capacitances at -0.51 V vs. RHE against the pH of activated carbons are presented in Figure 57. The increased surface basicity of activated carbon improves the

DL capacitance of the lead-carbon electrodes. This observation might be associated with the enhanced electronic charge density of the carbon leading to further ion adsorption from the electrolyte. Another reason for this increased DL capacitance might be due to the contribution of the additional pseudocapacitance provided by alkaline carbons. In case of electrodes with nitrogen-doped ACs (AC-b1, AC-b2 and AC-b4), an increase in the DL capacitance from AC-b1 to AC-b4 might be associated with increased amounts of pyridinic-N and quaternary-N in the carbon structure (Figure 49). It is known that pyridinic-N promotes pseudocapacitive reactions, while quaternary-N enhances the electron transfer [21,197,198]. Considering the electrode with hydrogen-treated AC, an increased electrical conductivity of carbon due to the delocalization of the π-electrons in the graphene layers might be the explanation for the superior DL capacitance of AC-b3.

The surface oxygen groups of carbons are known to increase the DL capacitance of electrodes in supercapacitor applications [199,200]. However, for lead-carbon electrodes in this work, the DL capacitance is clearly diminished by using oxidized ACs. As observed also for the HER activities of the oxidized AC-containing electrodes, this phenomenon can be attributed to the interaction between lignosulfonate and carbon as well as to the acidic surface groups being the active sites of lead electrodeposition.

When Figure 54 and Figure 57 are compared, carbon pH affects the DL capacitance and the HER activities of the lead-carbon electrodes in a similar way. The influence of carbon pH on the DL capacitance values is much more significant for electrodes with basic ACs in comparison to the ones with acidic ACs.

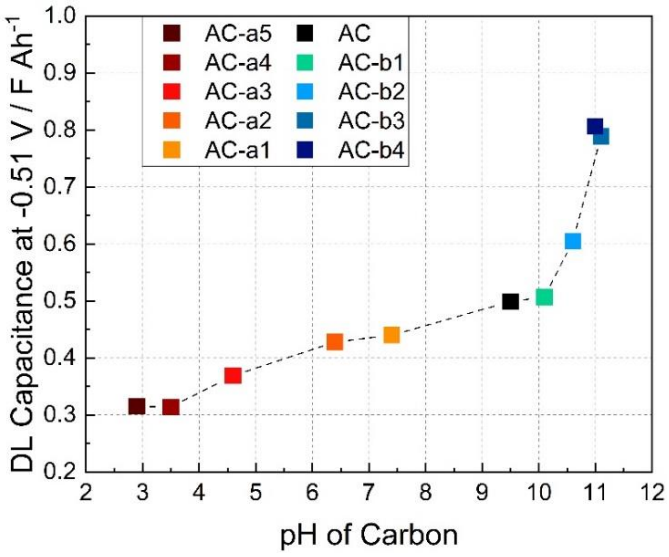

Figure 57: Relationship between the differential double-layer capacitance of negative electrodes and pH of carbons (the figure was adapted from Bozkaya et al. [169]).

4.2.2.2 Influence of carbon content

In order to compare the effect of carbon content and carbon surface chemistry on the electrochemical activity of the negative electrodes, negative electrodes containing 1 wt. % and 2 wt. % carbon were compared in terms of the HER activity and the DL capacitance. Additionally, special attention is given to the comparison of the AC additives with reference carbon blacks which are commercially used as additives in the lead-acid battery industry.

Figure 58 shows the current-potential profile of the lead-carbon electrodes with 1 wt. % and 2 wt. % carbon additives as well as a negative electrode without any carbon additive. As expected, the lowest HER activity is obtained for the electrode without any carbon additive (w/o C). As carbon is introduced as an additive in the negative plates, the activity towards HER is promoted for both CB- and AC-containing electrodes. When the CB- and AC-containing electrodes are compared, the HER activity is increasing in the following order: CB-low < CB-high < pristine AC < basic ACs. The difference between CB electrodes obviously results from the specific BET surface area of CBs (Table 9). As compared to CB-high, the increased HER activity of AC can be attributed to both the BET surface area and the type of carbon itself. As the 1 wt. % (Figure 58a) and 2 wt. % carbons (Figure 58b) are compared, the order of the HER activities of the negative electrodes are almost the same. To have a closer look into this, the relationship between the HER currents at -0.85 V vs. RHE and the pH of the ACs are analyzed. As seen in Figure 58c, not only 2 wt. % but also 1 wt. % AC-containing cells possess higher HER activities as the carbon pH increases. Moreover, doubling the carbon content in the negative electrodes increases the HER currents by two times. This observation suggests the direct contribution of the carbon´s surface to the electrochemical active surface area of the negative electrodes.

Besides HER activity, DL capacitance of the lead-carbon electrodes was also investigated via CV measurements. The current-potential profile of the negative electrodes with 1 wt. % and 2 wt. % carbon additives in the DL potential window is shown in Figure 59. The lowest DL capacitances are obtained by the negative electrodes without any carbon additive and the one containing CB with lower BET surface area. Incorporation of a higher specific surface area of carbon additive (CB-high and AC series) enhances the DL capacitance of the lead-carbon electrodes. To see the influence of carbon content clearly, the DL capacitance values determined at -0.52 V are plotted with respect to the pH of ACs (Figure 59c). Similar to results obtained from the HER activities, both 1 wt. % and 2 wt. % AC containing cell provide the same tendency in the DL capacitances with respect to the carbon pH.

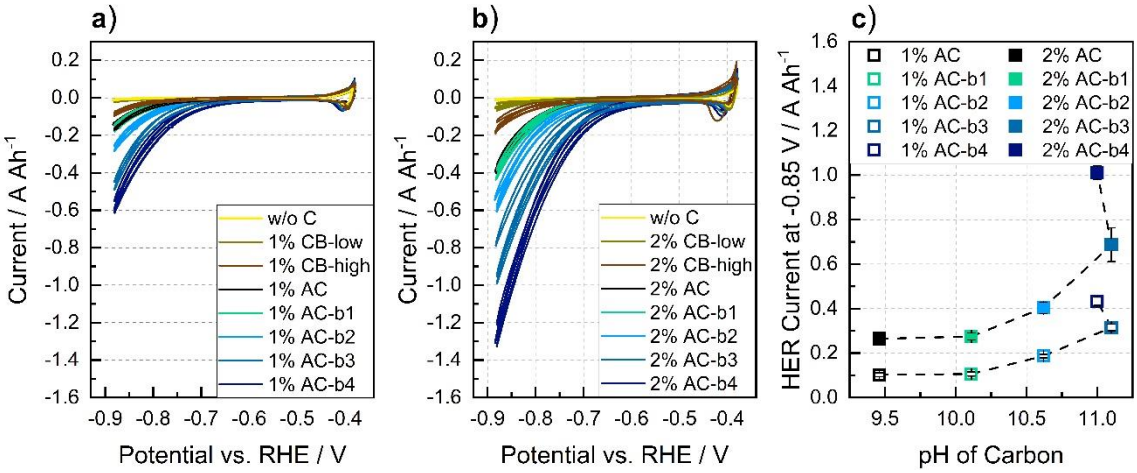

Figure 58: Current-potential relationship of fully-charged negative electrodes including a) 1 % carbon; b) 2 % carbon. c) Relationship between the HER currents of negative electrodes and pH of carbons for both 1 % and 2 % carbon-containing cells. Negative electrodes without any carbon additive (w/o C) are included in the first two graphs as references. In total, three cells per NAM variation were tested (the figure was reproduced from Bozkaya et al. [169]).

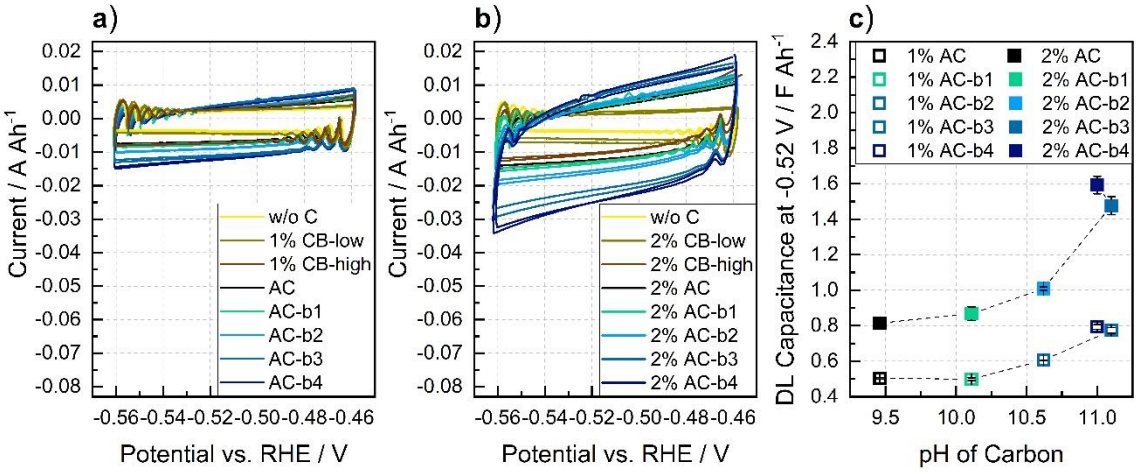

Figure 59: Current-potential relationship of fully-charged negative electrodes in the double-layer region including a) 1 % carbon; b) 2 % carbon and c) Relationship between the HER currents of negative electrodes and pH of carbons for both 1 % and 2 % carbon-containing cells. Negative electrodes without any carbon additive (w/o C) are included in the first two graphs as references. In total, two cells per NAM variation were tested (the figure was reproduced from Bozkaya et al. [169]).

By gathering the results, it was observed that the increased electrochemical activity of the lead-carbon electrodes via higher carbon pH and higher carbon amount is much more pronounced regarding HER as compared to the DL capacitance. For instance, the HER current for AC-b4 is more than three times higher than that of the AC electrodes for both 1 wt. % and 2 wt. % cells (Figure 58c). Considering the DL capacitance, the

capacitance with AC-b4 is double that with AC for 2 wt. % cells (Figure 59c). This capacitance increase by AC-b4 as compared to AC is even further reduced for 1 wt. % cells. This observation suggests that the HER mainly occurs on the carbon surface. On the other hand, the DL charging takes place both on lead and carbon surfaces.

4.2.3 Dynamic charge acceptance of lead-carbon electrodes

The impact of carbon surface chemistry on the recharge-ability of lead-carbon electrodes is investigated via the dynamic charge acceptance test according to the EN specification. The DCA is determined after charge history at 80 % SoC (I_c), after discharge history at 90 % SoC (I_d) and during a simulated real-world drive cycle at 80 % SoC (I_r). Afterwards, the final DCA (I_{DCA}) is calculated (equation 31).

4.2.3.1 Influence of carbon pH

The dynamic charge acceptance for cells containing 1 % acidic and basic activated carbons is presented in Figure 60. In case of the charge acceptance after charge history (I_c), an increase in carbon pH enhances the charge-ability of the negative electrodes (Figure 60a). This enhancement is especially dominant for basic ACs (from pristine AC to AC-b4), in which the charge acceptance is increased by more than 50 % (1 % AC and 1 % AC-b4 is 0.28 A Ah^{-1} and 0.37 A Ah^{-1}, respectively). For electrodes with oxidized ACs (from AC-a1 to AC-a5), only minor differences in the I_c values are observed. After discharge history (I_d), higher pH of carbon additives improves the charge acceptance as well (Figure 60b). Considering cells with basic ACs, I_d is slightly improved by carbons with higher surface basicity (1.20 A Ah^{-1} for AC and 1.25 A Ah^{-1} for AC-b4). A saturation in case of change currents higher than 1.20 A Ah^{-1} is observed. Regarding the cells including acidic ACs, the I_d is remarkably increased via higher carbon pH (1.12 A Ah^{-1} for AC-a5 and 1.22 A Ah^{-1} for AC-a1). In terms of the charge acceptance during simulated stop/start drive cycles (I_r), electrodes containing basic ACs also provide higher charge acceptance in comparison to the ones with acidic ACs (Figure 60c). Here, the influence of carbon pH is not as obvious as in the other parts, which might originate from a saturation effect for high charge currents. Among the cells with the oxidized ACs, similar I_d values are obtained, where the only exception is observed for AC-a4. As shown in Figure 60d, the DCA of cells (I_{DCA}) is increased by using AC additives with higher surface basicity. The impact of carbon pH on the DCA is much more significant for the basic AC-containing cells.

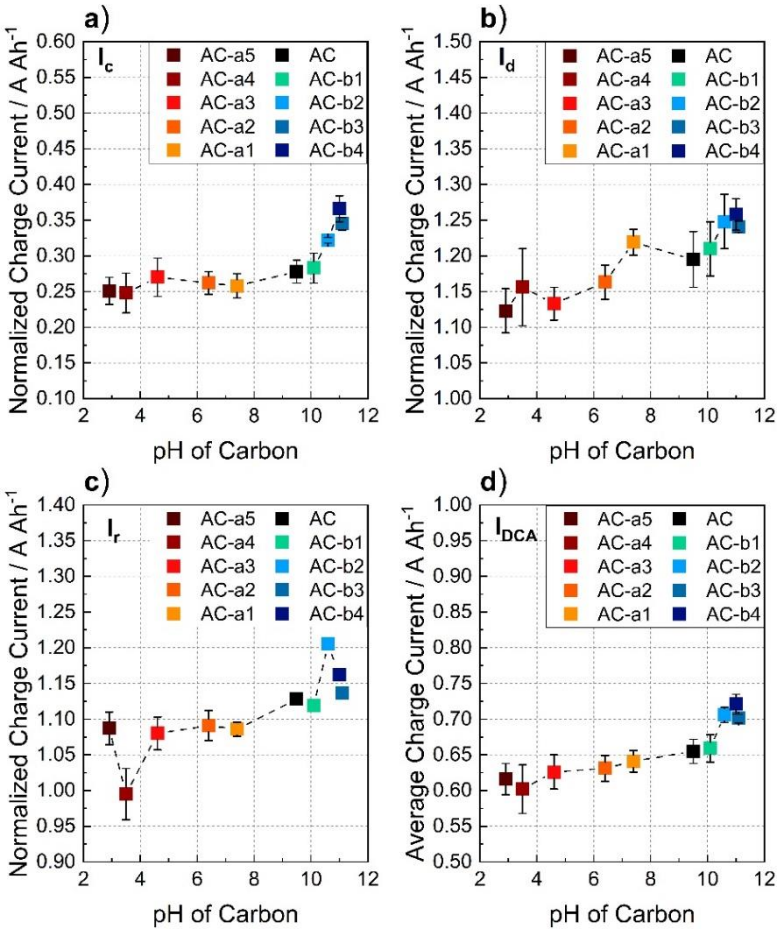

Figure 60: Relationship between carbon pH and normalized charge currents of cells containing 1 wt. % acidic and basic ACs a) after charge history (I_c); b) after discharge history (I_d); c) during one week simulated Start-Stop drive cycle (I_r). d) Correlation between carbon pH and the DCA of cells (I_{DCA}).

Based on the findings above, the history of cells plays an important role in the impact of carbon surface chemistry on charging currents of lead-acid cells. Moreover, the influence of carbon pH on the DCA is different for the cells with acidic and basic ACs. The charge acceptance after charge history (I_c) and discharge history (I_d) is particularly improved via greater surface basicity of carbon. The improvement in I_c is much more remarkable for electrodes containing basic ACs, whereas the enhancement in I_d is more pronounced for the cells with acidic ACs. In case of I_r, no clear relation to the carbon pH can be obtained. The reason for this observation might be due to a limitation of the charge current in case of I_d and I_r. Due to the high electrochemical activity of activated carbons in comparison to carbon blacks, as previously shown in Figure 58 and Figure 59, negative electrodes containing AC additives provide already superior charge currents. Therefore, a further improvement by increased carbon pH may be limited by other battery components (e.g. battery plugs and grid design) rather than the negative active material. Another reason might be related to the structural differences of the negative electrodes after charge and

discharge history. After charge history, much larger $PbSO_4$ crystals are expected to be present in the negative electrode as compared to after discharge history. Thus, the main charge reaction ($PbSO_4$ to Pb reduction) might be improved stronger in case of charge history by using more conductive carbon additives such as AC-b3 and AC-b4 (Figure 52). The reduction of Pb^{2+} ions might be enhanced due to the higher electron transfer rate from carbon to the adsorbed Pb^{2+} ions.

Further attention is given to the understanding of the relationship between the electrochemical activity of the negative electrodes and the DCA. It is crucial to determine how much of the DCA improvement is resulted from the contribution of the HER currents as well as the DL capacitance. To address this issue, the DCA values are plotted with respect to the HER current and the DL capacitance obtained from the CV measurements (Figure 61). The HER current values of the negative electrodes, presented in Figure 61a, are determined at -0.7 V vs. RHE, at which the negative electrode polarization occurs during the charge pulses at around 2.5 V in the DCA test. To find out the contribution of the HER currents, the CV of the most active (AC-b4) and the least active (AC-a5) is compared. The HER currents of AC-b4 and AC-a5 are 64 mA Ah^{-1} and 6 mA Ah^{-1}, respectively. On the other hand, the difference between the DCA of these cells is around 100 mA Ah^{-1}, which is almost double as compared to the difference in the HER current. Therefore, HER can only explain a maximum of 50 % of the DCA improvement. Besides that, the CV measurements were performed at 100 % SoC. In case of PSoC, such as in the DCA test, the HER generated on the negative electrode at -0.7 V vs. RHE is expected to be even further diminished.

The same aspect is also investigated in terms of the contribution of the DL charging. It is suggested that the microporous carbon materials with higher specific surface area can provide a capacitive contribution during the charge and discharge events of electrodes leading to an increase of the current rates [7,12]. Due to the high specific surface area of ACs in this work, the impact of the activity on negative electrodes in the DL region is examined. Figure 61b presents the correlation between the DCA and the DL capacitance determined at -0.51 V vs. RHE according to the CV measurements. When the DL capacitance of AC-b4 and AC-a5 is compared, a difference of around 0.5 F Ah^{-1} is observed. This difference in the DL capacitance generates a maximum charge of $Q = C \cdot \Delta U = 150$ mAs Ah^{-1}, taking into account a negative electrode polarization by 0.3 V. This value 0.3 V is the difference between the negative electrode potential at the charge pulse and the electrode´s equilibrium potential. Considering 10 s charge pulses in the qDCA part for the determination of the average charge currents (I_c and I_d), a maximum charge current of 15 mA Ah^{-1} can be delivered via the DL capacitance. Since the DCA difference between AC-b4 and AC-a5 is around 100 mA Ah^{-1}, the capacitive current obtained in the DL region has a negligible contribution to the DCA.

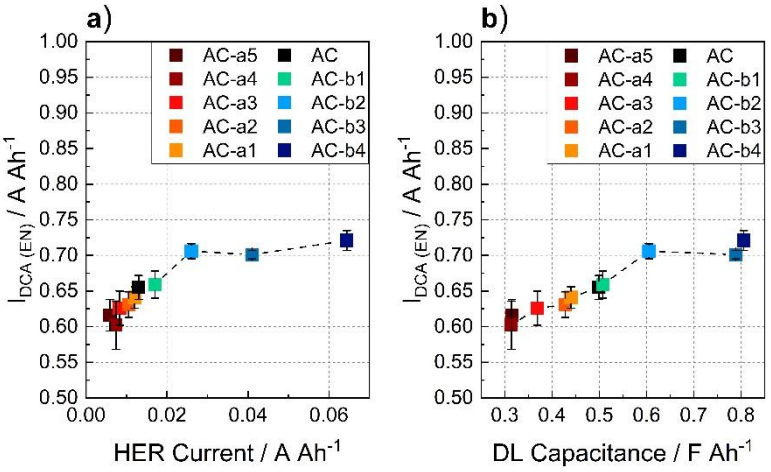

Figure 61: The relationship between DCA and a) the HER current determined at -0.7 V vs. RHE from Figure 53; b) the DL capacitance determined at -0.51 V vs. RHE from Figure 56.

4.2.3.2 Influence of carbon content

For the comparison between the impact of carbon content and that of carbon surface chemistry, the DCA of negative electrodes including two different amounts of basic ACs is examined. The investigation is focused only on the basic ACs, as the surface chemistry has the highest effect in this case. It shall be investigated whether the DCA can be further improved by doubling the content of highly active carbons.

Figure 62 presents the charge acceptance of the negative electrodes containing 1 % and 2 % basic AC additives. It should be mentioned that the results of the 1 % basic ACs are the same as in Figure 60 and they are additionally shown again to evaluate the results of 2 % basic ACs. As seen in Figure 62a-d, 1 % and 2 % carbon-containing electrodes show almost the same trend in the average charging currents (I_c, I_d and I_r) as well as the final DCA (I_{DCA}). The only exception is obtained for I_r of 1 % AC-b2, which possesses the highest charging current. It seems that not only the increase of the carbon pH but also the higher carbon content in the negative electrodes particularly promotes the charge acceptance. For instance, I_{DCA} of AC cells is increased from 0.66 A Ah^{-1} to 0.75 A Ah^{-1} by doubling the carbon amount (Figure 62d). Besides that, the dynamic charge acceptance of 0.72 A Ah^{-1} is reached by using 1 % AC-b4.

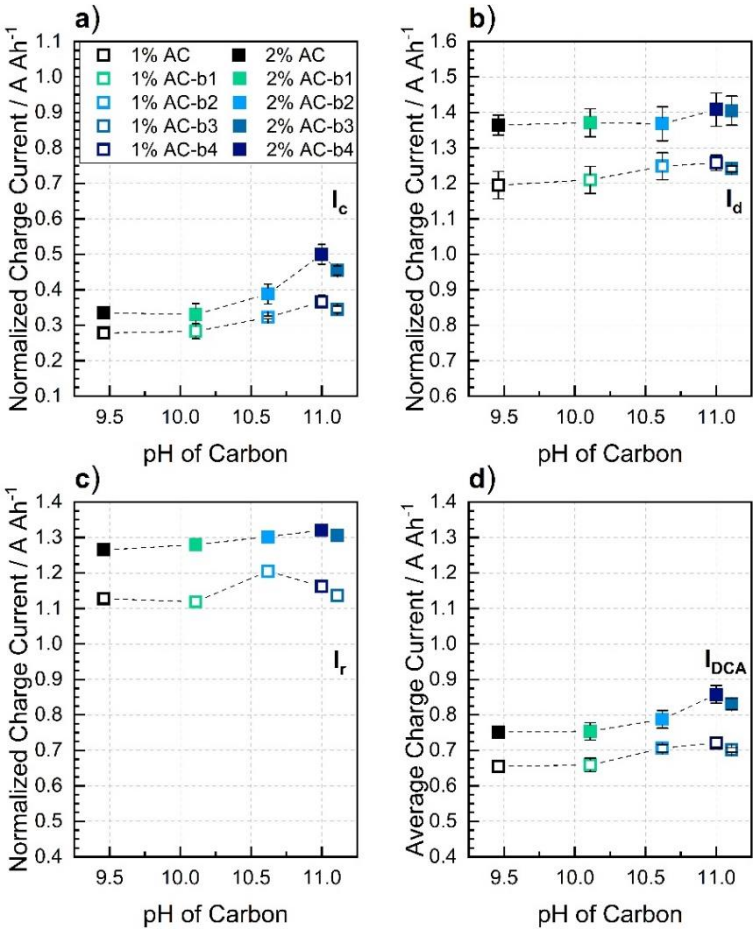

Figure 62: Relationship between carbon pH and normalized charge currents of cells containing 1 wt. % and 2 wt. % basic ACs a) after charge history (I_c); b) after discharge history (I_d); c) during one week simulated Start-Stop drive cycle (I_r). d) Correlation between carbon pH and the DCA of cells (I_{DCA}). The figure was reproduced from Bozkaya et al. [169].

By gathering all results together, both pH and amount of the carbon influence the charge acceptance I_c. In case of I_d and I_r, the surface chemistry of highly active carbon additives has only a minor impact. Therefore, the charging currents I_d and I_r depend mainly on the amount of the carbon additive. The reason for this phenomenon might be associated with a limitation in case of high charge currents (>1 A Ah^{-1}), which is observed for both 1 % and 2 % carbon-containing cells. As the charge current I_c is much lower in comparison to I_d and I_r, the impact of carbon surface chemistry can be revealed.

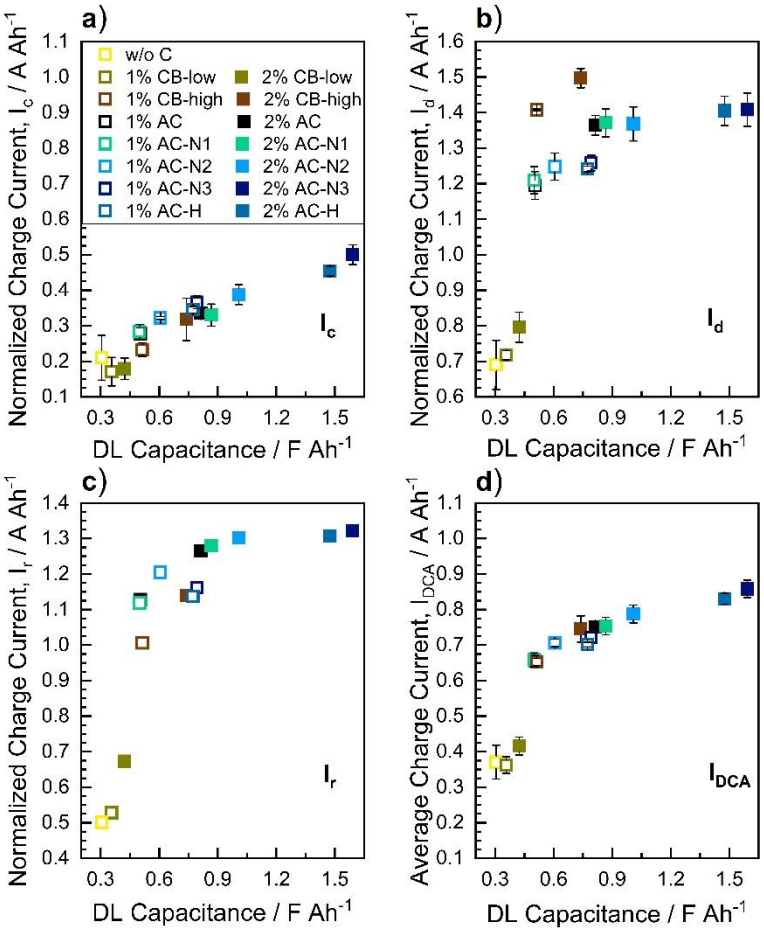

Figure 63: a) Relationship between the DL capacitance of negative electrodes and the normalized charge currents of basic ACs as well as reference cells for I_c, b) I_d, c) I_r and d) I_{DCA}. The unfilled and filled symbols show electrodes with 1 % and 2 % carbon, correspondingly. Only the yellow unfilled symbol presents the negative electrodes without carbon additive (the figure was reproduced from Bozkaya et al. [169]).

The correlation between the DL capacitance and the DCA was shown and discussed for negative electrodes with 1 % acidic and basic activated carbons. This relation is also investigated for the cells with different amounts of basic ACs as well as reference cells. Figure 63 presents the normalized charge currents and final DCA of negative electrodes with respect to the DL capacitance. After charge history, an almost linear correlation between the DL capacitance and charge currents I_c is obtained. This linkage is valid for the negative electrodes containing basic ACs and commercial CBs as well as electrodes without carbon additive (45 cells in total). For the charge currents I_d and I_r, the charge acceptance is improved via higher DL capacitance of negative electrodes. However, as discussed already above, there seems to be a saturation of charge currents above 1.2 A Ah^{-1}, which impedes a further improvement in charge-ability via greater DL capacitance. This saturation might result from other limiting effects in the cells such as

electrode grid, cell plugs and dispersion of carbon particles in negative electrodes. As the final DCA is considered, I_{DCA} is promoted via higher DL capacitance of negative electrodes. Still, the saturation in charge currents is obtained due to the contribution of I_d and I_r for the calculation of I_{DCA}. Overall, using negative electrodes providing higher DL capacitance results in improved dynamic charge acceptance. An increase of DL capacitance of negative electrodes can be achieved by increasing carbon content, by higher surface basicity of carbon and by higher specific surface area of carbon. As discussed before, the additional charge current generated in the DL region has only a minor impact on charge currents. Therefore, the DCA improvement cannot be directly originated from the capacitive charge currents. The obtained results suggest that the origin of the DCA enhancement might be related to same reason initiating improved DL capacitance values. The increased activity concerning lead sulfate reduction (charge reaction) can be explained by two possible reasons. The first one is the improvement in the lead sulfate reduction by the creation of additional conductive paths in the active material. This can be possibly achieved by using carbon additives with higher pH, as they provide higher electrical conductivity. The second reason might be related to the adsorption of lignosulfonate on specific surface functional groups of carbon. In comparison to basic functional groups, acidic groups might be the active sites for the adsorption of lignosulfonate, which could occupy the possible reaction sites for lead sulfate reduction. Therefore, pH and electrical conductivity of carbons might be the possible parameters generating the surface effects mentioned above, which could enhance the lead sulfate reduction and thereby the charge acceptance.

4.3 Summary

The goal of this study was to understand the influence of carbon surface chemistry on the electrochemical properties of lead-carbon electrodes with a focus on DCA. To reveal this effect, commercial activated carbon was chemically modified to introduce acidic and basic surface functional groups in the carbon structure. Basic ACs were prepared by gas-phase ammonia and hydrogen treatments. Gas- (air) and liquid-phase oxidative treatments (hydrogen peroxide and nitric acid) were used to produce acidic ACs. In total, ten different ACs (pristine AC, four basic ACs and five acidic ACs) possessed a broad range of carbon pH, changing between 2.5 and 11.1. According to the elemental analysis and XPS, ammonia treatments of AC resulted in an increase of nitrogen content and a decrease of oxygen content, where a higher treatment temperature pronounced this effect. In case of hydrogen treatment, a reduction in the oxygen content of carbon was obtained. Considering oxidative treatments, gas-phase modification generated a modest increase in the oxygen content. Oxidative treatments performed in the liquid phase generated a significant increase in the oxygen content in the carbon structure. The latter was further promoted by using a higher concentration of nitric acid. Further attention was given to the type of surface functional groups, which was analyzed via deconvolution of

N1s and O1s spectra obtained from XPS. Higher treatment temperature of ammonia clearly increased the relative abundance of pyridinic-N and quaternary-N groups. When the oxidized ACs were analyzed, the concentration of phenolic groups was remarkably promoted via stronger oxidative treatments. The nitrogen sorption results indicated that the textural properties of the modified ACs were not significantly altered in comparison to pristine AC. Furthermore, the electrical conductivity of ACs seems to be improved by increasing nitrogen content or decreasing oxygen content. The improved conductivity for the ammonia-modified ACs was attributed to the incorporation of quaternary-N or to the decreased amounts of oxygen groups.

Two different concentrations (1 wt. % and 2 wt. %) of ACs were included as additives in the negative electrodes. The corresponding 2 V lead-acid cells contained two positive and one negative electrode. All cells provided a 20 h discharge capacity of around 1.2 Ah. The CV measurements performed on the lead-acid cells revealed that the HER activity and the DL capacitance of the negative electrodes were enhanced by higher pH of carbon or higher carbon content. However, the impact of carbon pH on the HER as well as on the DL capacitance was more pronounced for the basic ACs compared to acidic ACs. The increased electrochemical activity via higher pH was explained by the improved rate of proton adsorption on the carbon surface or by the enhanced electrical conductivity of carbons. In case of basic ACs, the increased HER activity was linked to the higher relative abundance of pyridinic-N and/or lower concentrations of pyrrolic-N. Considering the DL capacitance, the improved capacitance was attributed to the promotion of the pseudocapacitive reactions via pyridinic-N or to the improved electron transfer via quaternary-N. On the other hand, the decreased HER and the DL capacitance for acidic ACs was associated with the passivation of the electrode´s surface, which is probably due to the acidic groups being the active sites such as for the adsorption of lignosulfonate or the lead electrodeposition.

The influence of carbon surface chemistry on charge acceptance was examined by the DCA (EN) test. In general, the charge currents after charge (I_c) and discharge (I_d) history as well as during stop/start microcycling (I_r) were increased by adding more carbon or by higher carbon pH. The proportionality of this increase for the latter was different for acidic and basic ACs. Considering I_c, the improvement in the charge acceptance was more remarkable for the basic ACs. In case of I_d, the increase of the charge currents was more significant among the acidic ACs. In terms of I_r, clear differentiation was not possible to make neither among acidic carbons nor among basic carbons. This phenomenon was attributed to an up-to-now charge current limitation during charging that results in saturation in very high charge currents. The contribution of the HER and the DL charging was determined not to be the main driver of the enhancement in the DCA, even though these electrochemical properties can be correlated to the DCA. Therefore, the DCA improvement can be attributed to the factors which also increase the

electrochemical activity of the negative electrodes. The pH of carbon, which is changed by the inclusion of specific functional groups, seems to be a crucial parameter affecting the electrochemical activity of the negative electrodes as well as the charge acceptance of lead-acid batteries.

5 Conclusion and Outlook

Lead-acid batteries in micro-hybrid vehicles require enhanced charge acceptance in order to fulfill the automotive requirements for reducing fuel consumption via specific features such as stop/start and regenerative braking. As the active material development is mainly investigated in 2 V cell-level, it is crucial to execute the dynamic charge acceptance tests, established for 12 V lead-acid batteries, on a laboratory scale. One of the main challenging aspects in DCA testing of batteries is the discrepancy in charge acceptance values obtained from the short-term and long-term usage. As the current research on this topic mostly focuses on the development and understanding of the carbon additives for the negative electrodes, a comprehensive study is needed, which gives a comparison of different DCA tests on 2 V lead-acid cells. Another important aspect for increasing DCA depends on the investigation and identification of the parameters of carbon materials, which remarkably influence the electrochemical performance of LABs. In this case, carbon surface chemistry is a strong candidate, which can be used as a key parameter for improving performance, which is known from applications like supercapacitors.

Based on the current aspects of research topics for lead-acid batteries, this dissertation aimed to improve the cell-level measurement methodology for dynamic charge acceptance in terms of carbon material screening and to demonstrate the impact of carbon surface chemistry on the electrochemical activity as well as the DCA of lead-carbon batteries. To address these two topics, this thesis was divided into two main parts, which are summarized in the following paragraphs.

Dynamic charge acceptance tests on laboratory cell-level (chapter 3)

The effect of carbon additives on different charge acceptance tests, classified as short- (CA test 2 from SBA and DCA from EN) and long-term (Run-in DCA test from Ford) tests, was investigated. For this purpose, it was crucial to use carbon additives generating a remarkable difference in DCA. In a previous study [10,72], an increase in the external surface area of carbon additives improved the charge acceptance according to the DCA (EN) test. In this dissertation, similar carbon additives with a distinct variation in the external surface area were used as additives in the negative plates of 2 V lead-acid cells. A direct proportionality between CA test 2, DCA (EN) and the 3 weeks of the Run-in DCA test was established. For the first time, the influence of carbon external surface in long-term DCA testing was shown. However, the carbon impact was revealed up to airport parking. After airport parking, only differentiation between “high” and “low” DCA cells can be made. The run-in behavior of 2 V cells, such as stabilized DCA levels at the end of the Run-in test and reversibility of the “run-in” effect, was found similar to that already known for 12 V lead-acid batteries [74,77]. Furthermore, a correlation between

the charge acceptance and capacitance values determined from the cyclic voltammetry and electrochemical impedance spectroscopy was established. This correlation between EIS and DCA was maintained for the DCA (EN) and 3 weeks of the Run-in DCA tests. According to the fitting parameters of the EIS spectrum for each negative electrode, an increase in the external surface area of carbon resulted in higher capacitances and lower charge-transfer resistance values. These findings were attributed to the surface effects originating from the external surface area of carbon. As the electrochemical properties like HER activity, DL capacitance and resistance are directly influenced by the surface effects, both electrochemical techniques (CV and EIS) were determined to be an efficient tool for carbon material screening which can be used to improve the DCA of lead-acid batteries and to investigate the dynamic processes within the active material. In conclusion, this study delivered major findings in understanding the DCA measurements on laboratory cell-level and enabled a comparison of different DCA tests with a focus on carbon additives. In terms of charge acceptance tests, both short-term DCA tests (SBA and EN) and the 3 weeks of the Run-in DCA test seem to be applicable for carbon additive screening in 2 V laboratory cells.

Influence of carbon surface chemistry on negative electrodes (chapter 4)

The impact of carbon surface chemistry on the double-layer capacitance, hydrogen evolution reaction and dynamic charge acceptance of lead-carbon electrodes was systematically investigated. For this purpose, commercial activated carbon was modified by various chemical treatments to introduce acidic and basic surface functional groups without generating significant differences in textural properties. A total of nine modified activated carbons together with the pristine AC provided a broad pH ranging between 2 and 11. For the first time, a direct correlation between the pH and electrical conductivity of carbon was established. The ten carbons (including pristine AC) were used as additives to produce negative electrodes with 1 and 2 wt. % carbon. The electrodes were finally tested in 2 V laboratory lead-acid cells. According to cyclic voltammetry measurements, both HER activity and DL capacitance of the negative electrodes were enhanced via higher pH of carbon or higher carbon content. The increased electrochemical activity of negative electrodes was attributed to the specific surface functional groups such as higher concentrations of pyridinic-N and quaternary-N or lower concentrations of pyrrolic-N. The decreased activity for electrodes containing acidic activated carbons was attributed to the passivation of the electrode´s surface probably resulting from the adsorption of lignosulfonate or electrodeposition of lead on active sites of acidic surface groups. The charge acceptance test results according to the DCA (EN) test revealed that the DCA can be improved via higher carbon pH or higher content of carbon. For DL capacitance, HER activity and charge acceptance, the impact of carbon pH was much more pronounced for the basic ACs compared to the acidic ACs, which was shown for the first time. Although a correlation between the carbon pH and DL

capacitance as well as HER activity was obtained, the charge currents generated from DL charging or HER were found insufficient to explain the increased DCA values. The improved DCA might be explained by the lead sulfate reduction being catalyzed by the carbon due to its specific surface functional groups. Explanations include the creation of additional conductive pathways through the active material by using carbons with higher electrical conductivity. Another explanation is the carbons with higher pH providing less active sites for the adsorption of lignosulfonate, which leads to a higher electrochemical active surface available for the lead sulfate reduction. Based on these findings, carbon pH or carbon surface chemistry, which is introduced by addition of surface functional groups, can be used as a performance-enhancing parameter for increasing the charge acceptance of lead-acid batteries.

This dissertation generated a significant contribution to the development of advanced lead-acid batteries by providing methodologies and major findings which are beneficial for both carbon and battery manufacturers. Within this thesis, part of the results was published in peer-reviewed scientific journals and also was presented in several international conferences, which attract the attention of the battery industry. Further understanding of the function of carbon additives was delivered within this work, which can be used to optimize and develop new carbon additives to improve the dynamic charge acceptance of lead-acid batteries. By a significant enhancement of the dynamic charge acceptance, cost-efficient lead-acid batteries can be widely employed in micro-hybrid vehicles, which can facilitate fuel savings and thereby reduce CO_2 emissions.

Zusammenfassung und Ausblick

Blei-Säure Batterien in Mikro-Hybrid-Fahrzeugen benötigen eine verbesserte Stromaufnahme, um die Anforderungen der Automobilindustrie an die Verringerung des Kraftstoffverbrauchs durch spezifische Funktionen wie Stopp/Start und regeneratives Bremsen zu erfüllen. Da die Aktivmaterialentwicklung hauptsächlich auf 2 V-Zellenebene untersucht wird, ist es von entscheidender Bedeutung, die dynamischen Stromaufnahme-Testverfahren (engl. *dynamic charge acceptance*, kurz DCA), die für 12 V Blei-Säure Batterien eingeführt wurden, im Labormaßstab durchzuführen. Eine der größten Herausforderungen bei der DCA-Prüfung von Batterien ist die Diskrepanz zwischen den Stromaufnahmewerten, die im Kurzzeit- und Langzeitbetrieb ermittelt werden. Da sich die derzeitige Forschung zu diesem Thema hauptsächlich auf die Entwicklung und das Verständnis der Kohlenstoffadditive für die negativen Elektroden konzentriert, ist eine umfassende Studie erforderlich, die einen Vergleich verschiedener DCA-Tests an 2 V-Bleisäurezellen liefert. Weitere wichtige Faktoren zur Steigerung der DCA sind die Untersuchung und Identifizierung der Parameter der Kohlenstoffmaterialien, welche die elektrochemische Leistung von Blei-Säure Batterien erheblich beeinflussen. In diesem Fall ist die Oberflächenchemie des Kohlenstoffs ein Schlüsselparameter für die Verbesserung der Leistung. Diese Oberflächenmodifikation ist beispielsweise bei Anwendungen in Superkondensatoren bekannt.

Ausgehend von den aktuellen Aspekten der Forschungsthemen für Blei-Säure Batterien zielte diese Dissertation darauf ab, die Messmethodik auf Zellebene für die dynamische Stromaufnahme im Hinblick auf das Screening von Kohlenstoffmaterialien zu verbessern und den Einfluss der Kohlenstoffoberflächenchemie auf die elektrochemische Aktivität sowie die dynamische Stromaufnahme von Blei-Kohlenstoff Batterien zu ergründen. Um diese beiden Themen zu behandeln, ist diese Arbeit in zwei Hauptteile unterteilt, die in den folgenden Abschnitten zusammengefasst werden.

Dynamische Ladeakzeptanztests auf Laborzellenniveau (Kapitel 3)

Es wurde die Wirkung von Kohlenstoffadditiven auf verschiedene Ladungsakzeptanztests untersucht, die als Kurzzeit- (CA-Test 2 von SBA und DCA von EN) und Langzeittests (Run-in DCA-Test von Ford) klassifiziert wurden. Zu diesem Zweck war es entscheidend, Kohlenstoffadditive zu verwenden, die einen bemerkenswerten Unterschied bezüglich der Stromaufnahme erzeugen. In einer früheren Studie [10,72] verbesserte eine Vergrößerung der äußeren Oberfläche von Kohlenstoffadditiven die Stromaufnahme gemäß dem DCA-Test (EN). In dieser Dissertation wurden ähnliche Kohlenstoffadditive mit einer deutlichen Variation der äußeren Oberfläche als Additive in den negativen Platten von 2 V Blei-Säurezellen verwendet. Es wurde eine direkte Proportionalität zwischen CA-Test 2, DCA (EN) und

den 3 Wochen des Run-in DCA-Tests festgestellt. Zum ersten Mal wurde der Einfluss der externen Kohlenstoffoberfläche bei DCA-Langzeittests nachgewiesen. Der Einfluss des Kohlenstoffs zeigte sich jedoch nur bis zum Flughafen Parken. Nach dem Flughafen Parken kann nur noch zwischen „höheren" und „niedrigeren" DCA-Zellen unterschieden werden. Das Run-In Verhalten von 2 V-Zellen, wie z. B. stabilisierte DCA-Werte am Ende des Run-in-Tests und der Reversibilität des „Run-In"-Effekt, wurde ähnlich wie bei bereits bekannten 12 V Bleibatterien festgestellt [74,77]. Darüber hinaus wurde eine Korrelation zwischen den aus der zyklischen Voltammetrie und der elektrochemischen Impedanzspektroskopie (engl. *electrochemical impedance spectroscopy*, kurz EIS) ermittelten Ladungsaufnahme- und Kapazitätswerten festgestellt. Diese Korrelation zwischen EIS und DCA wurde für die DCA (EN) und die dreiwöchigen Run-in DCA-Tests beibehalten. Durch Anpassung der Parameter des EIS-Spektrums für jede negative Elektrode führte eine Vergrößerung der externen Oberfläche des Kohlenstoffs zu höheren Kapazitäten und niedrigeren Ladungstransferwiderständen. Diese Ergebnisse wurden auf die Oberflächeneffekte zurückgeführt, die von der externen Kohlenstoffoberfläche ausgehen. Da die elektrochemischen Eigenschaften wie Wasserstoffentwicklungsreaktion (engl. *hydrogen evolution reaction*, kurz HER), Doppelschichtkapazität (engl. *double-layer capacitance*, kurz DL) und Widerstand direkt von den Oberflächeneffekten beeinflusst werden, erwiesen sich beide elektrochemischen Techniken (Zyklovoltammetrie und EIS) als effizientes Werkzeug für das Screening von Kohlenstoffmaterialien. Diese können zur Verbesserung der Stromaufnahme von Blei-Säure Batterien eingesetzt werden. Zusammenfassend lässt sich sagen, dass diese Doktorarbeit wichtige Erkenntnisse zum Verständnis der DCA-Messungen auf der Ebene von Laborzellen lieferte und einen Vergleich verschiedener DCA-Tests mit Kohlenstoffadditiven als Schwerpunkt ermöglichte. Was die Ladungsakzeptanztests betrifft, so scheinen sowohl die Kurzzeit-DCA-Tests (SBA und EN) als auch der dreiwöchige Run-in-DCA-Test für das Screening von Kohlenstoffadditiven in 2 V Laborzellen geeignet zu sein.

Einfluss der Kohlenstoffoberflächenchemie auf negative Elektroden (Kapitel 4)

Der Einfluss der Oberflächenchemie von Kohlenstoff auf die Doppelschichtkapazität, Wasserstoffentwicklungsreaktion und die dynamische Stromaufnahme von Bleikohlenstoffelektroden wurde systematisch untersucht. Zu diesem Zweck wurde Aktivkohle durch verschiedene chemische Behandlungen modifiziert, um saure und basische funktionelle Gruppen in die Oberfläche einzubringen, ohne signifikante Unterschiede in den strukturellen Eigenschaften zu erzeugen. Insgesamt neun modifizierte Aktivkohlen lieferten zusammen mit der nicht modifizierten Aktivkohle einen breiten pH-Bereich zwischen 2 und 11. Zum ersten Mal wurde eine direkte Korrelation zwischen dem pH-Wert und der elektrischen Leitfähigkeit von Kohlenstoff festgestellt. Die zehn Kohlenstoffe (einschließlich der unberührten Aktivkohle) wurden als Additive

zur Herstellung negativer Elektroden mit 1 und 2 Gew.-% Kohlenstoff verwendet. Die Elektroden wurden schließlich in 2 V Blei-Säure Laborzellen getestet. Messungen mittels zyklischer Voltammetrie ergaben, dass sowohl die Aktivität der HER als auch die DL-Kapazität der negativen Elektroden durch einen höheren pH-Wert der Aktivkohle oder einen höheren Kohlenstoffgehalt verstärkt wurden. Die erhöhte elektrochemische Aktivität der negativen Elektroden wurde auf die spezifischen funktionellen Oberflächengruppen wie höhere Konzentrationen von Pyridin-N und Quaternär-N oder niedrigere Konzentrationen von Pyrrol-N zurückgeführt. Die geringere Aktivität bei Elektroden mit sauren Aktivkohlen wurde auf die Passivierung der Elektrodenoberfläche zurückgeführt, die wahrscheinlich auf die Adsorption von Ligninsulfonat oder die galvanische Abscheidung von Blei an aktiven Stellen der sauren Oberflächengruppen zurückzuführen ist. Die Ergebnisse des Ladungsakzeptanztests gemäß dem DCA (EN)-Test zeigten, dass die Stromaufnahme durch einen höheren pH-Wert des Kohlenstoffs oder einen höheren Kohlenstoffgehalt verbessert werden kann. Bei der DL-Kapazität, der HER-Aktivität und der Ladungsakzeptanz war der Einfluss des pH-Werts des Kohlenstoffs bei den basischen Aktivkohlen viel ausgeprägter als bei den sauren Aktivkohlen, was zum ersten Mal gezeigt wurde. Obwohl eine Korrelation zwischen dem Kohlenstoff-pH-Wert und der DL-Kapazität sowie der HER-Aktivität festgestellt wurde, erwiesen sich die durch die DL-Ladung oder HER erzeugten Ladungsströme als unzureichend, um die erhöhten DCA-Werte zu erklären. Der verbesserte DCA-Wert könnte darauf zurückzuführen sein, dass die Reduktion von Bleisulfat durch den Kohlenstoff aufgrund seiner spezifischen funktionellen Oberflächengruppen katalysiert wird. Zu den Erklärungen gehört die Schaffung zusätzlicher leitfähiger Pfade durch das aktive Material durch die Verwendung von Kohlenstoffen mit höherer elektrischer Leitfähigkeit. Eine weitere Erklärung ist, dass Kohlenstoffe mit höherem pH-Wert weniger aktive Stellen für die Adsorption von Ligninsulfonat bieten, was zu einer größeren elektrochemisch aktiven Oberfläche für die Bleisulfatreduktion führt. Auf der Grundlage dieser Erkenntnisse kann der pH-Wert des Kohlenstoffs oder die Oberflächenchemie des Kohlenstoffs, die durch das Einbringen von funktionellen Oberflächengruppen bereitgestellt werden, als leistungssteigernder Parameter zur Erhöhung der Stromaufnahme von Blei-Säure Batterien genutzt werden.

Diese Dissertation leistete einen bedeutenden Beitrag zur Entwicklung fortschrittlicher Bleisäurebatterien, indem sie Methoden und wichtige Erkenntnisse lieferte, die sowohl für Kohlenstoff- als auch für Batteriehersteller von Nutzen sind. Im Rahmen dieser Arbeit wurden Teile der Ergebnisse in wissenschaftlichen Zeitschriften veröffentlicht und auf mehreren internationalen Konferenzen vorgestellt, welche die Aufmerksamkeit der Batterieindustrie auf sich ziehen. Im Rahmen dieser Arbeit wurden weitere Erkenntnisse über die Funktion von Kohlenstoffadditiven gewonnen, die zur Optimierung und Entwicklung neuer Kohlenstoffadditive zur Verbesserung der dynamischen Stromaufnahme von Bleibatterien genutzt werden können. Durch eine signifikante

Verbesserung der dynamischen Stromaufnahme können kosteneffiziente Blei-Säure Batterien in großem Umfang in Mikro-Hybrid-Fahrzeugen eingesetzt werden, was zu Kraftstoffeinsparungen und damit zur Verringerung der CO_2-Emissionen führen kann.

6 References

1. Garche, J.; Karden, E.; Moseley, P.T.; Rand, D., Eds.; *Lead-acid batteries for future automobiles;* Elsevier: Amsterdam, Oxford, Cambridge, **2017**, ISBN 9780444637031.

2. Pavlov, D. *Lead-acid batteries: Science and technology*: *A handbook of lead-acid battery technology and its influence on the product;* Elsevier Science: San Diego, **2011**, ISBN 9780444528827.

3. Budde-Meiwes, H.; Drillkens, J.; Lunz, B.; Muennix, J.; Rothgang, S.; Kowal, J.; Sauer, D.U. A review of current automotive battery technology and future prospects. *Proceedings of the Institution of Mechanical Engineers, Part D: Journal of Automobile Engineering* **2013**, *227*, 761–776, doi:10.1177/0954407013485567.

4. Valenciano, J.; Fernández, M.; Trinidad, F.; Sanz, L. Lead-acid batteries for micro- and mild-hybrid applications. *Journal of Power Sources* **2009**, *187*, 599–604, doi:10.1016/j.jpowsour.2008.11.089.

5. European Comittee for Electrotechnical Standardisation. *Lead-acid starter batteries - Part 6: Batteries for micro-cycle applications*, **2015** (EN 50342-6:2015).

6. Enos, D.G.; Ferreira, S.R.; Barkholtz, H.M.; Baca, W.; Fenstermacher, S. Understanding function and performance of carbon additives in lead-acid batteries. *Journal of the Electrochemical Society* **2017**, *164*, A3276-A3284, doi:10.1149/2.1031713jes.

7. Pavlov, D. *Lead-acid batteries: Science and technology*: *Chapter 7: Additives to the pastes for positive and negative battery plates;* Elsevier, **2011**, ISBN 978-0-444-52882-7.

8. Pavlov, D.; Rogachev, T.; Nikolov, P.; Petkova, G. Mechanism of action of electrochemically active carbons on the processes that take place at the negative plates of lead-acid batteries. *Journal of Power Sources* **2009**, *191*, 58–75, doi:10.1016/j.jpowsour.2008.11.056.

9. Pavlov, D.; Nikolov, P.; Rogachev, T. Influence of carbons on the structure of the negative active material of lead-acid batteries and on battery performance. *Journal of Power Sources* **2011**, *196*, 5155–5167, doi:10.1016/j.jpowsour.2011.02.014.

10. Settelein, J.; Oehm, J.; Bozkaya, B.; Leicht, H.; Wiener, M.; Reichenauer, G.; Sextl, G. The external surface area of carbon additives as key to enhance the

dynamic charge acceptance of lead-carbon electrodes. *Journal of Energy Storage* **2018**, *15*, 196–204, doi:10.1016/j.est.2017.11.016.

11. Nethaji, E.L.; Srinivas, K.; Murthy, K.S.; Jagadish, M. Effect of properties of carbon materials on performance of VRLA batteries. *Journal of Power and Energy Engineering* **2015**, *9*, 1029–1035, doi:10.17265/1934-8975/2015.11.011.

12. Moseley, P.T. Consequences of including carbon in the negative plates of Valve-regulated Lead–Acid batteries exposed to high-rate partial-state-of-charge operation. *Journal of Power Sources* **2009**, *191*, 134–138, doi:10.1016/j.jpowsour.2008.08.084.

13. Moseley, P.T.; Rand, D.A.; Davidson, A.; Monahov, B. Understanding the functions of carbon in the negative active-mass of the lead–acid battery: A review of progress. *Journal of Energy Storage* **2018**, *19*, 272–290, doi:10.1016/j.est.2018.08.003.

14. Boden, D.P.; Loosemore, D.V.; Spence, M.A.; Wojcinski, T.D. Optimization studies of carbon additives to negative active material for the purpose of extending the life of VRLA batteries in high-rate partial-state-of-charge operation. *Journal of Power Sources* **2010**, *195*, 4470–4493, doi:10.1016/j.jpowsour.2009.12.069.

15. Wulfert-Holzmann, P.; Huck, M.; Gold, L.; Settelein, J.; Sauer, D.U.; Giffin, G.A. A New In Situ and Operando Measurement Method to Determine the Electrical Conductivity of the Negative Active Material in Lead-Acid Batteries during Operation. *Journal of the Electrochemical Society* **2021**, *168*, 50537, doi:10.1149/1945-7111/ac00f5.

16. Hosaka, D. Investigation of Water Consumption Mechanism of Flooded Type ISS Batteries to Balance with Charge Acceptance. *8th International Advanced Automotive Battery Conference (AABC Europe)*, Mainz, Germany, January **2018**.

17. Wang, F.; Hu, C.; Zhou, M.; Wang, K.; Lian, J.; Yan, J.; Cheng, S.; Jiang, K. Research progresses of cathodic hydrogen evolution in advanced lead–acid batteries. *Science Bulletin* **2016**, *61*, 451–458, doi:10.1007/s11434-016-1023-0.

18. Settelein, J.; Lorrmann, H.; Sextl, G. Evaluating the lead affinity of graphite additives in lead-acid batteries by electrochemical deposition. *Electrochimica Acta* **2017**, *233*, 173–180, doi:10.1016/j.electacta.2017.03.034.

19. Calvo, E.G.; Rey-Raap, N.; Arenillas, A.; Menéndez, J.A. The effect of the carbon surface chemistry and electrolyte pH on the energy storage of supercapacitors. *RSC Advances* **2014**, *4*, 32398–32404, doi:10.1039/C4RA04430D.

20. Śliwak, A.; Díez, N.; Miniach, E.; Gryglewicz, G. Nitrogen-containing chitosan-based carbon as an electrode material for high-performance supercapacitors. *Journal of Applied Electrochemistry* **2016**, *46*, 667–677, doi:10.1007/s10800-016-0955-z.

21. Liu, H.; Song, H.; Chen, X.; Zhang, S.; Zhou, J.; Ma, Z. Effects of nitrogen- and oxygen-containing functional groups of activated carbon nanotubes on the electrochemical performance in supercapacitors. *Journal of Power Sources* **2015**, *285*, 303–309, doi:10.1016/j.jpowsour.2015.03.115.

22. Hulicova-Jurcakova, D.; Seredych, M.; Lu, G.Q.; Bandosz, T.J. Combined effect of nitrogen- and oxygen-containing functional groups of microporous activated carbon on its electrochemical performance in supercapacitors. *Advanced Functional Materials* **2009**, *19*, 438–447, doi:10.1002/adfm.200801236.

23. DuPasquier, A.; Kirchev, A.; Miller, D.; Merritt, B.; Atanassova, P.; Oljaca, M. Carbon black surface modifications for reduced hydrogen evolution reaction. *10th International Conference on Lead-Acid Batteries (LABAT)*, Golden Sands, Bulgaria, June **2017**.

24. Hong, B.; Yu, X.; Jiang, L.; Xue, H.; Liu, F.; Li, J.; Liu, Y. Hydrogen evolution inhibition with diethylenetriamine modification of activated carbon for a lead-acid battery. *RSC Advances* **2014**, *4*, 33574–33577, doi:10.1039/C4RA04245J.

25. Shafeeyan, M.; Daud, W.; Houshmand, A.; Shamiri, A. A review on surface modification of activated carbon for carbon dioxide adsorption. *Journal of Analytical and Applied Pyrolysis* **2010**, *89*, 143–151, doi:10.1016/j.jaap.2010.07.006.

26. Budde-Meiwes, H.; Schulte, D.; Kowal, J.; Sauer, D.U.; Hecke, R.; Karden, E. Dynamic charge acceptance of lead–acid batteries: Comparison of methods for conditioning and testing. *Journal of Power Sources* **2012**, *207*, 30–36, doi:10.1016/j.jpowsour.2011.12.045.

27. Kowal, J.; Schulte, D.; Sauer, D.U.; Karden, E. Simulation of the current distribution in lead-acid batteries to investigate the dynamic charge acceptance in flooded SLI batteries. *Journal of Power Sources* **2009**, *191*, 42–50, doi:10.1016/j.jpowsour.2008.12.016.

28. Karden, E.; Jöris, F.; Budde-Meiwes, H.; Sauer, D.U. Test Methods for Dynamic Charge Acceptance (DCA) of Microhybrid Starter Batteries. *13th European Lead Battery Conference (ELBC)*, Paris, France, September **2012**.

29. Hamann, C.H.; Hamnett, A.; Vielstich, W. *Electrochemistry*, 2nd, completely rev. and updated ed.; Wiley-VCH: Weinheim, **2007**, ISBN 352731069X.

30. Scholz, F.; Bond, A.M., Eds., *Electroanalytical methods*: *Guide to experiments and applications;* 2., rev. and extended ed.; Springer: Berlin, **2010**, ISBN 9783642029158.

31. Pletcher, D. *A first course in electrode processes*, 2. ed.; RSC Publ: Cambridge, **2009**, ISBN 9781847558930.

32. Zheng, Y.; Jiao, Y.; Jaroniec, M.; Qiao, S.Z. Advancing the electrochemistry of the hydrogen-evolution reaction through combining experiment and theory. *Angewandte Chemie Internation* Edition, **2015**, *54*, 52–65, doi:10.1002/anie.201407031.

33. Lasia, A. Mechanism and kinetics of the hydrogen evolution reaction. *International Journal of Hydrogen Energy* **2019**, *44*, 19484–19518, doi:10.1016/j.ijhydene.2019.05.183.

34. Kahyarian, A.; Achour, M.; Nesic, S. CO2 corrosion of mild steel. *Trends in Oil and Gas Corrosion Research and Technologies*; Elsevier, **2017**, ISBN 9780081011058.

35. Conway, B.E.; Tilak, B.V. Interfacial processes involving electrocatalytic evolution and oxidations of H_2, and the role of chemisorbed H. *Electrochimica Acta* **2002**, *47*, 3571–3594, doi:10.1016/S0013-4686(02)00329-8.

36. Bockris, J.; Potter, E.C. The mechanism of the cathodic hydrogen evolution reaction. *Journal of the Electrochemical Society* **1952**, *99*, 169–186, doi:10.1149/1.2779692.

37. Trasatti, S. Work function, electronegativity, and electrochemical behavior of metals: Electrolytic hydrogen evolution in acid solutions. *Journal of Electroanalytical Chemistry and Interfacial Electrochemistry* **1972**, *39,* 163–184, doi:10.1016/S0022-0728(72)80485-6.

38. Quaino, P.; Juarez, F.; Santos, E.; Schmickler, W. Volcano plots in hydrogen electrocatalysis - uses and abuses. *Beilstein Journal of Nanotechnolgy* **2014**, *5*, 846–854, doi:10.3762/bjnano.5.96.

39. Sabatier, P. Hydrogénations et déshydrogénations par catalyse. *European Journal of Inorganic Chemistry* **1911**, 44, 1984–2001, doi:10.1002/cber.19110440303.

40. Elgrishi, N.; Rountree, K.J.; McCarthy, B.D.; Rountree, E.S.; Eisenhart, T.T.; Dempsey, J.L. A practical beginner's guide to cyclic voltammetry. *Journal of Chemical Education* **2018**, *95*, 197–206, doi:10.1021/acs.jchemed.7b00361.

41. Rusling, J.F.; Suib, S.L. Characterizing materials with cyclic voltammetry. Advanced Materials **1994**, *6*, 922–930, doi:10.1002/adma.19940061204.

42. Béguin, F.; Frackowiak, E., Eds., *Carbons for electrochemical energy storage and conversion systems;* CRC: Boca Raton, **2010**, ISBN 9781420053074.

43. Compton, R.G.; Laborda, E.; Ward, K.R. *Understanding Voltammetry: Simulation of electrode processes;* Imperial Colloge Press, **2014**, ISBN 978-1-78326-323-3.

44. Fattakhova-Rohlfing, D. *Special topics III: Electrochemistry*: *Fundamentals and Application*. Advanced Materials Science (AMS) Master Program, WS 2013/2014 Lecture Notes, LMU München, **2013**.

45. Kwiecien, M.; Huck, M.; Badeda, J.; Zorer, C.; Komut, K.; Yu, Q.; Sauer, D.U. Variation of Impedance in Lead-Acid Batteries in the Presence of Acid Stratification. *Applied Sciences* **2018**, *8*, 1018, doi:10.3390/app8071018.

46. Lefrou, C.; Fabry, P.; Poignet, J.-C. *Electrochemistry*: *The Basics, With Examples;* Springer Berlin Heidelberg: Berlin, Heidelberg, **2012**, ISBN 9783642302503.

47. Kwiecien, M. *Electrochemical Impedance Spectroscopy on Lead-Acid Cells during Aging*. PhD Thesis; Universitätsbibliothek der RWTH: Aachen, **2019**.

48. Karden, E. *Using low-frequency impedance spectroscopy for characterization, monitoring, and modeling of industrial batteries*. PhD Thesis; RWTH Aachen University, Aachen, **2002**, ISBN 3826597664.

49. Hawkins, J.M.; Barling, L.O., Eds. *Some aspects of battery impedance characteristics;* 17th International Telecommunications Energy Conference (INTELEC 95), The Hague, Netherlands, Inst. of Electrical and Electronics Engineers: New York, NY, **1995**.

50. Diard, J.P.; Gorrec, B.; Montella, C.; Poinsignon, C.; Vitter, G. Impedance measurements of polymer electrolyte membrane fuel cells running on constant

load. *Journal of Power Sources* **1998**, *74*, 244–245, doi:10.1016/S0378-7753(98)00056-1.

51. Hampson, N.A.; Lakeman, J.B. The electrochemistry of the porous lead electrode in sulphuric acid — a selective review. *Journal of Power Sources* **1981**, *6*, 101–120, doi:10.1016/0378-7753(81)80018-3.

52. Varela, F.E.; Vela, M.E.; Vilche, J.R.; Arvia, A.J. Kinetics and mechanism of PbSO4 electroformation on Pb electrodes in H2SO4 aqueous solutions. *Electrochimica Acta* **1993**, *38*, 1513–1520, doi:10.1016/0013-4686(93)80283-6.

53. Guo, Y.; Groiss, R.; Döring, H.; Garche, J. Rate-Determining Step Investigations of Oxidation Processes at the Positive Plate during Pulse Charge of Valve-Regulated Lead-Acid Batteries. *Journal of the Electrochemical Society* **1999**, *146*, 3949–3957, doi:10.1149/1.1392575.

54. Bode, H. *Lead-Acid Batteries;* John Wiley & Sons: New York, **1977**, ISBN 0-471-08455-7.

55. Pavlov, D. The Lead-Acid Battery Lead Dioxide Active Mass: A Gel-Crystal System with Proton and Electron Conductivity. *Journal of the Electrochemical Society* **1992**, *139*, 3075–3080, doi:10.1149/1.2069034.

56. Pavlov, D.; Monahov, B. Mechanism of the Elementary Electrochemical Processes Taking Place during Oxygen Evolution on the Lead Dioxide Electrode. *Journal of the Electrochemical Society* **1996**, *143*, 3616–3629, doi:10.1149/1.1837261.

57. Beck, F. A Semiconductor Model for the Cathodic Passivation of Lead Dioxide. *Journal of the Electrochemical Society* **1982**, *129*, 1880–1885, doi:10.1149/1.2124319.

58. Macdonald, J.R., Ed., *Impedance spectroscopy*: *Emphasizing solid materials and systems,* Wiley: New York, **1987**, ISBN 0471831220.

59. Mauracher, P.; Karden, E. Dynamic modelling of lead/acid batteries using impedance spectroscopy for parameter identification. *Journal of Power Sources* **1997**, *67*, 69–84, doi:10.1016/S0378-7753(97)02498-1.

60. Randles, J. Kinetics of rapid electrode reactions. *Discussions of the Faraday Society* **1947**, *1*, 11, doi:10.1039/df9470100011.

61. Bullock, K.R. The electromotive force of the lead-acid cell and its half-cell potentials. *Journal of Power Sources* **1991**, *35*, 197–223, doi:10.1016/0378-7753(91)80107-9.

62. Planté; G. Nouvelle pile secondaire d`une grande puissance **1860**, 640–642.

63. Cao, S.; Duan, X.; Zhao, X.; Wang, B.; Ma, J.; Fan, D.; Sun, C.; He, B.; Wei, F.; Jiang, G. Health risk assessment of various metal(loid)s via multiple exposure pathways on children living near a typical lead-acid battery plant, China. *Environmental Pollution* **2015**, *200*, 16–23, doi:10.1016/j.envpol.2015.02.010.

64. Pourbaix, M. *Atlas of electrochemical equilibria in aqueous solution;* Pergamon: New York, **1966**.

65. Daniel, C., Ed., *Handbook of battery materials,* 2., completely rev. and enlarged ed.; Wiley-VCH: Weinheim, **2011**, ISBN 9783527326952.

66. Pavlov, D.; Nikolov, P.; Rogachev, T. Influence of expander components on the processes at the negative plates of lead-acid cells on high-rate partial-state-of-charge cycling. Part II. Effect of carbon additives on the processes of charge and discharge of negative plates. *Journal of Power Sources* **2010**, *195*, 4444–4457, doi:10.1016/j.jpowsour.2009.12.132.

67. Pavlov, D.; Nikolov, P. Lead–Carbon Electrode with Inhibitor of Sulfation for Lead-Acid Batteries Operating in the HRPSoC Duty. *Journal of the Electrochemical Society* **2012**, *159*, A1215-A1225, doi:10.1149/2.035208jes.

68. Garche, J.; Dyer, C.K.; Moseley, P.T.; Ogumi, Z.; Rand, D.; Scrosati, B. *Encyclopedia of electrochemical power sources;* Elsevier: Amsterdam, **2009**, ISBN 9780444520937.

69. Gubbins, K.E.; Walker Jr., R.D. The solubility and diffusivity of oxygen in electrolytic solutions. *Journal of the Electrochemical Society* **1965**, *112*, 469–471, doi:10.1149/1.2423575/meta.

70. Mrha, J.; Micka, K.; Jindra, J.; Musilova, M. Oxygen cycle in sealed lead-acid batteries. *Journal of Power Sources* **1989**, *27*, 91–117, doi:10.1016/0378-7753(89)80125-9.

71. Berndt, D. Valve-regulated lead-acid batteries. *Journal of Power Sources* **2001**, *95*, 29–46, doi:10.1016/S0378-7753(01)00881-3.

72. Settelein, J. Kohlenstoffadditive für negative Elektroden von modernen Blei-Säure Batterien. PhD thesis; Julius-Maximilians-Universität Würzburg, Würzburg, **2020**.

73. Lach, J.; Wróbel, K.; Wróbel, J.; Podsadni, P.; Czerwiński, A. Applications of carbon in lead-acid batteries: a review. *Journal of Solid State Electrochemistry* **2019**, *23*, 693–705, doi:10.1007/s10008-018-04174-5.

74. Budde-Meiwes, H. Dynamic charge acceptance of lead-acid batteries for micro-hybrid automotive applications. PhD thesis; RWTH Aachen University, Aachen, **2016**.

75. Karden, E.; Ploumen, S.; Fricke, B.; Miller, T.; Snyder, K. Energy storage devices for future hybrid electric vehicles. *Journal of Power Sources* **2007**, *168*, 2–11, doi:10.1016/j.jpowsour.2006.10.090.

76. Karden, E. Dynamic Charge Acceptance (DCA) Test Method Development for EN 50342-6. *Innovations in Lead-Acid Batteries - ALABC Workshop*, Würzburg, Germany, **2015**.

77. Budde-Meiwes, H.; Schulte, D.; Kowal, J.; Sauer, D.U.; Hecke, R.; Karden, E. Dynamic charge acceptance of lead–acid batteries: Comparison of methods for conditioning and testing. *Journal of Power Sources* **2012**, *207*, 30–36, doi:10.1016/j.jpowsour.2011.12.045.

78. Christen, U.; Romano, P.; Karden, E. Estimator for charge acceptance of lead acid batteries. *Oil Gas Sci. Technol. – Revue IFP Energies nouvelles* **2012**, *67*, 613–631, doi:10.2516/ogst/2012007.

79. Schaeck, S.; Stoermer, A.O.; Kaiser, F.; Koehler, L.; Albers, J.; Kabza, H. Lead-acid batteries in micro-hybrid applications. Part I. Selected key parameters. *Journal of Power Sources* **2011**, *196*, 1541–1554, doi:10.1016/j.jpowsour.2010.08.077.

80. Lam, L.; Haigh, N.; Phyland, C.; Urban, A. Failure mode of valve-regulated lead-acid batteries under high-rate partial-state-of-charge operation. *Journal of Power Sources* **2004**, *133*, 126–134, doi:10.1016/j.jpowsour.2003.11.048.

81. Moseley, P.T.; Rand, D.A.; Peters, K. Enhancing the performance of lead–acid batteries with carbon – In pursuit of an understanding. *Journal of Power Sources* **2015**, *295*, 268–274, doi:10.1016/j.jpowsour.2015.07.009.

82. Sauer, D.U.; Karden, E.; Fricke, B.; Blanke, H.; Thele, M.; Bohlen, O.; Schiffer, J.; Gerschler, J.B.; Kaiser, R. Charging performance of automotive batteries—An underestimated factor influencing lifetime and reliable battery operation. *Journal of Power Sources* **2007**, *168*, 22–30, doi:10.1016/j.jpowsour.2006.11.064.

83. Moseley, P.T.; Rand, D. Partial State-of-Charge Duty: A Challenge but Not a Show-Stopper for Lead-Acid Batteries! *ECS Transactions* **2012**, *41*, 3–16, doi:10.1149/1.3691907.

84. Pavlov, D.; Nikolov, P. Capacitive carbon and electrochemical lead electrode systems at the negative plates of lead–acid batteries and elementary processes on cycling. *Journal of Power Sources* **2013**, *242*, 380–399, doi:10.1016/j.jpowsour.2013.05.065.

85. Xiang, J.; Ding, P.; Zhang, H.; Wu, X.; Chen, J.; Yang, Y. Beneficial effects of activated carbon additives on the performance of negative lead-acid battery electrode for high-rate partial-state-of-charge operation. *Journal of Power Sources* **2013**, *241*, 150–158, doi:10.1016/j.jpowsour.2013.04.106.

86. Pavlov, D.; Nikolov, P.; Rogachev, T. Influence of expander components on the processes at the negative plates of lead-acid cells on high-rate partial-state-of-charge cycling. Part II. Effect of carbon additives on the processes of charge and discharge of negative plates. *Journal of Power Sources* **2010**, *195*, 4444–4457, doi:10.1016/j.jpowsour.2009.12.132.

87. Bača, P.; Micka, K.; Křivík, P.; Tonar, K.; Tošer, P. Study of the influence of carbon on the negative lead-acid battery electrodes. *Journal of Power Sources* **2011**, *196*, 3988–3992, doi:10.1016/j.jpowsour.2010.11.046.

88. Nakamura, K.; Shiomi, M.; Takahashi, K.; Tsubota, M. Failure modes of valve-regulated lead/acid batteries. *Journal of Power Sources* **1996**, *59*, 153–157, doi:10.1016/0378-7753(95)02317-8.

89. Shiomi, M.; Funato, T.; Nakamura, K.; Takahashi, K.; Tsubota, M. Effects of carbon in negative plates on cycle-life performance of valve-regulated lead/acid batteries. *Journal of Power Sources* **1997**, *64*, 147–152, doi:10.1016/S0378-7753(96)02515-3.

90. Fernández, M.; Valenciano, J.; Trinidad, F.; Muñoz, N. The use of activated carbon and graphite for the development of lead-acid batteries for hybrid vehicle applications. *Journal of Power Sources* **2010**, *195*, 4458–4469, doi:10.1016/j.jpowsour.2009.12.131.

91. Ebner, E.; Burow, D.; Börger, A.; Wark, M.; Atanassova, P.; Valenciano, J. Carbon blacks for the extension of the cycle life in flooded lead acid batteries for micro-hybrid applications. *Journal of Power Sources* **2013**, *239*, 483–489, doi:10.1016/j.jpowsour.2013.03.124.

92. Hollenkamp, A.F.; Baldsing, W.; Lau, S.; Lim, O.V.; Newnham, R.H.; Rand, D.; Rosalie, J.M.; Vella, D.G.; Vu, L.H. *Overcoming negative-plate capacity loss in VRLA batteries cycled under partial-state-of-charge duty*: *ALABC Project N1.2, Final Report*, Research Triangle Park, NC, USA, **2002**.

93. Arun, S.; Mithin Kumar, S.; Uday Venkat Kiran, K.; Mayavan S. Effects of carbon surface area and morphology on performance of stationary lead acid battery. *Journal of Energy Storage* **2020**, *32*, 101763, doi:10.1016/j.est.2020.101763.

94. Moseley, P.T.; Nelson, R.F.; Hollenkamp, A.F. The role of carbon in valve-regulated lead–acid battery technology. *Journal of Power Sources* **2006**, *157*, 3–10, doi:10.1016/j.jpowsour.2006.02.031.

95. Dyatkin, B.; Gogotsi, Y. Effects of structural disorder and surface chemistry on electric conductivity and capacitance of porous carbon electrodes. *Faraday Discuss.* **2014**, *172*, 139–162, doi:10.1039/c4fd00048j.

96. Suslova, E.V.; Arkhipova, E.A.; Kalashnik, A.V.; Ivanov, A.S.; Savilov, S.V.; Xia, H.; Lunin, V.V. Effect of the functionalization of nitrogen-doped carbon nanotubes on electrical conductivity. *Russian Journal of Physical Chemistry* **2019**, *93*, 1952–1956, doi:10.1134/S0036024419100303.

97. Ismagilov, Z.R.; Shalagina, A.E.; Podyacheva, O.; Ischenko, A.V.; Kibis, L.S.; Boronin, A.I.; Chesalov, Y.A.; Kochubey, D.I.; Romanenko, A.I.; Anikeeva, O.B.; et al. Structure and electrical conductivity of nitrogen-doped carbon nanofibers. *Carbon* **2009**, *47*, 1922–1929, doi:10.1016/j.carbon.2009.02.034.

98. Micka, K.; Calábek, M.; Bača, P.; Křivák, P.; Lábus, R.; Bilko, R. Studies of doped negative valve-regulated lead-acid battery electrodes. *Journal of Power Sources* **2009**, *191*, 154–158, doi:10.1016/j.jpowsour.2009.01.014.

99. Calábek, M.; Micka, K.; Křivák, P.; Bača, P. Significance of carbon additive in negative lead-acid battery electrodes. *Journal of Power Sources* **2006**, *158*, 864–867, doi:10.1016/j.jpowsour.2005.11.022.

100. Moseley, P.T.; Rand, D.; Davidson, A.; Monahov, B. Understanding the functions of carbon in the negative active-mass of the lead–acid battery: A review of progress. *Journal of Energy Storage* **2018**, *19*, 272–290, doi:10.1016/j.est.2018.08.003.

101. Wang, L.; Zhang, H.; Cao, G.; Zhang, W.; Zhao, H.; Yang, Y. Effect of activated carbon surface functional groups on nano-lead electrodeposition and hydrogen evolution and its applications in lead-carbon batteries. *Electrochimica Acta* **2015**, *186*, 654–663, doi:10.1016/j.electacta.2015.11.007.

102. Zhang, B.; Wen, Z.; Ci, S.; Chen, J.; He, Z. Nitrogen-doped activated carbon as a metal free catalyst for hydrogen production in microbial electrolysis cells. *RSC Advances* **2014**, *4*, 49161–49164, doi:10.1039/C4RA08555H.

103. Riley, L.A.; Sakshaug, A.J.; Feaver, A.M. *Characterizations of carbons and understanding their hydrogen gassing properties in lead-acid battery negative plaes*: *ALABC Project 1012L, Final Report*, Durham, NC, USA, **2012**.

104. Atanassova, P.; Oljaca, M.; Nikolov, P.; Matrakova, M.; Pavlov, D. Performance additives for advanced lead-acid battery applications. *15th Asian Battery Conference* **2013**.

105. Béguin, F.; Frackowiak, E. *Carbons for electrochemical energy storage and conversion systems;* Taylor & Francis: USA, **2009**, ISBN 9781420053074.

106. Kinoshita, K. *Carbon*: *Electrochemical and physicochemical properties;* Wiley: New York, USA, **1988**, ISBN 0471848026.

107. Winter, M.; Moeller, K.C.; Besenhard, J.O. Carbonaceous and Graphitic Anodes. *Nazri G.A., Pistoia G., Eds.; Lithium Batteries Science and Technology*; Springer: New York, USA, **2003**, 144–194, ISBN 978-0-387-92675-9.

108. Harris, P.J.F. Structure of non-graphitising carbons. *International Materials Reviews* **1997**, *42*, 206–218, doi:10.1179/imr.1997.42.5.206.

109. Franklin, R.E. Crystallite growth in graphitizing and non-graphitizing carbons. *Proceedings of the Royal Society A* **1951**, *209*, 196–218, doi:10.1098/rspa.1951.0197.

110. Saleem, J.; Shahid, U.B.; Hijab, M.; Mackey, H.; McKay, G. Production and applications of activated carbons as adsorbents from olive stones. *Biomass Conversion and Biorefinery* **2019**, *9*, 775–802, doi:10.1007/s13399-019-00473-7.

111. Marsh, H.; Rodríguez-Reinoso, F. *Activated carbon*, 1st ed.; Elsevier: Amsterdam, London, **2006**, ISBN 9780080444635.

112. Otowa, T.; Tanibata, R.; Itoh, M. Production and adsorption characteristics of MAXSORB: High-surface-area active carbon. *Gas Separation & Purification* **1993**, *7*, 241–245, doi:10.1016/0950-4214(93)80024-Q.

113. Abd, A.A.; Othman, M.R.; Kim, J. A review on application of activated carbons for carbon dioxide capture: present performance, preparation, and surface modification for further improvement. *Environmental Science and Pollution Research* **2021**, *28*, 43329–43364, doi:10.1007/s11356-021-15121-9.

114. Zhang, F.; Zhang, S.; Chen, L.; Liu, Z.; Qin, J. Utilization of bark waste of Acacia mangium: The preparation of activated carbon and adsorption of phenolic wastewater. *Industrial Crops and Products* **2021**, *160*, 113157, doi:10.1016/j.indcrop.2020.113157.

115. Sadeek, S.A.; Mohammed, E.A.; Shaban, M.; Abou Kana, M.; Negm, N.A. Synthesis, characterization and catalytic performances of activated carbon-doped transition metals during biofuel production from waste cooking oils. *Journal of Molecular Liquids* **2020**, *306*, 112749, doi:10.1016/j.molliq.2020.112749.

116. Winata, A.S.; Devianto, H.; Susanti, R.F. Synthesis of activated carbon from salacca peel with hydrothermal carbonization for supercapacitor application. *Materials Today: Proceedings* **2021**, *44*, 3268–3272, doi:10.1016/j.matpr.2020.11.515.

117. Tong, P.; Zhao, R.; Zhang, R.; Yi, F.; Shi, G.; Li, A.; Chen, H. Characterization of lead (Ⅱ)-containing activated carbon and its excellent performance of extending lead-acid battery cycle life for high-rate partial-state-of-charge operation. *Journal of Power Sources* **2015**, *286*, 91–102, doi:10.1016/j.jpowsour.2015.03.150.

118. Kirchev, A.; DuPasquier, A.; Atanassova, P. Oxidized carbon blacks and applications for lead acid batteries. *U.S. Patent 2016/0322634 A1*, November **2016**.

119. Figueiredo, J.L. Functionalization of porous carbons for catalytic applications. *Journal of Materials Chemistry A* **2013**, *1*, 9351–9364, doi:10.1039/c3ta10876g.

120. Laszlo, K.; Szucs, A. Surface characterization of polyethyleneterephthalate (PET) based activated carbon and the effect of pH on its adsorption capacity from

aqueous phenol and 2, 3, 4-trichlorophenol solutions. *Carbon* **2001**, *39*, 1945–1953, doi:10.1016/S0008-6223(01)00005-7.

121. Otake, Y.; Jenkis, R.G. Characterization of oxygen-containing surface complexes created on a microporous carbon by air and nitric acid treatment. *Carbon* **1993**, 31, 109–121, doi:10.1016/0008-6223(93)90163-5

122. Barton, S.S.; Evans, M.; Halliop, E.; Macdonald, J. Acidic and basic sites on the surface of porous carbon. *Carbon* **1997**, *35,* 1361–1366, doi:10.1016/S0008-6223(97)00080-8.

123. Boehm, H.P. Catalytic Properties of Nitrogen-Containing Carbons. In *Carbon materials for catalysis*; Serp, P., Figueiredo, J.L., Eds.; John Wiley & Sons: Hoboken, NJ, **2009**, ISBN 9780470403709.

124. Montes-Morán, M.A.; Suárez, D.; Menéndez, J.A.; Fuente, E. On the nature of basic sites on carbon surfaces: an overview. *Carbon* **2004**, *42*, 1219–1225, doi:10.1016/j.carbon.2004.01.023.

125. Stein, A.; Wang, Z.; Fierke, M.A. Functionalization of porous carbon materials with designed pore architecture. *Advanced Materials* **2009**, *21*, 265–293, doi:10.1002/adma.200801492.

126. Vinke, P.; van der Euk, M.; Verbree, M.; Voskamp, A.F.; van Bekkum, H. Modification of the surfaces of a gas-activated carbon and a chemically activated carbon with nitric acid, hypochlorite, and ammonia. *Carbon* **1994**, *32*, 675–686, doi:10.1016/0008-6223(94)90089-2

127. Pradhan, B.K.; Sandle, N.K. Effect of different oxidizing agent treatments on the surface properties of activated carbons. *Carbon* **1999**, *37*, 1323–1332, doi:10.1016/S0008-6223(98)00328-5.

128. Chen, X.; Farber, M.; Gao, Y.; Kulaots, I.; Suuberg, E.M.; Hurt, R.H. Mechanisms of surfactant adsorption on non-polar, air-oxidized and ozone-treated carbon surfaces. *Carbon* **2003**, *41*, 1489–1500, doi:10.1016/S0008-6223(03)00053-8.

129. Gomes, H.T.; Miranda, S.M.; Sampaio, M.J.; Silva, A.; Faria, J.L. Activated carbons treated with sulphuric acid: Catalysts for catalytic wet peroxide oxidation. *Catalysis Today* **2010**, *151*, 153–158, doi:10.1016/j.cattod.2010.01.017.

130. Mangun, C.L.; Benak, K.R.; Daley, M.A.; Economy, J. Oxidation of activated carbon fibers: Effect on pore size, surface chemistry, and adsorption properties. *Chemistry of Materials* **1999**, *11*, 3476–3483, doi:10.1021/cm990123m.

131. Cheng, P.Z.; Teng, H. Electrochemical responses from surface oxides present on HNO3-treated carbons. *Carbon* **2003**, *41*, 2057–2063, doi:10.1016/S0008-6223(03)00212-4.

132. Figueiredo, J.L.; Pereira M.F.R.; Freitas M.M.A.; Órfão J.J.M. Modification of the surface chemistry of activated carbons. *Carbon* **1999**, *37*, 1379–1389, doi:10.1016/S0008-6223(98)00333-9.

133. Jia, Y.F.; Xiao, B.; Thomas, K.M. Adsorption of metal ions on nitrogen surface functional groups in activated carbons. *Langmuir* **2002**, *18*, 470–478, doi:10.1021/la011161z.

134. Leon y Leon, C.A.; Solar, J.M.; Calemma, V.; Radovic, L.R. Evidence for the protonation of basal plane sites on carbon. *Carbon* **1992**, *30*, 797–811, doi:10.1016/0008-6223(92)90164-R.

135. Pietrzak, R. XPS study and physico-chemical properties of nitrogen-enriched microporous activated carbon from high volatile bituminous coal. *Fuel* **2009**, *88*, 1871–1877, doi:10.1016/j.fuel.2009.04.017.

136. Bandosz, T.J. Surface Chemistry of Carbon Materials. In *Carbon materials for catalysis*; Serp, P., Figueiredo, J.L., Eds.; John Wiley & Sons: Hoboken, NJ, **2009**, ISBN 9780470403709.

137. Jansen, R.; van Bekkum, H. Amination and ammoxidation of activated carbons. *Carbon* **1994**, *32*, 1507–1516, doi:10.1016/0008-6223(94)90146-5.

138. Shafeeyan, M.S.; Daud, W.; Houshmand, A.; Arami-Niya, A. Ammonia modification of activated carbon to enhance carbon dioxide adsorption: Effect of pre-oxidation. *Applied Surface Science* **2011**, *257*, 3936–3942, doi:10.1016/j.apsusc.2010.11.127.

139. Świetlik, U.; Grzyb, B.; Torchała, K.; Gryglewicz, G.; Machnikowski, J. High temperature ammonia treatment of pitch particulates and fibers for nitrogen enriched microporous carbons. *Fuel Processing Technology* **2014**, *119*, 211–217, doi:10.1016/j.fuproc.2013.11.009.

140. Bashkova, S.; Bandosz, T.J. The effects of urea modification and heat treatment on the process of NO2 removal by wood-based activated carbon. *Journal of Colloid and Interface Science* **2009**, *333*, 97–103, doi:10.1016/j.jcis.2009.01.052.

141. Le, H.N.T.; Jeong, H.K. Synthesis and characterization of nitrogen-doped activated carbon by using melamine. *New Physics: Sae Mulli* **2015**, *65*, 86–89, doi:10.3938/NPSM.65.86.

142. Pevida, C.; Plaza, M.G.; Arias, B.; Fermoso, J.; Rubiera, F.; Pis, J.J. Surface modification of activated carbons for CO2 capture. *Applied Surface Science* **2008**, *254*, 7165–7172, doi:10.1016/j.apsusc.2008.05.239.

143. Dastgheib, S.A.; Karanfil, T.; Cheng, W. Tailoring activated carbons for enhanced removal of natural organic matter from natural waters. *Carbon* **2004**, *42*, 547–557, doi:10.1016/j.carbon.2003.12.062.

144. Guerro-Ruiz, A.; Rodriguez-Ramos, I.; Rodriguez-Reinoso, F. The role of nitrogen and oxygen surface groups in the behavior of carbon supported iron and ruthenium catalysts. *Carbon* **1988**, *26*, 417–423, doi:10.1016/0008-6223(88)90140-6.

145. Papirer, E.; Li, S.; Donnet, J.B. Contribution to the study of basic surface groups on carbons. *Carbon* **1987**, *25*, 243–247, doi:10.1016/0008-6223(87)90122-9.

146. Dandekar, A.; Baker, R.; Vannice, M.A. Characterization of activated carbon, graphitized carbon fibers and synthetic diamond powder using TPD and DRIFTS. *Carbon* **1998**, *36*, 1821–1831, doi:10.1016/S0008-6223(98)00154-7.

147. Menéndez, J.A.; Phillips, J.; Xia, B.; Radovic, L.R. On the modification and characterization of chemical surface properties of activated carbon: In the search of carbons with stable basic properties. *Langmuir* **1996**, *12*, 4404–4410, doi:10.1021/la9602022.

148. Menéndez, J.A.; Xia, B.; Phillips, J.; Radovic, L.R. On the modification and characterization of chemical surface properties of activated carbon: Microcalorimetric, electrochemical and thermal desorption probes. *Langmuir* **1997**, *13*, 3414–3421, doi:10.1021/la970200x.

149. Pereira, M.; Soares, S.F.; Órfão, J.; Figueiredo, J.L. Adsorption of dyes on activated carbons: influence of surface chemical groups. *Carbon* **2003**, *41*, 811–821, doi:10.1016/S0008-6223(02)00406-2.

150. Menéndez, J.A.; Radovic, L.R. Low-temperature generation of basic carbon surfaces by hydrogen spillover. *Journal of the Physical Chemistry* **1996**, *100*, 17243–17248, doi:10.1021/jp961243+.

151. Garten, V.A.; de Weiss; Willis, J.B. A new interpretation of the acidic and basic structures in carbons. II. The chromene-carbonium ion couple in carbon. *Australian Journal of Chemistry* **1957**, *10*, 309–328, doi:10.1071/CH9570309.

152. Contescu, A.; Vass, M.; Contescu, C.; Putyera, K.; Schwarz, J.A. Acid buffering capacity of basic carbons revealed by their continuous pK distribution. *Carbon* **1998**, *36*, 247–258, doi:10.1016/S0008-6223(97)00168-1.

153. Boehm, H.P. Surface oxides on carbon and their analysis: a critical assessment. *Carbon* **2002**, *40*, 145–149, doi:10.1016/S0008-6223(01)00165-8.

154. Bozkaya, B.; Bauknecht, S.; Settelein, J.; Kowal, J.; Karden, E.; Giffin, G.A. Comparison of dynamic charge acceptance tests on lead-acid cells for carbon additive screening. Energy Technology, **2022**, *10*, 2101051, doi: 10.1002/ente.202101051.

155. Scherdel, C.; Scherb, T.; Reichenauer, G. Spherical porous carbon particles derived from suspensions and sediments of resorcinol-formaldehyde particles. *Carbon* **2009**, *47*, 2244-2252, doi:10.1016/j.carbon.2009.04.015.

156. Brunauer, S.; Emmett, P.H.; Teller, E. Adsorption of Gases in Multimolecular Layers. *Journal of the American Chemical Society* **1938**, *60*, 309–319, doi:10.1021/ja01269a023.

157. Pekala, R.W.; Alviso, C.T. Carbon Aerogels and Xerogels. *MRS Online Proceedings Library* **1992**, *270*, 3–14, doi:10.1557/PROC-270-3.

158. Battery Association of Japan. *Lead-acid batteries for vehicles with stop and start system SBA S 0101:2014*, **2014**.

159. Schaeck, S.; Stoermer, A.O.; Kaiser, F.; Koehler, L.; Albers, J.; Kabza, H. Lead-acid batteries in micro-hybrid applications. Part I. Selected key parameters. *Journal of Power Sources* **2011**, *196*, 1541–1554, doi:10.1016/j.jpowsour.2010.08.077.

160. Thele, M.; Schiffer, J.; Karden, E.; Surewaard, E.; Sauer, D.U. Modeling of the charge acceptance of lead–acid batteries. *Journal of Power Sources* **2007**, *168*, 31–39, doi:10.1016/j.jpowsour.2006.11.088.

161. Bauknecht, S.; Bozkaya, B.; Settelein, J.; Karden, E.; Kowal, J. The Influence of Cell Size on Dynamic Charge Acceptance Tests in Laboratory Lead-Acid Cells. *Energy Technology*, **2022**, *10*, 2101053, doi: 10.1002/ente.202101053.

162. Kirchev, A.; Mattera, F.; Lemaire, E.; Dong, K. Studies of the pulse charge of lead-acid batteries for photovoltaic applications: Part IV. Pulse charge of the negative plate. *Journal of Power Sources* **2009**, *191*, 82–90, doi:10.1016/j.jpowsour.2008.10.098.

163. Kwiecien, M.; Badeda, J.; Huck, M.; Komut, K.; Duman, D.; Sauer, D.U. Determination of SoH of Lead-Acid Batteries by Electrochemical Impedance Spectroscopy. *Applied Sciences* **2018**, *8*, 873, doi:10.3390/app8060873.

164. Hampson, N.A.; Kelly, N.; Peters, K. Fundamentals of lead-acid cells. XVII. The a.c. impedance of lead dioxide formed in sulphuric acid on some lead alloys. *Journal of Applied Electrochemistry*, **1981**, *11*, 751–763, doi:10.1007/BF00615180.

165. Macdonald, J.R. *Impedance Spectroscopy: Theory, Experiment, and Applications*: *Second edition;* Wiley-Interscience a John Wiley & Sons Inc. publication: Hoboken, New Jersey, **2005**, ISBN 0-471-64749-7.

166. Bard, A.J.; Faulkner, L.R. *Electrochemical methods*: *Fundamentals and applications*, 2. ed.; Wiley: Hoboken, NJ, **2001**, ISBN 9780471043720.

167. Thele, M. *A contribution to the modelling of the charge acceptance of lead-acid batteries - using frequency and time domain based concepts*. PhD thesis; Shaker: Aachen, **2008**, ISBN 9783832276591.

168. Kowal, J. *Spatially-resolved impedance on nonlinear inhomogenerous devices: Using the example of lead-acid batteries*. PhD thesis; Shaker: Aachen, **2010**, ISBN 9783832294830.

169. Bozkaya, B.; Settelein, J.; Komma, M.; Gryglewicz, G.; Sextl, G.; Giffin, G.A. Influence of basic carbon additives on the electrochemical performance of lead-carbon batteries. *Journal of Energy Storage* **2021**, *44*, 103400, doi:10.1016/j.est.2021.103400.

170. Jaramillo, J.; Álvarez, P.M.; Gómez-Serrano, V. Oxidation of activated carbon by dry and wet methods: Surface chemistry and textural properties. *Fuel Processing Technology* **2010**, *91*, 1768–1775, doi:10.1016/j.fuproc.2010.07.018.

171. Weidenthaler, C.; Lu, A.H.; Schmidt, W.; Schüth, F. X-ray photoelectron spectroscopic studies of PAN-based ordered mesoporous carbons (OMC). *Microporous and Mesoporous Materials* **2006**, *88*, 238–243, doi:10.1016/j.micromeso.2005.09.015.

172. Adelodun, A.A.; Jo, Y.M. Integrated basic treatment of activated carbon for enhanced CO2 selectivity. *Applied Surface Science* **2013**, *286*, 306–313, doi:10.1016/j.apsusc.2013.09.076.

173. Zielke, U.; Hüttinger, K.J.; Hoffman, W.P. Surface-oxidized carbon fibers: I. Surface structure and chemistry. *Carbon* **1996**, *34*, 983–988, doi:10.1016/0008-6223(96)00032-2.

174. Lorenc-Grabowska, E.; Gryglewicz, G.; Diez, M.A. Kinetics and equilibrium study of phenol adsorption on nitrogen-enriched activated carbons. *Fuel* **2013**, *114*, 235–243, doi:10.1016/j.fuel.2012.11.056.

175. Biniak, S.; Pakuła, M.; Szymański, G.S.; Świątkowski, A. Effect of activated carbon surface oxygen- and/or nitrogen-containing groups on adsorption of copper(II) ions from aqueous solution. *Langmuir* **1999**, *15*, 6117–6122, doi:10.1021/la9815704.

176. Stoeckli, F.; López-Ramón, M.; Hugi-Cleary, D.; Guillot, A. Micropore sizes in activated carbons determined from the Dubinin–Radushkevich equation. *Carbon* **2001**, *39*, 1115–1116, doi:10.1016/S0008-6223(01)00054-9.

177. Barroso-Bogeat, A.; Alexandre-Franco, M.; Fernández-González, C.; Macías-García, A.; Gómez-Serrano, V. Electrical conductivity of activated carbon-metal oxide nanocomposites under compression: a comparison study. *Physical Chemistry Chemical Physics* **2014**, *16*, 25161–25175, doi:10.1039/c4cp03952a.

178. Kim, J.H.; Hwang, S.Y.; Park, J.E.; Lee, G.B.; Kim, H.; Kim, S.; Hong, B.U. Impact of the oxygen functional group of nitric acid-treated activated carbon on KOH activation reaction. *Carbon Letters* **2019**, *29*, 281–287, doi:10.1007/s42823-019-00024-0.

179. Stavropoulos, G.G.; Samaras, P.; Sakellaropoulos, G.P. Effect of activated carbons modification on porosity, surface structure and phenol adsorption. *Journal of Hazardous Materials* **2008**, *151*, 414–421, doi:10.1016/j.jhazmat.2007.06.005.

180. Strelko, V.; Malik, D.; Streat, M. Characterisation of the surface of oxidised carbon adsorbents. *Carbon* **2002**, *40*, 95–104, doi:10.1016/S0008-6223(01)00082-3.

181. Jansen, R.; van Bekkum, H. XPS of nitrogen-containing functional groups on activated carbon. *Carbon* **1995**, *33*, 1641–1653, doi:10.1016/0008-6223(95)00030-h.

182. Bota, K.B.; Abotsi, G. Ammonia: a reactive medium for catalysed coal gasification. *Fuel* **1994**, *73*, 1354–1357, doi:10.1016/0016-2361(94)90313-1.

183. Stöhr, B.; Boehm, H.P. Enhancement of the catalytic activity of activated carbons in oxidation reactions by thermal treatment with ammonia or hydrogen cyanide and observation of a superoxide species as a possible intermediate. *Carbon* **1991**, *29*, 707–720, doi:10.1016/0008-6223(91)90006-5.

184. Figueiredo, J.L.; Pereira, M. The role of surface chemistry in catalysis with carbons. *Catalysis Today* **2010**, *150*, 2–7, doi:10.1016/j.cattod.2009.04.010.

185. Biniak, S.; Szymański, G.; Siedlewski, J.; Swiatkowski, A. The characterization of activated carbons with oxygen and nitrogen surface groups. *Carbon* **1997**, *35*, 1799–1810, doi:10.1016/S0008-6223(97)00096-1.

186. Vautard, F.; Grappe, H.; Ozcan, S. Stability of carbon fiber surface functionality at elevated temperatures and its influence on interfacial adhesion. *Applied Surface Science* **2013**, *268*, 61–72, doi:10.1016/j.apsusc.2012.11.158.

187. Samant, P.V.; Gonçalves, F.; Freitas, M.; Pereira, M.; Figueiredo, J.L. Surface activation of a polymer based carbon. *Carbon* **2004**, *42*, 1321–1325, doi:10.1016/j.carbon.2004.01.034.

188. Chen, W.; Cannon, F.S.; Rangel-Mendez, J.R. Ammonia-tailoring of GAC to enhance perchlorate removal. I: Characterization of NH3 thermally tailored GACs. *Carbon* **2005**, *43*, 573–580, doi:10.1016/j.carbon.2004.10.024.

189. Kiuchi, H.; Shibuya, R.; Kondo, T.; Nakamura, J.; Niwa, H.; Miyawaki, J.; Kawai, M.; Oshima, M.; Harada, Y. Lewis Basicity of Nitrogen-Doped Graphite Observed by CO2 Chemisorption. *Nanoscale Research Letters* **2016**, *11*, 127, doi:10.1186/s11671-016-1344-6.

190. Darmstadt, H.; Roy, C. Surface spectroscopic study of basic sites on carbon blacks. *Carbon* **2003**, *41*, 2662–2665, doi:10.1016/S0008-6223(03)00325-7.

191. Boehm, H.P. Some aspects of the surface chemistry of carbon blacks and other carbons. *Carbon* **1994**, *32*, 759–769, doi:10.1016/0008-6223(94)90031-0.

192. Zherebtsov, D.A.; Pankratov, D.A.; Dvoryak, S.V.; Zhivulin, D.E.; Eremyashev, V.E.; Yantsen, R.F.; Zhivulin, V.E.; Smolyakova, K.R.; Lebedeva, S.M.; Avdin, V.V.; et al. Key role of nitrogen in conductivity of carbon-nitrogen materials. *Diamond and Related Materials* **2021**, *111*, 108183, doi:10.1016/j.diamond.2020.108183.

193. Mousavi, H.; Moradian, R. Nitrogen and boron doping effects on the electrical conductivity of graphene and nanotube. *Solid State Sciences* **2011**, *13*, 1459–1464, doi:10.1016/j.solidstatesciences.2011.03.008.

194. Li, Y.; Ai, C.; Deng, S.; Wang, Y.; Tong, X.; Wang, X.; Xia, X.; Tu, J. Nitrogen doped vertical graphene as metal-free electrocatalyst for hydrogen evolution reaction. *Materials Research Bulletin* **2021**, *134*, 111094, doi:10.1016/j.materresbull.2020.111094.

195. Davodi, F.; Tavakkoli, M.; Lahtinen, J.; Kallio, T. Straightforward synthesis of nitrogen-doped carbon nanotubes as highly active bifunctional electrocatalysts for full water splitting. *Journal of Catalysis* **2017**, *353*, 19–27, doi:10.1016/j.jcat.2017.07.001.

196. Jiang, Z.; Wang, T.; Song, L.; Guo, H.; Xia, W.; Gong, H.; Gao, B.; Feng, L.; Liu, X.; He, J. High over-potential nitrogen-doped activated carbon towards hydrogen evolution inhibition in sulfuric acid solution. *Journal of Material Science: Materials in Electronics* **2018**, *29*, 14170–14179, doi:10.1007/s10854-018-9550-x.

197. Lee, Y.H.; Chang, K.H.; Hu, C.C. Differentiate the pseudocapacitance and double-layer capacitance contributions for nitrogen-doped reduced graphene oxide in acidic and alkaline electrolytes. *Journal of Power Sources* **2013**, *227*, 300–308, doi:10.1016/j.jpowsour.2012.11.026.

198. Seredych, M.; Hulicova-Jurcakova, D.; Lu, G.Q.; Bandosz, T.J. Surface functional groups of carbons and the effects of their chemical character, density and accessibility to ions on electrochemical performance. *Carbon* **2008**, *46*, 1475–1488, doi:10.1016/j.carbon.2008.06.027.

199. Hsieh, C.T.; Teng, H. Influence of oxygen treatment on electric double-layer capacitance of activated carbon fabrics. *Carbon* **2002**, *40*, 667–674, doi:10.1016/S0008-6223(01)00182-8.

200. Wang, Z.; Wang, Y.; Hao, X.; Liu, J.; Chen, Y.; Li, P.; Dong, M. Modulation of oxygen functional groups and their influence on the supercapacitor performance of reduced graphene oxide. *New Journal of Chemistry* **2020**, *44*, 19022–19027, doi:10.1039/D0NJ04072J.

Appendix

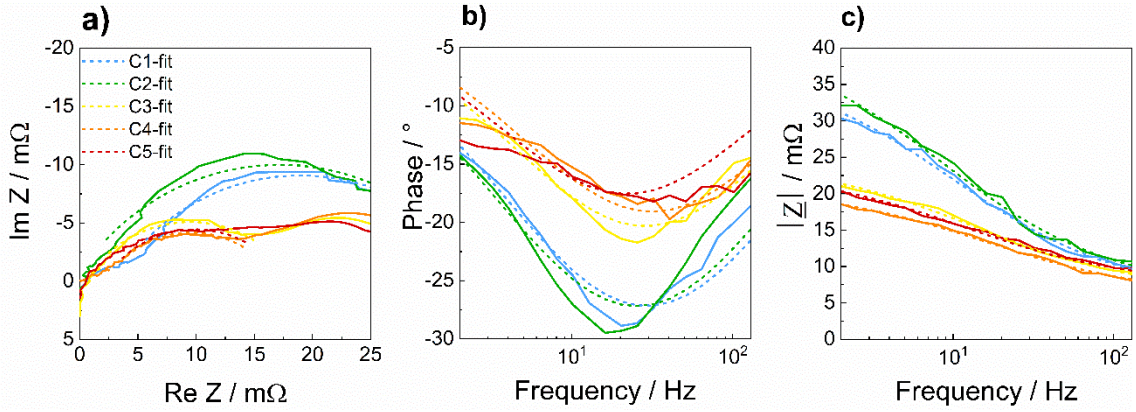

Figure A.1: The fitting of negative electrode spectrum in a frequency range between 2 Hz and 128.5 Hz for a) Nyquist plot and b, c) Bode plot.

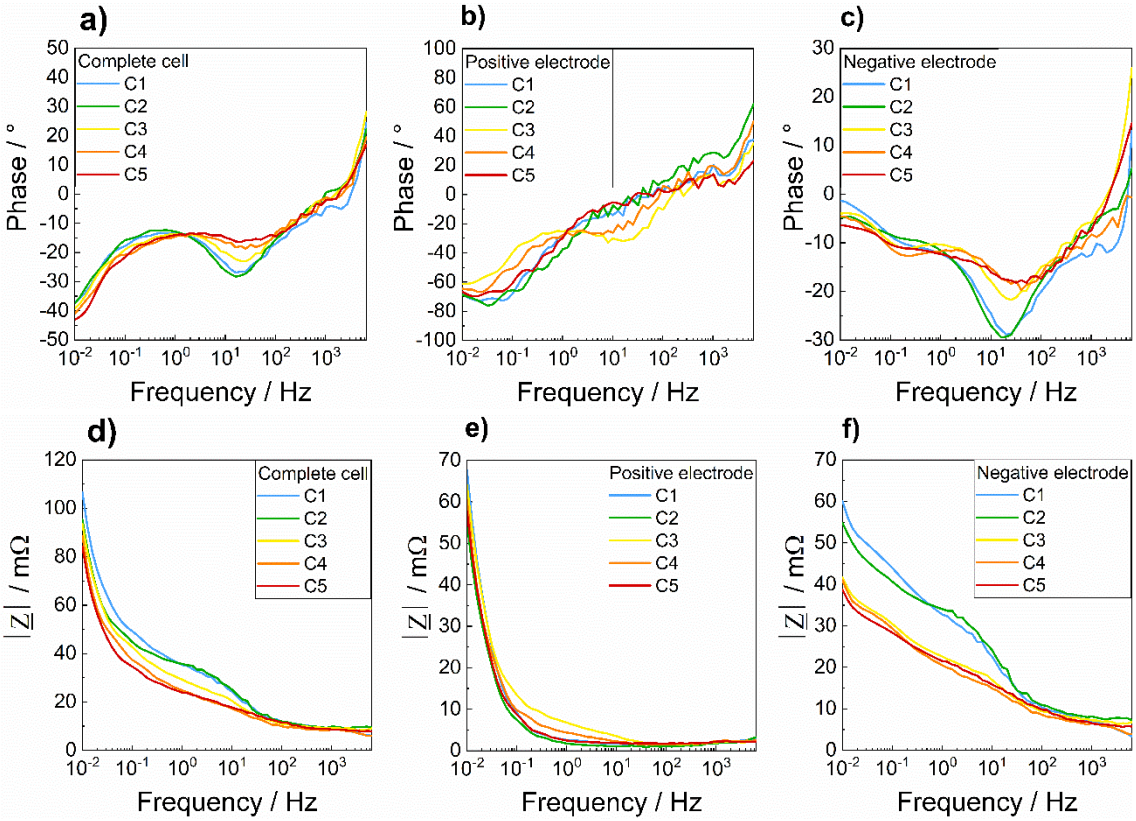

Figure A.2: Bode plot obtained from the electrochemical impendance spectroscopy executed after the qDCA part of the DCA (EN) test for a,d) complete cell; b,e) positive electrode and c,f) negative electrode. The EIS measurements were performed with a superimposed charge current of $0.5 \cdot I_{20}$.

List of Abbreviations

Acronyms

1BS	Monobasic lead sulfate
3BS	Tribasic lead sulfate
ac	Alternating current
AC	Activated carbon
AC-ai	Acidic activated carbon
AC-bi	Basic activated carbon
Ah	Ampere-hour
BET	Brunauer, Emmet and Teller
Ci	Amorphous carbon
CA	Charge acceptance
CB	Carbon black
CC	Constant current
CPE	Constant phase element
CV	Cyclic voltammetry
dc	Direct current
DCA	Dynamic charge acceptance
DCRss	Real-world stop/start drive cycle
DL	Double-layer
DR	Dubinin-Radushkevich
EC	Equivalent circuit
ECM	Equivalent circuit model
EIS	Electrochemical impedance spectroscopy
EN	European norm
GEIS	Galvanostatic electrochemical impedance spectroscopy
HER	Hydrogen evolution reaction
HEV	Hybrid electric vehicle
HRPSoC	High-rate partial state of charge
KOL	Key-off load
LAB	Lead-acid battery
NAM	Negative active material
NHE	Normal hydrogen electrode
OCV	Open circuit voltage
OEM	Original equipment manufacturer
OER	Oxygen evolution reaction
ORR	Oxygen recombination reaction
PSoC	Partial state of charge
PTFE	Teflon
qDCA	Quick DCA
RC	Reserve capacity
RHE	Reversible hydrogen electrode
SBA	Test standard for lead batteries developed by Battery Association of Japan
SEM	Scanning electron microscopy
SLI	Starting, lighting and ignition
SoC	State of charge
XPS	X-ray photoelectron spectroscopy
XRD	X-ray diffraction

Physical Parameters

a_i	Activity of a substance
A	Area
C	Capacity
C_n	Nominal capacity
$C_{compact}$	Compact capacitance
$C_{diffuse}$	Diffuse layer capacitance
C_D	Total double-layer capacitance
C_{DL}	Differential double-layer capacitance
C_{ox}	Bulk concentration of oxidized species
C_{red}	Bulk concentration of reduced species
C^s_{ox}	Surface concentration of oxidized species
C^s_{red}	Surface concentration of reduced species
D	Diffusion coefficient
d_{part}	Average particle diameter
E	Equilibrium potential
E_0	Open-circuit potential
E^0	Formal potential
$E_{M\text{-}H}$	Energy of hydride formation
E_i	Initial potential
E_v	Vertex potential
e^-	Electron
f	Frequency
h	Height
H*	Adsorbed hydrogen
H^+	Positively-charged hydrogen ion
i_0	Exchange current
i_c	Capacitance charging current
i	Current
I	Current amplitude
I_c	Charge acceptance after charge history
I_d	Charge acceptance after discharge history
I_{DCA}	Dynamic charge acceptance
I_r	Charge acceptance during simulated stop/start drive cycle
I_{recu}	Recuperation current
-Im (Z)	Imaginary part of the impedance
j	Imaginary number
j_{00}	Exchange current density
k^0	Electron-transfer rate constant
L	Inductance
m_t	Rate of mass transport
n	Number of exchanged electrons
M	Metal
P_{H_2}	Partial pressure of hydrogen
P_{O_2}	Partial pressure of oxygen
Q	Electrical charge
R	Electrical resistance
R_{CT}	Charge-transfer resistance
R_d	Diffusion resistance
R_i	Internal resistance

Re (Z)	Real part of the impedance
S_{BET}	Specific BET surface area
S_{ext}	Specific external surface area
$S_{spherical}$	Spherical surface
S_{red}	Reduzierte Spezies
T	Temperature
t	Time
u	Voltage
U	Voltage amplitude
V_C	Volume of the non-porous carbon skeleton
V_{DR}	Micropore volume according to Dubinin-Radushkevich
V_{meso}	Mesopore volume
V_{mic}	Specific micropore volume
$V_{spherical}$	Spherical volume
V_T	Total pore volume
Z	Complex impedance amplitude
Z (f)	Complex impedance as a function of frequency
Z_W	Warburg impedance

Greek Letters

α	Transfer coefficient
η	Overpotential
Λ	Matsa number
φ	Chemical potential
ϕ	Phase
ϕ_i	Phase for current
ϕ_u	Phase for voltage
τ	Time constant
ξ	CPE parameter
ν	Diffusion coefficient
ω	Angular frequency
ρ	Density

Constants

F	Faraday constant
π	Pi
R	Universal gas constant

Acknowledgement

This dissertation was conducted at Fraunhofer Institute for Silicate Research ISC in Würzburg and its main funding was received from the Bavarian State Ministry of Economic Affairs and Media, Energy and Technology (Grant No. 43-6629/86). The results of chapter 3 were generated during an industrial project funded by Consortium for Battery Innovation (CBI), former Advanced Lead-Acid Battery Consortium (ALABC). Several people involved in this dissertation and their valuable contributions should be mentioned here.

Firstly, I take this opportunity to express my gratitude to my Ph.D. supervisor Prof. Dr. Gerhard Sextl for his supervision and support during this dissertation as well as for giving me the opportunity to conduct this work at Fraunhofer ISC. I also express my regards to Prof. Dr. Grażyna Gryglewicz and to Prof. Dr. Lutz Nuhn for being the second and third promoter of my thesis, respectively.

Secondly, I want to thank Dr. Jochen Settelein, for introducing me to the lead-acid battery field and for his supervision during my dissertation. Thank you very much for the constructive and motivating discussions as well as for correcting the first version of my thesis. My grateful thanks are extended to Prof. Dr. Grażyna Gryglewicz for her endless help, discussions and encouragement in every part of the research. I am very grateful for our collaboration as well as for the preliminary study of oxidized carbons and the characterization of all activated carbons by elemental analysis and nitrogen sorption, conducted at Wroclaw University of Science and Technology.

Thirdly, I am especially thankful to OE 322 (former lead-acid battery group) for their valuable contribution and friendly support, which includes Jochen Settelein, Paul Wulfert-Holzmann, Gabi Ulm, Elena Fleder as well as my students Lukas Gerstner and Miriam Komma. I am also very grateful to Martina Kapuschinski, Oliver Schüßler and Vilija Anfimovaite for their endless help in the laboratory, whenever I needed them.

I also would like to thank Dr. Henning Lorrmann for giving me this chance to be a part of the group of Fraunhofer R&D Center Electromobility Bavaria FZEB. I am also thankful to all colleagues in FZEB for their cooperation and the pleasant working atmosphere. Many thanks to Lukas Gold for his support and his help during electrochemical impedance spectroscopy measurements. Also, special thanks to Matthias Rumpel and Marian Cabanero for scientific discussions and support during my time at Fraunhofer ISC. My grateful thanks are also extended to Dr. Guinevere Giffin for her guidance and support in publishing papers.

Besides my colleagues in FZEB and OE 322, I had the chance to get support from the other working groups at Fraunhofer ISC. I would like to thank Angelika Schmitt and Dr. Alexander Reinholdt for performing the XPS measurements and for helping me with the evaluation of the XPS data. I am also thankful to Ralf Herborn, Arne Rüdinger and Jens Baber for their help in the gas-phase modifications of carbons such as ammonia and hydrogen treatments. I also want to thank Werner Stracke for teaching me how to conduct SEM measurements.

My dissertation was all about cooperations. During this time, I had the chance to work with great people such as Sophia Bauknecht, Prof. Dr. Julia Kowal and Dr. Eckhard Karden. Thank you very much Sophia for the evaluation of my EIS data. Many thanks to Julia and Eckhard for their valuable feedback and scientific discussions during our joint CBI (former ALABC) project. I especially thank Eckhard Karden for encouraging me to give several presentations at international conferences and workshops.

Lastly, I want to say thanks to the most important people in my life, my family, my friends and my boyfriend. So many unexpected things happened, especially during the corona pandemic, when I was far away from home but you were always there for me. During this time, my friends in Eskisehir and Würzburg have always supported me. I especially thank my boyfriend and his parents for their extensive help, patience and understanding, when I was writing my thesis. Also my parents and my brother, without your unconditional support, I could have never come to this point. Therefore, I dedicate this work to you.